Model-Based Iterative Image Reconstruction for Echo-Planar Imaging

September 17, 2018

Delft University of Technology

Author   Lars Rehbein [1]
Student Number 4623037

Committee   Dr. Rob F. Remis [2]
Prof. Dr. Peter Börnert [3]
Prof. Dr. Andrew G. Webb [4]
Dr. Vasiliki Giagka [5]

PHILIPS

Submitted in partial fulfilment of the requirements for the degree of

MASTER OF SCIENCE

in Electrical Engineering - Track Signals & Systems.

The project was conducted in collaboration of the Circuits and Systems group of the faculty Electrical Engineering, Mathematics and Computer Science and Philips Research Hamburg.

TU Delft
Delft
University of
Technology

Challenge the future

[1] Lars Rehbein   TU Delft, Student Number 4623037
Albererweg 16a, 83236 Übersee / GER
larsrehbein@posteo.net

[2] Rob Remis   TU Delft, Faculty EEMCS
Mekelweg 4, 2628CD Delft / NL
r.f.remis@tudelft.nl

[3] Peter Börnert   Philips GmH Innovative Technologies, Research Laboratories
Röntgenstraße 24-26, 22335 Hamburg / GER
peter.boernert@philips.com

[4] Andrew Webb   Leiden University Medical Center
Albinusdreef 2, 2333ZA Leiden / NL
a.webb@lumc.nl

[5] Vasiliki Giagka   TU Delft, Faculty EEMCS
Mekelweg 4, 2628CD Delft / NL
v.giagka@tudelft.nl

Confidentiality Clause

This thesis with the title *Model-Based Iterative Image Reconstruction for Echo-Planar Imaging* is based on internal and confidential data of Philips Research. This work may only be available to the reviewers and authorised members of the board of examiners. An inspection or publication and duplication of this thesis - even in part - requires the expressed admission of the author or the management of Philips Research. This confidentiality clause is temporally restricted and expires three years after the submission date of the thesis.

Preface

When starting my master programme *Electrical Engineering - Signal & Systems* at TU Delft, I started quickly to understand the depth and sophistication of signal processing theories. Having had some limited contact with medical imaging during my bachelor studies, I decided to gain some more knowledge by taking a course about different medical imaging modalities.

During this course and the *Medical Physics* Symposium 2017 at TU Delft, I realised that understanding MRI follows the line of thinking I enjoyed the most: Starting from the underlying, concise theory and description of *Nuclear magnetic resonance*, MRI has a vast range of topics from signal generation, signal detection and signal processing that allows deepening ones knowledge in a perceived infinite depth.

Having heard Andrew Webb's talk at the *Medical Physics* Symposium and met him shortly after at the mentioned medical imaging course, I was lucky that Andrew provided me with the contact to Peter Börnert, and I want to thank him for that. Peter's endeavour to guide me with his extensive knowledge throughout my work at *Philips Research* should be greatly appreciated here. Rob Remis' reachability and helpfulness in all matters helped conducting my thesis at *Philips Research* Hamburg, while still being a student at TU Delft, an astonishingly easy-going way of working.

I want to thank my family and especially my parents, without whose longstanding support this Master thesis couldn't represent the end of my master studies.

The thesis at hand is structured into seven sequential chapters: The *Introduction* chapter gives a brief summary of the state of art image reconstruction for Echo-planar imaging. Furthermore, the thesis objective are presented here. Chapter two and three present the theoretical knowledge needed to understand the implemented model-based reconstruction algorithm of this work. The *Methodology* chapter presents all expects of modelling and iterative reconstruction in detail, which were used to tackle the problem of *Nyquist ghosting* and field inhomogeneities leading to a concise and joint reconstruction of EPI images. The *Results* of this reconstruction for phantom as well as in vivo measurements can be found in chapter five. The thesis concludes with a *Discussion* of these results, discussing the limits of the executed algorithm and leading to the *Conclusion* in chapter seven.

Delft - September 17, 2018

Abstract

Magnetic Resonance Imaging (MRI) is still a vital and fast evolving medical imaging modality. Especially, due it its excellent soft tissue contrast it is often one of the most preferred diagnostic imaging technologies. Among the different data sampling schemes used is Echo Planar Imaging (EPI), which is one of the fastest and most efficient sampling schemes, representing the workhorse for many time and motion critical applications.

One of the most serious artefacts occurring in Echo-planar imaging (EPI) are Nyquist ghosts, induced by eddy currents and the opposed gradient polarity of adjacent readout lines. On most commercial scanners Nyquist ghosts are tackled by obtaining additional EPI reference data prior to the actual imaging process. Therefore, the imaging protocol is prolonged. Furthermore, for a multislice study the reference data looses validity, due to effects like coil heating associated with a change of eddy currents.

This works demonstrates the replacement of the EPI reference scan with an image-based estimation of phase errors. It is shown that with a separate image reconstruction of data acquired under *odd/even* gradient polarity, a phase error can be estimated. Due to the effectively doubled acceleration factor of this procedure and the *g*-factor induced noise amplification the resulting phase map tends to be noisy. This effect increases non-linearly with the SENSE acceleration factor R. Artefacts occurring in the phase map estimation are directly propagated into the final reconstruction, which leads to image artefacts.

It is argued, that a 1D phase map, calculated by first masking areas of high *g*-factor in the 2D phase map and subsequently calculating an average linear fit of all rows, can alleviate those effects. With the usage of a full 2D phase map, the average Normalised root-mean-square error (nRMSE) of R=1 compared to R=3 increases sixfold. Utilisation of the proposed 1D phase maps halves the error increase to threefold. Therefore, up to R=3 images can be successfully reconstructed using image-based phase maps. It is shown that for phantom measurements the obtained phase map remains valid for adjacent slices.

All calculations are executed using a conjugate gradient (CG) algorithm. It is shown how variable density slope sampling can be integrated into the reconstruction. Furthermore, it is argued that the most efficient integration of field inhomogeneity maps is achieved by interpolating the sensitivity profiles to mimic the effects of field inhomogeneity.

Contents

List of Figures

List of Tables

List of Symbols

a Estimate of unaliased pixel density

A System matrix

$\mathbf{B_0}$ Static magnetic field density vector

$\mathbf{B_1}$ RF field density vector

c Complex sensitivity value

C Sensitivity profile matrix

E_p Potential energy

E Encoding matrix

F Decoding matrix

g Geometry factor

G Applied gradient in one direction

G Applied gradient vector

$\hbar$ Planck constant divided by 2π

H Magnetic field vector

I Intensity correction matrix

J Cost functional

J Current density

$\mathbf{\bar{J}}$ Surface current density

k_{BC} Boltzmann constant

k Spatial frequency vector

l Spin quantum number

L Cholesky decomposition of Ψ

m Sampled data

m Sampled data vector

M_s Binary sampling mask

M Net magnetisation vector

n_d Number of samples

n_c Number of coils

n_p Number of superimposed pixels

N Number of pixels in one direction

O Sampling function

p_{DP} Magnetic dipole moment

p Single coil image

P Coil image matrix for all coils

r Spatial location

R Reduction factor

s Coil sensitivity weighted signal sum

S Spin angular momentum

T_{abs} Absolute temperature

T_1 Time constant T_1

T_2 Time constant T_2

T_2^* Time constant T_2^*

T_E Echo time

v Reconstructed pixel value

v Reconstructed image matrix

W_{KB} *Kaiser-Bessel* window function

Z_f Zero-fill factor

β Regularizer

γ Gyromagnetic ratio divided by 2π

δ Spatial resolution

Δk Sample spacing in *k*-space

$\Delta\Phi_{FULL}$ Image-based 2D phase map

$\Delta\Phi_{AVG}$ Image-based 1D phase map obtained by averaging

$\Delta\Phi_{AVG,M}$ Image-based 1D phase map obtained by averaging and masking

$\Delta\Phi_{REF}$ Phase map obtained from EPI reference scan

$\Delta\omega_{B0}$ Field inhomogeneity

$\Delta\omega_{CS}$ Chemical shift

ϵ Measurement error

θ Radiofrequency pulse (RF) flip angle

κ Sampling position in *k*-space

λ Regularisation parameter

μ Permeability

μ_0 Permeability of the free space

μ_r Relative Permeability

ρ Voxel index

ξ Coil index

ν Signal density in the transversal plane

ρ_A Area density

Φ_c Concomitant maxwell phase

χ Magnetic susceptibility

Ψ Receiver noise matrix

ω_0 Larmor frequency

Ω Object indicator map

List of Acronyms

ADC	Analog-Digital converter
BOLD	Blood oxygenation level dependent
BW	bandwidth
CG	conjugate gradient
DWI	Diffusion weighted imaging
FOV	Field of view
EMF	Electromotive force
EPI	Echo-planar imaging
EPI	Echo-planar imaging
FFT	Fast Fourier transform
fMRI	functional Magnetic resonance imaging
FLASH	Fast Low-Angle Shot
FID	Free induction decay
GRE	Gradient echo imaging
IFFT	Inverse fast Fourier transform
MRI	Magnetic resonance imaging
nRMSE	Normalised root-mean-square error
NUS	Non-Uniform sampling
PI	Parallel imaging
RO	Read-Out direction
PE	Phase-Encode direction
RF	Radiofrequency pulse
ROI	Region-of-interest
SAR	Specific Absorption Rate
SE	Spin echo
SENSE	Sensitivity encoding
SNR	Signal-to-Noise ratio
VSM	Voxel shift map
z	Longitudinal z direction

1 | Introduction

1.1 Prior Art

Magnetic resonance imaging (MRI) is still a vital and fast evolving medical imaging modality. Especially, due it its excellent soft tissue contrast it is often one of the most preferred diagnostic imaging technologies. Among the different data sampling schemes used is EPI [1], which is one of the fastest and most efficient sampling schemes, representing the workhorse for many time and motion critical applications. Thus, major applications for EPI can be found in functional Magnetic resonance imaging (fMRI) which can map the variety of brain activity patterns and diffusion-weighted MRI which finds applications in brain mapping too (fiber tracking), but which is also key in oncology driven approaches such as tumour identification and characterisation.

Although introduced more than 3 decades ago and already adapted to daily clinical practice, EPI definitively deserves and can benefit from some further improvements. Using the principle of parallel reception, which increases the number of independent measurements and thus data redundancy, modern and advanced model-based image reconstruction approaches can help to further improve image quality, taking imperfections of the measurement process appropriately into account enforcing data consistency.

One of the major EPI artefacts are Nyquist ghosts, also termed N/2 ghosts. Due to the opposing echo readout of adjacent k-space lines, eddy currents induce a phase error that projects ghosts half a field-of-view away. On most commercially available scanners, these phase-errors are addressed by obtaining additional EPI reference data [2] [3] used to perform correction. Therefore, the imaging protocol is prolonged. Furthermore, the reference data loose validity during the acquisition process, due to effects like coil heating associated with a change of eddy currents.

Meanwhile, there are new approaches in literature [4] [5] showing how to obtain information about the phase error only using the measurement data itself. These approaches form the starting point for the algorithm implemented in this work.

1.2 Thesis Objectives

When EPI was introduced in 1977 by Sir Peter Mansfield [1], the simple yet efficient formulation of gradient based k-space encoding [6] served as the basis of image reconstruction. While the core assumptions of this reconstruction can still be regarded as valid, the technical development of the last decades suggest an extension of this model. Therefore, one of the goals of this work is to revisit the image acquisition and to appropriately integrate the most important effects into the measurement model.

Using the principles of Parallel imaging (PI) [7], the model should account for multiple spatially varying coil sensitivities Sensitivity encoding (SENSE) [8]. Furthermore, modern sampling schemes like non-uniform sampling should be considered. One of the main artefacts of EPI are field inhomogeneity induced geometric distortions. Information about these inhomogeneities should be obtained by additional measurements and integrated into the reconstruction.

The core objective represents the calculation and integration of image-based phase maps, modelling the eddy current induced *odd*/*even* phase errors. This leads to a measurement data driven reconstruction of phase errors and image data. Therefore, this makes the need for an explicitly acquired EPI reference scans obsolete.

Using an iterative image reconstruction, the overdetermined equation system can be solved in

an Signal-to-Noise ratio (SNR) optimal way. A CG algorithm is especially suited, since it converges without special provisions as long as the system is positive definite [9]. It should be studied how all mentioned effects can be integrated into the reconstruction, also considering the numerical efficiency of the integration.

The offline reconstruction framework should be able to deal with real scanner data, to validate it against the scanner reconstruction employing EPI reference data. This validation should be carried out using a set of useful phantom and in vivo measurements. The objective is to study if image-based phase maps enable a reconstruction which is qualitatively equivalent or better compared to a reconstruction using EPI reference data. This analysis should be done for measurements with different acceleration factors.

1.3 Outline

As the goal of this work is to revise the EPI image reconstruction, in the first chapter the physical basis of MRI and EPI are explained. Starting from the principles of *nuclear magnetic resonance*, selective excitation, spatial encoding and data sampling are introduced. Following one of the core MRI developments of the last decades is introduced, which is termed PI. Using PI, SNR is improved and accelerated measurements are enabled.

The third chapter summarises Spin echo (SE) and Gradient echo imaging (GRE) pulse sequences, which represent the most important pulse sequences used for EPI measurements. Furthermore, the considered imaging artefacts are being introduced. One on hand, field inhomogeneities should be considered, while the core objective lies in the consideration of eddy current induced Nyquist ghosts, which are the primary reason for the need of EPI reference scans. The chapter concludes by explaining the modelling of an EPI measurement and by the introduction of an iterative solution of such a model.

Chapter 4 summarises the methodology. First the software framework is introduced and the obtained measurements stated. Second the preparation of the data to be used in the iterative algorithm is shown. Furthermore, the integration of field maps in that scheme is introduced. The chapter concludes with the integration of the obtained phase maps.

Chapter 5 shows the most important properties of the obtained phase maps. Furthermore, it is shown that already for moderate acceleration factors the obtained phase maps tend to show artefacts which propagate into the final reconstruction. To alleviate these effects, phase map averaging is introduced and it is shown that such an averaged phase map yields good reconstruction results. It is demonstrated that the integration of field maps into the reconstruction can successfully reconstruct data being subject to strong field inhomogeneity effects. The chapter completes by studying the reutilisation of the obtained phase maps for multislice reconstructions.

The thesis closes with the discussion of the obtained results and a conclusion.

2 | Theoretical Background

2.1 Nuclear Magnetic Resonance

Nuclear magnetic resonance is a resonance phenomenon which arises in atoms that have either an odd number of protons or neutrons. To generate sufficient detectable signal, the to be imaged proton has to be abundant in adequate quantities. For Magnetic Resonance Imaging of the human body the most important atom is ^{1}H, as it is bound in water (H_2O). Therefore, it represents around 50% - 75% of the human body. Other relevant atoms include ^{23}Na and ^{31}P. In the context of this work only imaging of ^{1}H is considered.

2.1.1 Polarisation and Resonance

All atoms intrinsically have the property of spin. While for atoms with an even number of protons and atoms the spin angular momentum $S = 0$, for the mentioned above atoms S can take integer values parameterised by the magnetic quantum number l. The magnetic quantum number l only takes integer values. Therefore, S takes integers values with $\hbar$ being the constant of proportionality, $S = \hbar l$. Associated with S is a magnetic dipole moment p_{DP}. Both properties are connected linearly by the so called gyromagnetic ratio γ, hence $p_{DP} = \gamma S$. The gyromagnetic ratio differs for nuclei, in the case of ^{1}H it is found to be $\gamma = 42.575 \frac{MHz}{T}$.

It is crucial to keep in mind that while these odd proton numbered nuclei will experience a non-zero magnetic moment, on average the spins will be oriented randomly and the resulting magnetisation vector summed over a unit volume $\mathbf{M} = \sum_{i=0}^{N} p_{DP,i}$ will be zero. However, by applying a strong $\mathbf{B}_0$ field (for scanners used in in vivo applications usually between 1.5T and 7T) a macroscopic magnetisation $\mathbf{M}$ can be created, because the protons will be aligned in the direction of $\mathbf{B}_0$. This basic notion is graphically visualised in fig. 2.1 - here it is also stated that the z direction is also called longitudinal, while the xy plane is referred to as the transversal plane. This nomenclature will be used in the following chapters of this work.
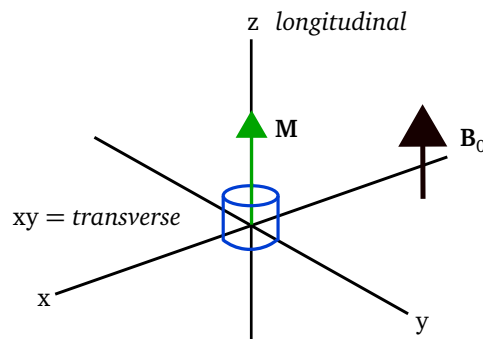
Figure 2.1: Orientation of net magnetisation.
The applied $\mathbf{B}_0$ field creates a net magnetisation $\mathbf{M}$ in a unit volume, shown in blue. The schematic is shown in the laboratory frame of reference. Adapted from [10].

When this magnetic flux density $\mathbf{B}_0$ is present, a magnetic dipole moment p_{DP} has a potential energy of $E_p = -p_{DP}\mathbf{B}_0$. For ^{1}H the possible spin quantum numbers are $l = -1/2, 1/2$. Therefore, two

energy states exist. The so called parallel and anti-parallel states have a slightly different energy, which is determined by the Boltzmann constant and the absolute temperature T_{abs}. Using the Larmor frequency ω_0 introduced below the spin excess can be calculated by spin excess $\approx N \frac{\hbar \omega_0}{2 k_{BC} T_{abs}}$. Therefore, for a magnetic field of strength $3T$ the excess is around 10 in a million, which explains why the to be imaged proton density has to be abundant in large numbers and SNR is a problem [11].

Another intrinsic feature of a magnetisation vector $\mathbf{M}$ when exposed to a static $\mathbf{B}_0$ can be exhibited when $\mathbf{M}$ and $\mathbf{B}_0$ point in different directions. While torque can be calculated with the cross product $p_{DP} \times \mathbf{B}_0$, the angular momentum is the time derivative of this cross product. Combining $\mathbf{M} = \gamma S$ with $\frac{dS}{dt} = p_{DP} \times \mathbf{B}_0$ leads to

$$\frac{d\mathbf{M}}{dt} = \mathbf{M} \times \gamma \mathbf{B}_0 \,. \tag{2.1}$$

From eq. 2.1, which represents the basic equation of motion for the magnetisation and which shows similarities to classic mechanics, we deduce the most famous equation in MRI, where γ is known as the *Larmor frequency*

$$\omega_0 = \gamma \mathbf{B}_0 \,. \tag{2.2}$$

Therefore, we conclude that by applying $\mathbf{B}_0$ the magnetisation $\mathbf{M}$ will rotate in resonance with the frequency ω_0.

2.1.2 Relaxation and Bloch Equation

To acquire an MR signal an excitation pulse RF has to be added. This RF pulse is also denoted by $\mathbf{B}_1$ and is orthogonal to $\mathbf{B}_0$. Therefore, $\mathbf{M}$ is rotated by a specific angle through the application of the excitation $\mathbf{B}_1$ as depicted in fig. 2.2. It should be noted that in this case $\mathbf{B}_1$ strength and duration are picked in a way that the flip angle $\theta = 90°$.
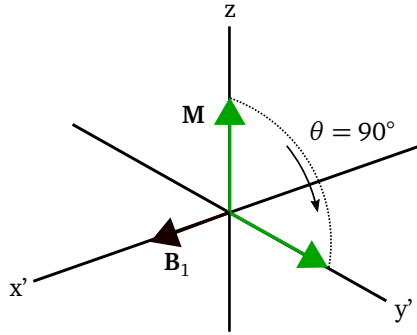
Figure 2.2: Rotation of net magnetisation to the transverse plane.
$\mathbf{B}_1$ induces rotation of $\mathbf{M}$ towards the transverse plane. Note that the schematic is shown in the rotating frame, rotating at the *Larmor frequency*. Adapted from [10].

This behaviour is equivalent of stating that $\mathbf{M}$ is flipped in the transversal xy plane and can then be denoted as $\mathbf{M}_{xy}$. The flipped magnetisation $\mathbf{M}$ will continue to precess at the *Larmor Frequency*. This precession phenomenon is characterised logically by 2 time constants: constant T_1 which characterises the return to the z-axis and constant T_2 which characterises the decay in xy plane. T_1 is also called the spin-lattice time constant [10], because it is governed by the energy exchange between the nuclei and surrounding lattice. Therefore, T_1 is the time constant which describes how fast $\mathbf{M}_z$ is restored to the equilibrium nuclear magnetisation $\mathbf{M}_0$, which is the lowest possible energy state [10]. Following a $\mathbf{B}_1$ excitation $\mathbf{M}_z$ follows

$$\mathbf{M}_z = \mathbf{M}_0 \left(1 - e^{-t/T_1}\right) \,. \tag{2.3}$$

T_2 depends on the transversal $\mathbf{M}_{xy}$ component and is also denoted as spin-spin time constant, as it's governed by the loss of phase coherence of $\mathbf{M}_{xy}$. Because $\mathbf{M}_z$ is the lowest energy state the

the magnetisation always has to return to this state. Universally the relation $T_2 \leq T_1$ applies. The dependence of $\mathbf{M}_{xy}$ on T_2 can be described by

$$\mathbf{M}_{xy} = \mathbf{M}_0 \, e^{-t/T_2}. \tag{2.4}$$

Combining eq. 2.1, eq. 2.4 and eq. 2.3, the Bloch equation can be derived. It describes the dynamics of the nuclear magnetisation and reads

$$\frac{\mathrm{d}\mathbf{M}}{\mathrm{d}t} = \mathbf{M} \times \gamma B - \frac{\mathbf{M}_x \mathbf{i} + \mathbf{M}_y \mathbf{j}}{T_2} - \frac{(\mathbf{M}_z - \mathbf{M}_0)\mathbf{k}}{T_1}, \tag{2.5}$$

where $\mathbf{i}, \mathbf{j}, \mathbf{k}$ are the unit vectors in x, y, z direction. Another crucial rationale derived from eq. 2.5 is that T_1, T_2 and the proton density v - which is linearly dependent on $\mathbf{M}_0$ - form the basic parameters of contrast generation in MRI.

In reality T_2 does not represent the actual decay of the transversal magnetisation. The decay is governed by T_2^* which depends on external field effects such as field inhomogeneities and can be modelled using

$$\frac{1}{T_2^*} = \frac{1}{T_2} + \frac{1}{T_2'}. \tag{2.6}$$

It is possible to reverse the effect of T_2', which leads to Spin-Echo SE, see sec. 3.2.1.

By placing receiver coils oriented to detect these changes in the xy plane an Electromotive force (EMF) will be induced into the receiver coils. The generated time signal is called the *free induction decay* (FID). Following Faraday's Law of Induction $\nabla \times \mathbf{E} = \frac{\partial \mathbf{B}}{\partial t}$ the precessing magnetisation will induce an EMF in the surrounding receiver coils, which depends on the rate of change of flux ϕ. Thus, we conclude $EMF = -\frac{\partial \phi}{\partial t}$.

While the upper explanation make clear how a measurable MRI signal can be generated, the last thing that has to be considered is how to make the origin of the measured EMF locatable. To reconstruct an image, localisation techniques have to be added. The smallest unit in a three dimensional MRI image, which is represented by a signal density v, is called a voxel. To achieve this spatial localisation linear magnet fields generated by gradients are used in addition to $\mathbf{B}_0$.

2.2 Image Acquisition and Imaging Parameters

2.2.1 Coordinate System

Before introducing methods to selectively excite voxels and add spatial localisation, the standard coordinate system used in this work shall be stated. It has to be noted that different conventions exist, as e.g. the orientation of the z-axis can be different in radiologic and neurologic publications.

In general, it is possible to state the coordinates of the MRI scanner in either in the logical or physical coordinate system [12]. The physical coordinate system corresponds to the x, y, z coordinates and is defined using the geometry of the magnet and the gradient coils.

For the definition of the nominal gradients it is common to use a logical coordinate system, which is described by the Phase-Encode direction (PE), Read-Out direction (RO) and *slice-selection* gradients.

As shown in fig. 3.1 the patient is placed head first into the gantry on a sliding patient table. Assuming a single slice image and z value is fixed. The remaining two coordinates are described using the x and y coordinates.

Without any loss of generality, in this work the PE direction corresponds to the x and the RO direction to the y axis. All in vivo results presented are transverse slices, i.e. parallel to the xy plane. The origin of the logical coordinate system is referred to as the *isocenter*.

2.2.2 Selective Excitation

For a usual imaging setup one slice in Longitudinal z direction (z) is selectively excited. This can be achieved by adding a gradient G_z. By using a RF pulse with a rectangular frequency spectrum which shares the width of the desired slice to be excited only a selective excitation will occur. From

standard signal processing literature it is well known that the time-domain representation of a rectangular function is a sinc function. Therefore, it is infinite and not realisable. Consequently, the "design" of such a RF function has to be performed with a finite support and special care, see e.g. [11] for further information.

As already mentioned is the EMF induced in the receiver coils motivated from the rotating magnetisation vector $\mathbf{M}(x, y)$. As the transverse $\mathbf{M}(x, y)$ is rotating in the xy plane it can also be written as $\mathbf{M}(x, y) = \mathbf{M}_x(x, y) + j\mathbf{M}_y(x, y)$. This gives the notion that $\mathbf{M}(x, y)$ is a complex signal but results only from the physical rotation in the xy plane. Keeping in mind that a 2D imaging method respectively selective excitation is applied, only the magnetisation within a slice is excited. A plane centred at $z = z_o$ of thickness Δz contains the signal density $v(x, y) = \int_{z_o - \Delta z/2}^{z_o + \Delta z/2} \mathbf{M}^o(x, y, z) \, dz$. The recorded signal is based on this integral over z. If only the described selective excitation would be used, destructive interference originating from the phase dispersion across the slice. Therefore, a slice refocusing gradient has to be used right after the selective excitation gradient. This refocusing gradient has opposite polarity to G_z and half the area of the applied G_z and time product.

$\mathbf{M}^o(x, y, z)$ is the initial condition and $v(x, y)$ is dependent on T_1, T_2, the proton density and the timing.

2.2.3   Spatial Encoding and k-space

By adding a gradient G_x, which is the so called readout gradient and a phase encoding gradient G_y, one arrives at the total formulation for the FID following

$$s(t) = \int_x \int_y v(x, y) \, e^{-j\gamma G_x(t) \, x \, t} \, e^{-j\gamma G_y(t) \, y \, t} \, dx dy \,. \tag{2.7}$$

Equation 2.7 shows that every voxel in the slice can be identified by a unique frequency and phase component. Furthermore, we clearly see similarity to a Fourier transformation. Indeed, we set up the gradients G_x, G_y and G_z in the described way. Using the so called *k-space* formalism where k represents the spatial-frequency variable, see [11], we substitute $k_x(t) = \gamma \int_0^t G_x(\tau) \, d\tau$ and $k_y(t) = \gamma \int_0^t G_y(\tau) \, d\tau$. Consequently, we arrive at the signal equation

$$s(t) = \int_x \int_y v(x, y) e^{-jk_x(t) x} e^{-jk_y(t) y} \, dx dy = \mathscr{F}_{2D}\{v(x, y)\} \,. \tag{2.8}$$

This equation summarises on of the most crucial features of the MRI gradient setup and the induced emf: the measured signal is the 2D Fourier transform of the magnetisation vector density!

To ensure readability while maintaining a compact form for all future equations, we reformulate eq. 2.8 using the spatial vector $\mathbf{r}$, as

$$s(t) = \int_{\mathscr{V}} v(\mathbf{r}) e^{-j\mathbf{k}(t)\mathbf{r}} d\mathbf{r} \,. \tag{2.9}$$

In general two 1D localisation methods are combined, which means frequency encoding in one and phase encoding in the other direction. This method, used on most of todays commercial scanners, is called spin-warp method. In practical terms this means that every readout line is collected using the same frequency encoding gradient G_{RO}. Readout lines differ only in an additionally applied phase encoding gradient G_{PE}.

By application of the phase encoding gradient G_y for a period t and following $k_y(t) = \gamma \int_0^t G_y(\tau)$ the k-space trajectory moves to a certain line in k space. In a similar manner the RO gradient G_x is applied during readout. Subsequently, stacking these readout lines in an array and applying a 2D FFT is the simplest method of obtaining an MRI image.

The time between the RF excitation pulse and the echo is defined as the echo-time TE, and the time between the consecutive RF excitation pulses the repetition time TR. This idea summarises the general idea of an MRI image acquisition. Spatially dependent gradients G_x, G_y and G_z are set up in addition to the strong constant field B_0 in z-direction. Using a B_1 to excite a slice selectively with a frequency matched RF function, one can record a signal $s(t)$ which equals the 2D Fourier transform of $v(x, y)$ at some spatial frequency. Therefore, $s(t)$ is dependant on the gradients and time integrals

applied. $v(x, y)$ is a function of T_1, T_2 and the proton density. Therefore, our generated image contrast depends on one of these 3 parameters.

2.2.4   Data Sampling

The Field of view (FOV) is inversely related to the sampling rate Δk as defined in eq. 2.10, where i stands for one of the cartesian coordinates. As usual the Nyquist sampling criterion has to be taken care of. Because the MR signal is sampled in the frequency (k) domain, aliasing will occur in the spatial domain. In the following sec. 2.3 deliberate aliasing will be introduced, as undersampling reduces the total scanning time and the occurring aliasing can be corrected using PI techniques, see sec. 2.3. The FOV in one cartesian dimension i is defined as

$$FOV_i = \frac{1}{\Delta k_i}. \tag{2.10}$$

The spatial resolution δ can be explained using the number of sampled points N in a FOV. Therefore, $\delta_i = \frac{FOV_i}{N_i}$, what can also be expressed as

$$\delta_i = \frac{1}{2k_{i,max} + \frac{\Delta k_i}{2}}. \tag{2.11}$$

Fig. 2.3 shows the relation between FOV in spatial and frequency k-domain.
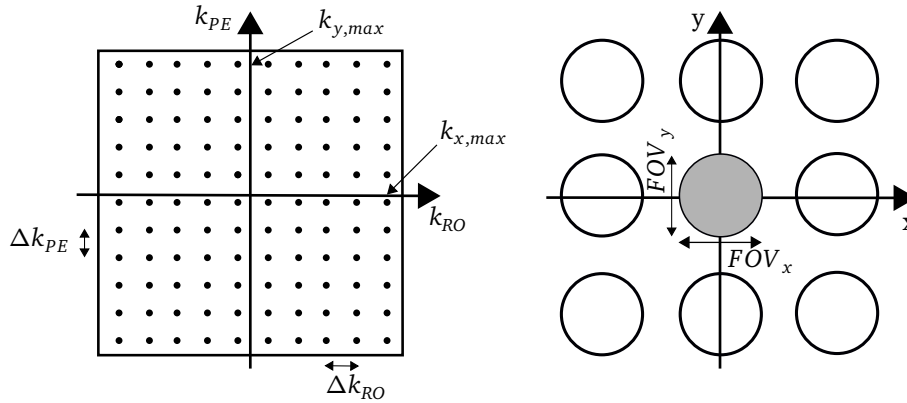
Figure 2.3: Sampling in k-space and corresponding replication in object domain.
The white circles are the object replicas and the grey circle is the object itself. If the sampling intervals in k-space are chosen too small ($\Delta k < \frac{1}{FOV}$), the object replicas and the object will superimpose. Adapted from [10].

2.3   Parallel Imaging

Parallel Imaging was originally referred to as *Phased Array Imaging*. The PI concept was introduced in 1990 by Roemer *et al.* [7]. When the PI acquisition was initially presented, its main advantage was seen as an increase in SNR. This notion can be derived from the fact that most noise in modern MRI can be attributed to thermal noise in the subject. It is clear that this noise originates from the whole body. Therefore, if each coil is only sensitive to a certain area it also picks up less noise. This underlying idea of PI is visualised in fig. 2.4 where the blue coloured areas represent the picked up noise. This notion in addition to the remarks made in sec. 2.3.3, can be summarised in a straightforward and intrusive way. As the noise can be modelled as white and gaussian distributed, spatially varying coil sensitivities reduce the noise that is picked up by the receive coils. Therefore, the SNR increases.
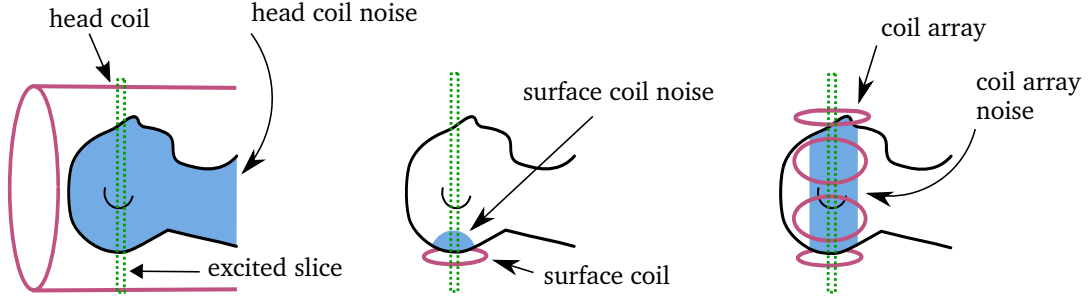
Figure 2.4: Parallel imaging coil setup.
Parallel imaging coil setup: Note that for an array of surface coils - shown on the right - the picked up cumulative noise is greatly reduced compared to the initial setup on the left. This reduction stems from the spatially reduced surface coil sensitivities and the noise being modelled as white and gaussian distributed.

2.3.1 Roemer Reconstruction

The concept of having 2 receiver coils with spatially varying coil sensitivities is display in fig. 2.5.
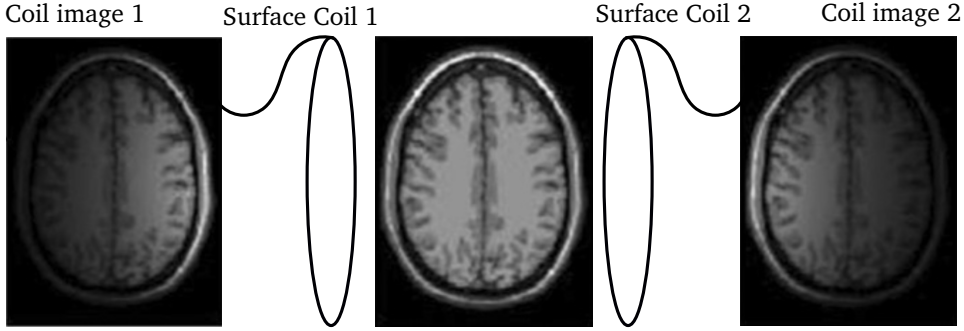
Figure 2.5: Concept of two receive coils with spatially varying coil sensitivities.
The figure illustrates the concept of using two coils with spatially different coil sensitivities to image an object. To yield the shown coil image, the collected k-space data is 2D-FFT transformed. To combine the coil images for the final reconstruction, reconstruction schemes Sum-of-Squares, Roemer or SENSE are used. For the two latter the spatial coil sensitivities have to be measured separately before the actual imaging sequence. Note that in a modern head imaging setup at least around a dozen surface coils are used. Adapted from [13].

Rewriting our signal eq. 2.9 using multiple receive coils, we obtain per coil ξ

$$s_\xi(t) = \int_{\mathcal{V}} c_\xi(\mathbf{r}) \, v(\mathbf{r}) \, e^{-j\mathbf{k}(t)\mathbf{r}} d\mathbf{r}, \qquad (2.12)$$

where $c_\xi(\mathbf{r})$ denotes the complex coil sensitivity c at spatial position $\mathbf{r}$. Surface coils have a rapidly weakening $\mathbf{B}_1$ receive field. The spatial variation of sensitivity maps is usually assumed to be smooth [8], see sec. 4.2.2 for further remarks on the calculation of sensitivity profiles.

The receive field is a function of distance away from the coil surface. Therefore, the image intensity in every coil image p_ξ varies according to the surface coil sensitivity as shown in fig. 2.5. Neglecting measurement noise, the discretised measured data per coil ξ is

$$m_{\xi,i} = s_\xi(t_i) \quad i = 1, ..., n_d. \qquad (2.13)$$

The sensitivity encoding of the coil is combined with the classic Fourier encoding. This leads to the term $\mathbf{E} = e^{j\mathbf{k}\mathbf{r}} c_\xi(\mathbf{r})$, per voxel located at $\mathbf{r}$. Therefore, this type of encoding can be seen as a hybrid encoding, utilising both gradient and sensitivity encoding.

As fig. 2.5 suggests in PI every coil picks up signal. Thus, n_c images are obtained. We reformulate the reconstructed signal density vector for $\xi \in \{0, ..., n_c\}$ as

$$p_\xi(\mathbf{r}) = c_\xi(\mathbf{r}) \, v(\mathbf{r}). \tag{2.14}$$

Stacking these pictures into matrix form we obtain

$$P = C \, \mathbf{v}, \tag{2.15}$$

which leads to the intrusive question of how to solve this eq. with respect to $\mathbf{v}$. Simply summing all coil images would lead to image artefacts such as regional signal cancellation, as the sensitivity c is complex. An artefact free image can be obtained using the sum-of-squares method. Thus, $v(\mathbf{r}) = \sqrt{\sum_\xi^{n_c} |p_\xi(\mathbf{r})|^2}$. The biggest benefit of this approach is that the sensitivity maps don't have to be known and consequently initial calibration scans are not compulsory. Calibration scans were seen as a major drawback in the past because they were time-consuming.

In general, it is not possible to obtain an exact solution as the system of eq. 2.15 is overdetermined and an exact inversion doesn't exist. Using the *Moore–Penrose* pseudo-inverse for the overdetermined case [14], we derive

$$\begin{aligned} C^H P &= C^H C \, \mathbf{v} \\ \mathbf{v} &= (C^H C)^{-1} C^H P \end{aligned} \tag{2.16}$$

This approach gives a solution which is optimal in the least square sense. It has optimal SNR and preserves the phase.

2.3.2 SENSE

Stemming from the Roemer reconstruction, SENSE is a generalisation of eq. 2.16 [8]. This generalisation can also be applied in the case of undersampling. The basic notion of undersampling is to omit sampling lines, as shown in fig. 3.4. Besides the basic benefit of PI nowadays the possibility of undersampling the k-space facilitates rapid acquisition schemes used in the applications described in chap. 3.1. This undersampling will lead to aliasing in the coil images p. This behaviour is shown on the left side of fig. 2.6.

The aliasing typically occurs in PE respectively y direction as the phase encoding blips are costly and consequently the number of PE steps is decreased by undersampling. It is possible to unfold the aliasing in image space. This algorithm is shown in 2.6. In this method the superimposed pixels in vector $\mathbf{a}$ can be separated by multiplying with an unfolding matrix. The aliased vector of pixels $\mathbf{s}$, can be formulated as

$$\mathbf{s} = \tilde{C}\mathbf{a}, \tag{2.17}$$

using the $n_c \times n_p$ matrix of coil sensitivities at the aliased positions $\tilde{C}$ and the initial pixel values $\mathbf{a}$. The system is solvable when $n_c \geq n_p$. Using the *Moore-Penrose* pseudoinverse, eq. 2.17 can be solved with respect to the n_p pixels $\mathbf{a}$:

$$\mathbf{a} = (\tilde{C}^H \tilde{\Psi}^{-1} \tilde{C})^{-1} \tilde{C}^H \tilde{\Psi}^{-1} \mathbf{s}. \tag{2.18}$$

$\tilde{\Psi}$ is the receiver noise matrix for the involved channels in $\tilde{C}$. The noise levels and correlations are only considered to minimise noise in the final image. To eliminate the noise matrix it can be taken as identity which leads to skipping of noise assessment. Furthermore, using *Cholesky decomposition* virtual receiver channels can be generated which then exhibit unit noise levels and no mutual noise correlation. $\tilde{\Psi}$ can be measured using a statistical analysis of reference samples collected in a calibration measurement prior to an actual MRI signal [9].

It should be emphasised again that following eq. 2.13 the SENSE reconstruction integrates the coil sensitivities implicitly in the encoding function $\mathbf{E} = e^{j\mathbf{kr}} c_\xi(\mathbf{r})$, hence the name *Sensitivity encoding*.
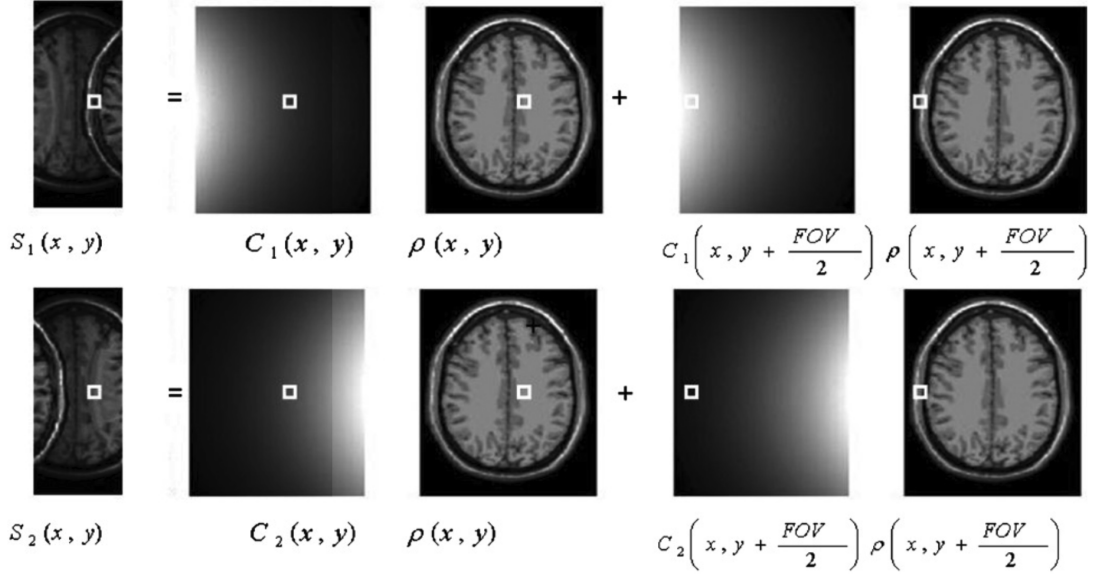
Figure 2.6: Schematic of aliasing in a parallel imaging setup.
The aliased pixel in the image from coil1, marked by a white square, contains the sum of the spin density v at location 1 and the spin density v at location 2 multiplied by the coil sensitivity at location 2, likewise for coil 2. If the coil sensitivities are known (the maps shown) then these equations are solvable for the spin density at both locations. A different set of equations can be constructed for each pixel in the sub-sampled images [13].

2.3.3   Noise Considerations

The main source of noise in MRI is of is of thermal origin. It stems from Brownian motion of electrons in a conductor and generates electrical fluctuations in the receive coils. The contributors to this motion are the resistance of the receive coil, the resistance of the human body and the receive electronics resistance. Although it should be noted that most noise originates from the body. In total all three effects can be added and denoted as R, since they have an additive effect on the noise variance. Taking the bandwidth (BW) into account, the noise variance can be calculated as

$$\sigma_m^2 = 4k_{BC} \, T \, R \, BW \, . \tag{2.19}$$

Any signal acquired during an MRI measurement will have an additive effect on the measured signal. Therefore, the noisy signal $\tilde{m}$ can be calculated with

$$\tilde{m}(k) = m(k) + \epsilon(k) \, . \tag{2.20}$$

The measurement error ϵ can be assumed as an *Additive White Gaussian Noise* process. The noise in k as well as spatial domain can be assumed as Gaussian [15].

Using this model, the spectral density $r_\epsilon(f)$ can be derived as $r_\epsilon(f) = \sigma_m^2$, in a discrete measurement setting this result sustains the interpretation that every measured k-space sample has the same noise variance σ_m^2. In image domain, the noise variance will be reduced by the number of voxels $\sigma_0^2 = \frac{\sigma_m^2}{N}$, see [11] for a derivation of this equation. Considering the noise statistics, a single coil acquisition the noise can be modelled as a complex Gaussian process, where the real and the imaginary part have zero mean and equal variance σ_m^2. For most cases the magnitude signal of the reconstructed image is modelled as non-zero mean and consequently as Rician distributed [15]. For background region which exhibit mostly noise contribution the magnitude statistics can be simplified as Rayleigh distribution and with the same approach statistics for regions of very low noise can be considered as Gaussian distributed [10].

To have a quantitative assessment of noise usually the SNR is used. In most technical applications the SNR refers to a signal in relation to noise *power*, in the field of MRI a definition in relation to the noise *standard deviation* is common. Therefore, SNR in a Region-of-interest (ROI) follows

$$SNR = \frac{\text{mean}(\text{ROI}_{signal})}{\text{std}(\text{ROI}_{noise})} . \tag{2.21}$$

Usually the SNR is then converted to $SNR_{dB} = 20\log(\text{SNR})$. The SNR depends on physical and instrumentation parameters - increases e.g. with $\mathbf{B}_0$, the geometry of the receiver coils and the conductivity of the sample. Also the SNR depends on imaging sequence parameters like the scan time, spatial resolution, sequence timing. In general, signal levels increase with ν. To assess the relation to T_1 and T_2, the to be imaged tissue characteristics have to be considered as well. MRI raw data is acquired in k-space, which is an inverse space to the spatial domain. Therefore, increasing the voxel dimensions $\Delta x, \Delta y, \Delta z$ increases the SNR and we obtain

$$SNR \propto \Delta x \Delta y \Delta z \sqrt{N_y T_s} f(\nu, T_1, T_2). \tag{2.22}$$

This linear dependance should be seen as a *rule of thumb*, as it also depends on the spatial-frequency properties of the imaged object and sampling trajectories. In eq. 2.22 $N_y T_s$ can be explained as the *cumulative readout duration*. More signal can be collected when the readout duration is increased. It is clear that the limit of such an increase are T_2^* effects which modulate the decreasing signal amplitude.

Second, unlike a matrix representation of an Fast Fourier transform (FFT), a SENSE reconstruction matrix generally is not unitary. As a consequence, unlike images obtained with one receive coil, the noise level in an image obtained with PI SENSE techniques varies from pixel to pixel due to inter-pixel noise correlation.

The geometry factor g can be calculated [8] per voxel ρ following

$$g_\rho = \sqrt{[(\tilde{C}^H \tilde{\Psi}^{-1} \tilde{C})^{-1}]_{\rho,\rho} (\tilde{C}^H \tilde{\Psi}^{-1} \tilde{C})_{\rho,\rho}} \geq 1. \tag{2.23}$$

The geometry factor characterises the ability to separate pixels superimposed by aliasing and is sometimes referred to as *noise amplification factor*. Together with the reduction factor R it defines an upper bound for the SNR obtained when undersampling is applied. SNR_p^{red} is exhibited when undersampling is performed

$$SNR_\rho^{\text{red}} = \frac{SNR_\rho^{\text{full}}}{g_\rho \sqrt{R}}, \tag{2.24}$$

while SNR_p^{full} is obtained under full Fourier encoding. The reduction factor R is the ratio of reduced number of samples with respect to full Fourier encoding. A reduction factor of $R = 2$ is visualised in fig. 3.4.

3 | Principles of Echo-Planar Imaging

3.1 Applications and Scanner Overview

EPI is mainly used for the imaging of the head. Major applications have been fMRI and Diffusion weighted imaging (DWI). Because it is noninvasive and no ionising radiation is used, fMRI has been the dominant tool for brain mapping research. Using fMRI, brain activity patterns can be mapped using Blood oxygenation level dependent (BOLD) contrast. BOLD contrast can be generated due to the properties of haemoglobin. Haemoglobin is diamagnetic when oxygenated and paramagnetic when deoxygenated. The other major application termed DWI finds applications in brain mapping too but also in fiber tracking. Using additional gradients the diffusion of water molecules, which is then used to generate contrast.

Figure 3.1 shows the system of an MRI system used in this work. The description of the underlying coordinate system can be found in sec. 2.2.1. The head coil array consists of multiple channels and is also shown in fig. 2.4. The different receive channels are located in a circular manner around the head and consists of more than 10 receive channels. The patient or phantom is placed on the movable patient table, which locates the table in a way that the head will be in the *isocenter* of the scanner. The liquid helium cools the main field coils below the critical temperature of around 4.2 K, needed for the superconducting electromagnets of the main field coils. The scanner reconstruction unit processes the acquired data and enables the export of raw data, see sec. 4.1.3.

3.2 Pulse Sequences

The last sections provided an overview of the physical background of MRI, the acquisition and spatial localisation of a signal. The following remarks should give an overview of the actually applied sequences, leading to an understanding of the EPI sequences used to obtain the results of this work. Both SE, introduced in the following sec. 3.2.1 and GRE sequences, sec. 3.2.2 are used for EPI trajectories. Both techniques rely on manipulating the Free induction decay (FID) in a way that an echo is generated instead of recording the FID directly. One of the main advantages of this approach is that the data measurement occurs far away from the excitation which needs high voltages and can hinder the recording of the significantly smaller FID signal.

Restating eq. 2.12 we obtain

$$s(t) = \int_{\mathcal{V}} c(\mathbf{r})\, v(\mathbf{r})\, e^{-j\Phi(\mathbf{r},t)} d\mathbf{r}\,. \tag{3.1}$$

In a practical term the phase accrual term $e^{-j\Phi(\mathbf{r},t)}$ not only considers phase accrual due to gradients, but also due to field inhomogeneities $\Delta\omega_{B0}$ and chemical shift $\Delta\omega_{CS}$. Therefore, it can be divided into these three additive parts

$$\Phi(\mathbf{r},t) = \Delta\omega_{B0}(\mathbf{r})\, t + \Delta\omega_{CS}(\mathbf{r})\, t + \gamma \int_0^t \mathbf{G}(\tau)\, d\tau\,. \tag{3.2}$$
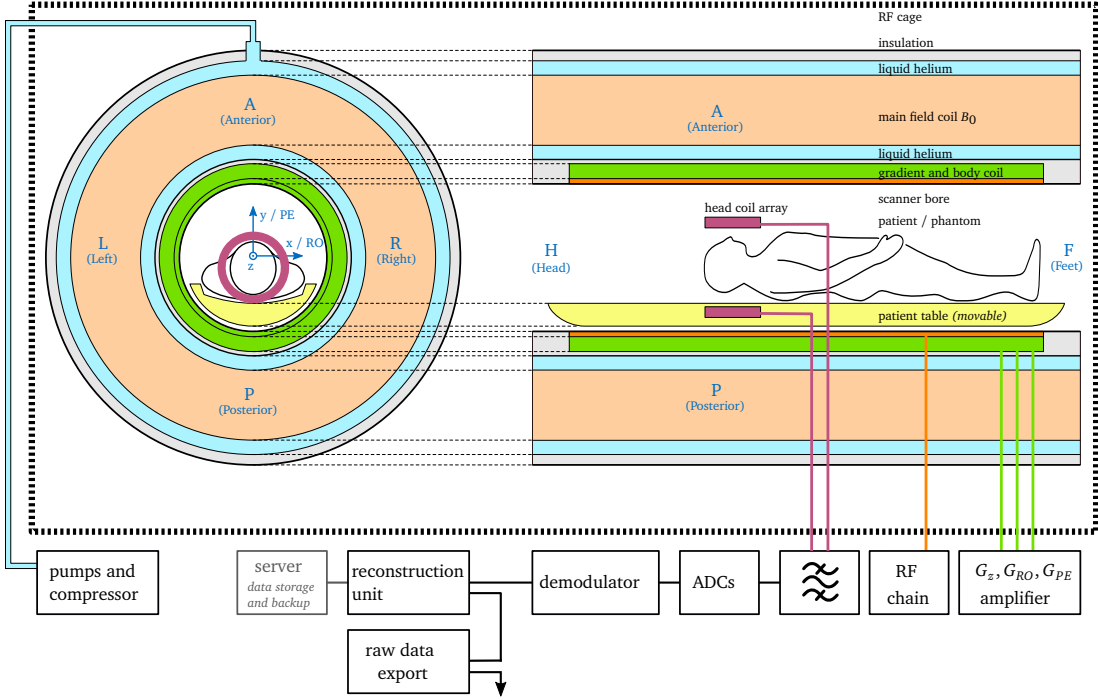
Figure 3.1: MRI system setup.
The Systems components are given in black and the four tomographic imaging directions are stated in dark blue. The head of the patient is located at the *isocenter* of the magnet. The bandpass filtered signal is demodulated and forwarded in the image processing unit. The reconstruction unit has a modular structure. After any module the raw data and certain image parameters can be exported via an output node. See sec. B for an overview of the exported data. Therefore, the output node resembles the input node of the offline reconstruction pipeline.

An echo occurs at the moment when the space-variant phase shifts are minimised. Therefore, a peak in strength and coherence of the signal is observed. While in GRE sequences these peaks are achieved by undoing the phase shifts from gradient fields, SE sequences neutralise the phase shifts due to $\Delta\omega_{B0}$ and $\Delta\omega_{CS}$.

3.2.1 Spin Echo Imaging

As note by eq. 2.6 the external field effects stemming from field inhomogeneities can be reverted by SE sequences. Fig. 3.2a) shows different spins dephasing until the point in time τ, after which the 180° excitation is applied. The phase right before the π excitation can be denoted as

$$\Phi(\mathbf{r}, \tau^-) = [\Delta\omega_{B0}(\mathbf{r}) + \Delta\omega_{CS}(\mathbf{r})]\tau^-. \tag{3.3}$$

This second excitation negates the spin phases. The phase right after the π excitation is therefore given by

$$\Phi(\mathbf{r}, \tau^+) = -\Phi(\mathbf{r}, \tau^-). \tag{3.4}$$

Consequently, all of the spins will be realigned at time 2τ. This realignment is called a spin echo.

3.2.2 Gradient Echo Imaging

In contrast to SE imaging presented in the section above, GRE imaging does not negate the phase shift from field inhomogeneities and chemical shifts, but only from gradient fields itself. When the gradient field reverses at τ, the phase wrapping accrued from 0 to τ starts to unwind. This means that the GRE sequence only rephase spins that are also dephased by the gradient application.

a)

b)
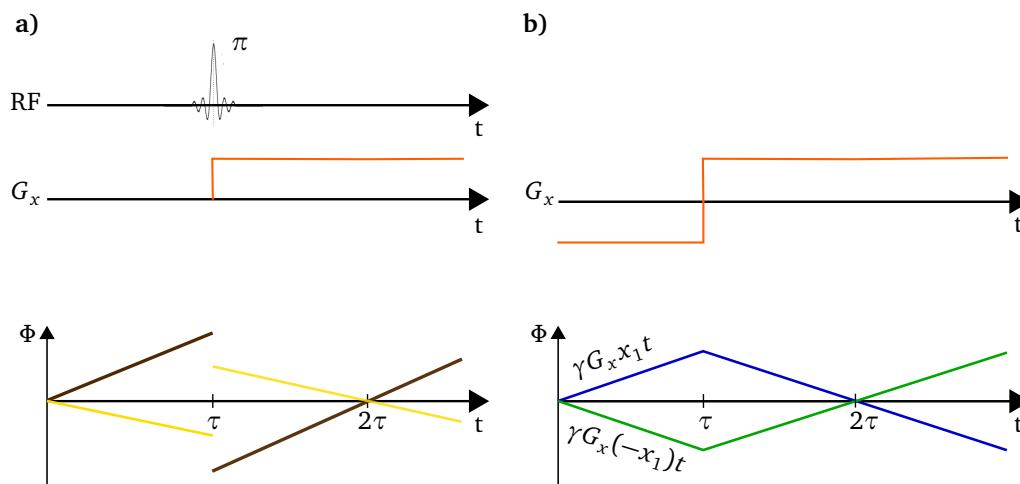
Figure 3.2: Phase evolution plots of Spin Echo and Gradient Echo sequences.
a) SE phase plot: Spin Echo-Spins at different resonant frequencies disperse in phase. At time τ, the 180° pulse reverses the phase about τ. The slope of phase accrual remains the same after the 180° pulse and at time 2τ, the spins rephase and an echo occurs.
b) GRE phase plot: Gradient Echo-Phase progression of spins at x_1, 0, $-x_1$. Spins at higher frequency from time 0 to τ (gains phase), lower frequency from τ (loses phase). At time 2τ, spins have rephased producing an echo.
Adapted from [10].

Therefore, the dephasing created is also symmetric, as noted by spins at x_1 and $-x_1$. Having a perfect main field inhomogeneity and no chemical shift the phase trend can be described by

$$\Phi(\mathbf{r}, t) = \gamma \int_0^t \mathbf{G}(\tau) \, d\tau \,. \tag{3.5}$$

Considering a constant readout gradient, fig. 3.5b) represents the phase accrual from 0 to τ. After the gradient reverses, the spins start to unwind and an echo is formed at 2τ. If the gradient is applied longer the spins start to dephase again after the time point 2τ.

As the spin echo dephasing due to field inhomogeneities and chemical shift is not compensated, GRE sequences are especially sensitive to $\Delta\omega_{B0}$ and $\Delta\omega_{CS}$ effects. This explains that GRE sequences produce T_2^* weighted contrast, while SE sequences measure contrast modulated by T_2 constants.

3.2.3 Echo Planar Imaging

EPI is an imaging technique where a whole slice is acquired following a single RF excitation or a small number of RF excitations. Using only one excitation is also denoted as *Single-Shot* EPI, consequently the use of multiple excitations is called *Multi-Shot* EPI. In this work only *Single-Shot* EPI sequences were considered. Thus, the usage of the term EPI implicitly contains this choice.

Fig. 3.3 shows part of SE EPI sequence. In general it is possible to obtain images with GRE as well as SE excitation and the following excitations are equivalent for both contrast mechanisms. To achieve an EPI trajectory at first a slice of several millimetre thickness is selectively excited using a gradient G_z. Afterwards, both G_{RO} and G_{PE} are applied to move to the lower left spatial frequency in Fourier domain. Following the π rephasing pulse (for SE sequences), line by line is being readout by applying a readout gradient G_{RO} of alternating polarity. The echoes are sampled using an Analog-Digital converter (ADC). To move from one line to another a so called *phase-blip* G_y is applied. As mentioned for a *Single-Shot* EPI acquisition a whole slice is imaged following a single RF excitation. Therefore, fig. 3.3 would contain as many *phase-blip* as sampled echoes.

An intrinsic problem of that approach is that any phase error exhibit by measured voxels is accrued, since for *Single-Shot* EPI all voxels are recorded in a successive fashion. Therefore, voxels lying at the end of the readout train are exposed to more phase errors than voxels recorded close to the RF excitation. One of the core advantages of EPI is imaging speed. Additionally, using EPI

several artefacts arise. All of these artefacts, described in the following sections, arise in the PE direction. This behaviour stems from the fact that due to the high sampling rate of the ADCs the BW in RO direction is high, while the BW in PE direction is very low.
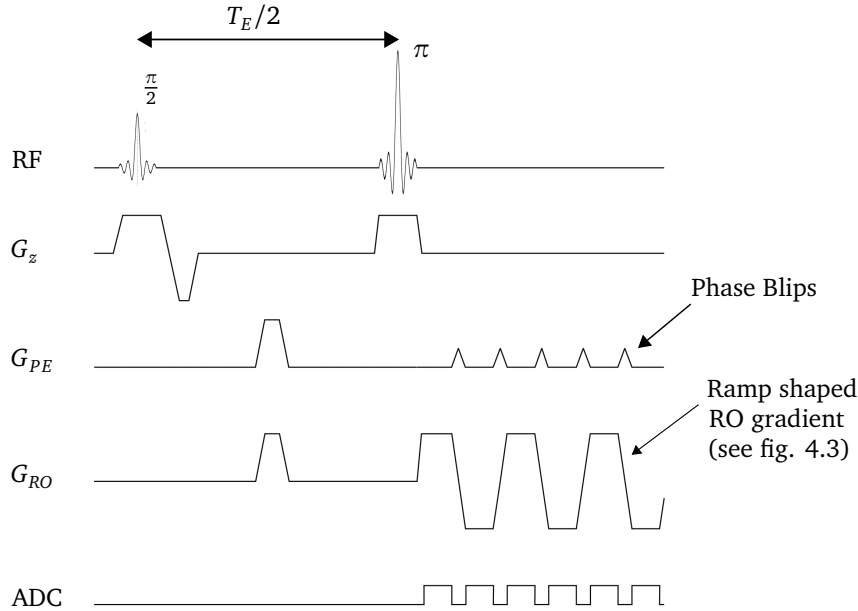
Figure 3.3: A Spin-Echo EPI imaging sequence.
Part of a SE EPI Imaging Sequence. In the experiments conducted for this work more than a hundred echoes per imaged slice were collected. The time difference between the $\frac{\pi}{2}$ and π pulse is defined by half the *echo time*, denoted as $\frac{T_E}{2}$. As the ratio between T_E and T_2 determines the amount of collectable signal, the slopes of the ramp shaped gradients are sampled. See fig. 4.3 for further explanations. The *phase blips* are applied to reach the next readout line. Adapted from [11].

One of the technological challenges in the development of EPI were high hardware requirements. Performant gradient coil systems, gradient amplifiers and ADCs are needed [3]. The readout of a whole slice has to executed before the T_2 respectively T_2^* weighted signal has diminished. Using PI techniques it has been a major improvement because only a fraction of the imaging plane has to be sampled. Such an undersampled trajectory is displayed on the right of fig. 3.4.

The reduction factor R denotes the ratio of sampled phase-encoding steps in relation to the total number of phase-encoding steps. Therefore, full cartesian sampling is equivalent to $R = 1$, while sampling every second phase-encoding step results in $R = 2$. This is visualised in fig. 3.4. As for most of the MRI signal is recorded at $k = 0$, the phase-encoding step at $k = 0$ is never omitted.

Using a reduced number of acquisition steps has several major advantages. First of all, the total imaging time is reduced approximately by $\frac{1}{R}$. The reduced imaging time can be used for better temporal resolution. Furthermore, because a single slice is imaged faster, the signal will also be decayed less which can be beneficial imaging tissue with short T_2 or T_2^* constants. Another crucial benefit can be reduced artefacts. As noted earlier, susceptibility artefacts are accumulated during the readout. Therefore, using accelerated measurements can lead to less artefacts.

On the downside following eq. 2.24 the SNR is reduced by $\frac{1}{\sqrt{R}}$. Also the increasing g, calculated with eq. 2.23, describes through the occurring noise amplification an algorithmic limit for the separation of superimposed pixels.

3.2.4 Field Inhomogeneities

There are multiple effects that can lead to field inhomogeneity effects. First of all susceptibility effects in the patients can induce the so called susceptibility gradients. The magnetic susceptibility

odd echo   *even echo*   sampling omitted
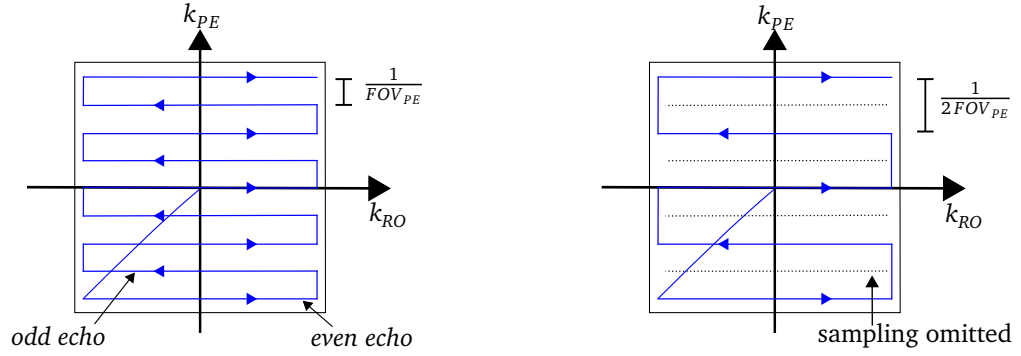
Figure 3.4: Scheme of a fully sampled and accelerated EPI trajectory.
Scheme of a fully sampled cartesian EPI trajectory on the left, which corresponds to a reduction factor of R=1. On the right Δk_{PE} is doubled and consequently the FOV halved, respectively R = 2. Such an accelerated measurement approximately halves the imaging time, but leads to aliasing. The aliasing can be unfolded using PI image reconstruction techniques.

quantifies how susceptible a magnetic material is to the magnetic field and is denoted by χ. For linear materials χ is the constant of proportionality between $\mathbf{M}$ and $\mathbf{H}$ and consequently $\mathbf{M} = \chi \mathbf{H}$. As usual the susceptibility generalises to a tensor representation for non-linear cases.

Recalling the fact that $\mathbf{B} = \mu \mathbf{H}$ it is possible to derive $\chi = \mu_r - 1$. From this eq. it becomes clear the χ is a dimensionless quantity. Furthermore, we formulate

$$\mathbf{B} = \mu_0 \left(\mathbf{H} + \mathbf{M} \right) = \mu_0 \mathbf{H} \left(1 + \chi \right). \tag{3.6}$$

As already mentioned in sec. 2.2.2, the signal density is $v(x, y) = \int_{z_o - \Delta z/2}^{z_o + \Delta z/2} M^o(x, y, z) \, dz$. Therefore, using eq. 3.6, we can relate $\mathbf{B}$ to the recorded signal described in eq. 2.8. This depiction is useful to analyse the recorded signals in the vicinity of interfaces. Such an interface is depicted in fig. 3.5. In the human brain this concept has a particular importance at water air interfaces which are for instance located at the borders of sinus cavities.
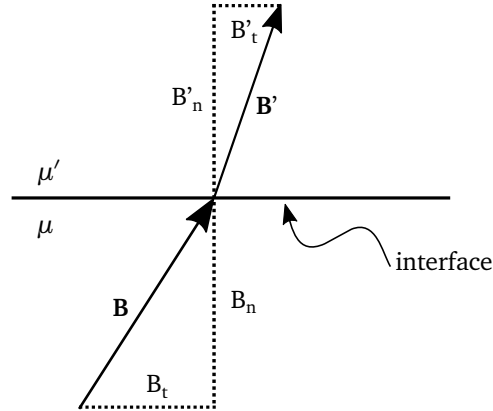
Figure 3.5: Flux density boundary condition.
Note that the normal component of B is continuous across the interface, while the tangential component is discontinuous. A practical example for EPI measurements are interfaces at the borders of the sinus cavities.

The boundary conditions for such an interface are

$$\begin{aligned} \mathbf{B}_n - \mathbf{B}'_n &= 0 \\ \mathbf{H}_t - \mathbf{H}'_t &= \bar{\mathbf{J}}. \end{aligned} \tag{3.7}$$

Most tissue in the body consists of water. The susceptibility difference between tissue and air can see local frequency shifts in the order of several ppm [16]. As the precession frequency is determined by the local field, these interfaces can induce additional susceptibility gradients. These gradients prevent correct spatial encoding, as described in 2.2.3, potentially leading to gross image distortion.

Another crucial source for field inhomogeneities is the so called *water-fat shift*. The shift between water and fat is $\approx$ 3.5ppm. On a 1.5T scanner the Larmor frequency is $\omega_0 \approx$ 64Mhz. Consequently, the difference in resonance frequency is around 220Hz. Therefore, proper fat suppression gains importance with increasing main field strengths.

3.2.5 Nyquist Ghosts

Nyquist ghosts are one of the most prominent artefacts occurring during EPI acquisitions. An EPI trajectory is shown in fig. 3.4. To perform an image reconstruction the echoes sampled in an *odd* manner have to be reversed. This is necessary because the spatial frequencies are sampled in an opposed order for *odd* compared to *even* lines.

Only when *even* and *odd* echoes are perfectly mirror-reversed the *odd* echo flip can be performed without introducing errors in the image reconstruction. In reality the rapid switching of the gradients needed to obtain an EPI image, induce eddy currents in coils and all conducting surfaces. These eddy currents yield a $EMF = -\frac{\partial \phi}{\partial t}$. Following *Lenz's law* the fields created by these currents always oppose the applied gradient fields. Therefore, the effective gradient is reduced and as a result the timing is delayed.

Assuming a local background gradient G' resulting from eddy currents, the measured qth echo will exhibit a shift of

$$\Delta k_{\text{shift},q} = (-1)^q \, \gamma \, G' \, T_{Eq} . \tag{3.8}$$

Because the polarity of *odd* and *even* echoes is opposite they will exhibit k-space shifts of opposite sign. Following the Fourier shift theorem, the 1D-FFT of that echo will see a linear phase variation

$$\hat{v}(x) = v(x) \, e^{-j2\pi\Delta k_{\text{shift},q}x} . \tag{3.9}$$

This linear phase variation is shown in fig. 3.6b). This asymmetry leads to aliasing in the spatial domain which results in a ghost shifted half a FOV respectively $\frac{N}{2}$ pixels away. Nyquist Ghosts are often also called *N/2 Ghosts*. Fig. 3.6c) shows an example of such Nyquist ghosting obtained by simulation.
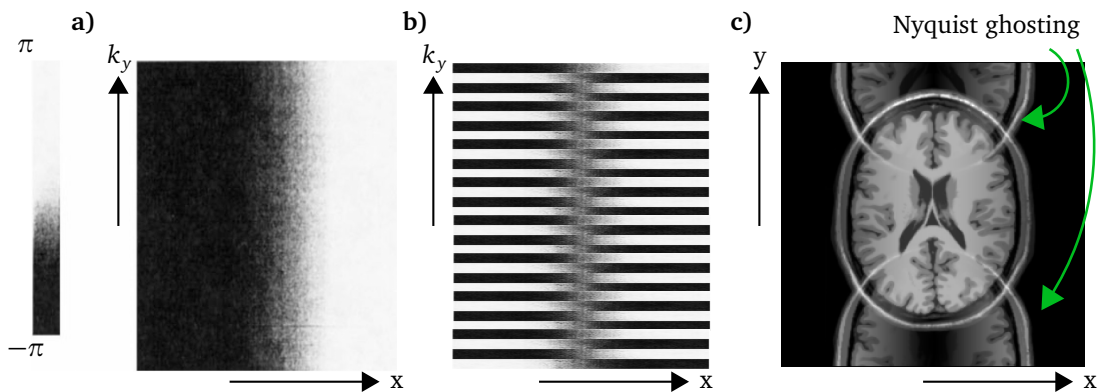
Figure 3.6: Phase rolls for EPI echoes and resulting Nyquist ghosting
a):Phase roll for a spin warp data set will not cause ghosting artefacts. **b)**:Phase roll for echoes of an EPI data set acquired in opposite k_x directions, after FFT in RO direction. These discontinuities are the principal cause of ghosting artefacts in EPI. .
b): Simulated Nyquist Ghost obtained by misaligning all *odd* echoes by one Δk_x.

To emphasise the Nyquist ghost problem, it can be stated that for BOLD MRI a N/2 ghost would imply that the brain activity is projected into a region half a FOV away [17].

Furthermore, it also has to be noted that all filters have non-zero phase responses which result in k-space misregistration and phase errors [18] [2].

3.3 Model Based and Iterative Image Reconstruction

When looking at the reconstruction problem of MRI, it becomes clear that the reconstruction procedure can be formulated as an inverse problem. The measured data $\mathbf{m}$ can be formulated as

$$\mathbf{m} = \mathbf{A}\mathbf{v}, \tag{3.10}$$

in relation to the reconstructed image $\mathbf{v}$ via the system matrix $\mathbf{A}$. In this simplest model-based formulation of eq. 3.10 the system matrix $\mathbf{A}$ denotes the Fourier encoding $\mathbf{A} = e^{j\mathbf{k}\mathbf{r}}$. This underlines why the Inverse fast Fourier transform (IFFT) has been used as the standard tool for reconstructing images obtained under conventional full cartesian spin-warp imaging.

There are multiple benefits stemming from this model-based formulation of the EPI reconstruction. First of all, it is possible to integrate effects like phase errors, field inhomogeneity effects and non-uniform or non-cartesian sampling patterns directly into the reconstruction. Second of all, prior information can be used to enforce smoothness and also support constraints, like e.g. phase constraints. On the downside it has to be noted, that an extension of the signal model complicates the reconstruction procedure [19].

The following sec. 3.3.1 gives an overview of the formulation and assumption used for $\mathbf{A}$. In sec. 3.3.2 an iterative algorithm for the solution of eq. 3.10 is described.

3.3.1 Model-Based Formulation of Reconstruction

While the measurement m is discrete, the reconstructed signal densities $v(\mathbf{r})$ are unknown continuos-space functions. Therefore, object functions have to be used to enable estimation v for this ill-posed problem. A widely used object function is a *rect* function. This mathematical choice can be visualised by assuming square voxels. Therefore, the signal densities v can be approximated using

$$v(\mathbf{r}) = \sum_{j=1}^{N} v_j \, \text{rect}(\frac{\mathbf{r} - \mathbf{r}_j}{FOV}), \tag{3.11}$$

where N denotes the number of voxels. We can obtain a simplified discrete model per coil ξ

$$s_\xi(t_j) = \sum_{j=1}^{N} a_{\xi ij} \, v_j. \tag{3.12}$$

As outlined in sec. 2.3.1 and 2.3.2 using SENSE the coil sensitivity profiles are integrated into the encoding function $\mathbf{E}$. Therefore, $a_{\xi ij}$ in eq. 3.12 are the elements of our system matrix $\mathbf{A}$. As an example for the extension of the signal model, the field inhomogeneity effects are taken into account as well. Therefore, the system matrix elements can be written as

$$a_{\xi ij} = \int \text{rect}(\frac{\mathbf{r} - \mathbf{r}_j}{FOV}) \, c(\mathbf{r}) \, e^{-j\mathbf{k}(t)\mathbf{r}} e^{-j\Delta\omega_{B0} t} d\mathbf{r} \approx c(\mathbf{r}_j) \, e^{-j\mathbf{k}(t)\mathbf{r}_j} e^{-j\Delta\omega_{B0} t}. \tag{3.13}$$

Using the system matrix elements $a_{\xi ij}$ in eq. 3.13 leads to the matrix formulation of eq. 3.10, $\mathbf{m} = \mathbf{A}\,\mathbf{v}$. Also further effects like binary sampling masks M_s and phase maps can be integrated into the system matrix, see sec. 4.5.2.

3.3.2 Iterative Methods

In a usual setup image dimensions are in the range of matrices of 256×256 pixels and more than 10 receive coils are used. Therefore, the system matrix can contain more than a million elements. It is clear that is costly to invert such a system analytically, as the complexity is of order $\mathcal{O}(N^3)$. Furthermore, the system can be ill-conditioned. Inverting such a ill-conditioned system, numerical errors are introduced into the solution.

Furthermore, using PI methods the inverse problem is also overdetermined due to multiple receive channels. Therefore, a prominent tool to solve these large systems are iterative algorithms.

Instead of looking for an exact solution of 3.10 in the iterative method the difference between left and right side is minimised [20]. This difference is specified using the so-called *residual vector* $\mathbf{r} = \mathbf{Av} - \mathbf{m}$. Therefore, the iterative algorithm should minimize a norm of this residual vector. The so called *cost functional* is defined by

$$J(\mathbf{v}) = ||\mathbf{Av} - \mathbf{m}||^2. \tag{3.14}$$

Consequently a solution $\hat{\mathbf{v}}$ can be found by minimising

$$\hat{\mathbf{v}} = \arg\min_{\mathbf{v}} J(\mathbf{v}). \tag{3.15}$$

As this is another formulation for a minimisation of the sum of $|\mathbf{r}|^2$, the minimisation problem ist often referred to as a *least-squares problem*.

The condition number cond($\mathbf{A}$) can be stated as the ratio of the largest to the smallest singular value cond($\mathbf{A}$) $= \frac{max\sigma_0(\mathbf{A})}{min\sigma_0(\mathbf{A})}$ [21]. Having a high condition number corresponds to an ill-conditioned system. One of the main issues with ill-conditioned systems is that small errors in the input data will result in large errors in the output data. For example noisy MRI signals could result in large errors in the reconstructed image.

One option to deal with an ill-conditioned system is to discard a fraction of the smallest singular values, which is called the Truncated SVD or TSVD [21]. In the case of SENSE this algorithm is not really fitting as the number of singular values is already very small [13]. Other methods include the Newton's method, the Steepest Decent Method or CG methods. See sec. 4.3 for explanations on the iterative algorithm implemented in this work.

One possible solution to deal with ill-conditioning due to noise or artefacts are regularisation methods. A regularisation can stabilise the solution for high iteration counts and also includes the possibility to include prior information [22]. We therefore extend the previous equation to

$$\hat{\mathbf{v}} = \arg\min_{\mathbf{v}} ||\mathbf{Av} - \mathbf{m}||^2 + \lambda\beta(\mathbf{v}). \tag{3.16}$$

An example for a regularisation method is the widely used *Tikhonov* regularisation. The chosen regulariser $\beta(\mathbf{v}) = ||\mathbf{v}||^2$ adds the λ weighted 2-norm of the solution vector to the minimisation problem. It is also possible to include prior knowledge respectively a reference image $\bar{\mathbf{v}}$ to the regulariser, $\beta(\mathbf{v}) = ||\mathbf{v} - \bar{\mathbf{v}}||^2$ [22]. See e.g. [22] for other possible regularisers. . The regularisation parameter λ can be determined using the *L-curve method*, see [20] for further details.

4 | Methodology

4.1 System Setup

All Philips scanners have an on board reconstruction unit, which is composed in modules. First the radiologist or researcher picks desired options in the user interface, like for example T_E or the desired imaging sequence. When the examination of the scanner starts, first the SENSE reference scan is taken. It consists of two parts: Initially the sensitivity of the RF body coil is measured. The second part consists of measuring the sensitivities of the channels in the head coil array. The processing of the SENSE reference scan data is explained in sec. 4.2.2. After the initial reference scans are executed, the MRI scanner performs the EPI reference scan to yield information about phase errors, see sec. 4.5.1. While the sequence shown in fig. 3.2 is performed, the reconstruction unit assembles the modules for the *reconstruction pipeline*. This pipeline is referred to as *recon2*. After a slice measurement has been performed, the data is passed through the *recon2* pipeline leading to a final image. Using a *Philips Research* internal format, the reconstructed image can be exported and loaded into a *Python* environment described in sec. 4.1.3. After any *recon2* module a data export can be triggered. The exported data used in this work is listed under table B.1.

4.1.1 MRI System

The measurements were obtained on a *Philips Ingenia* 1.5T [23] and a *Philips Ingenia* 3.0T [23] scanner (Koninklijke Philips N.V.). The detailed measurements obtained on each scanner are listed under table A.1. Both scanners have an open bore diameter of 70cm and a maximum FOV of 55cm. The gradients have an maximum amplitude of 45mT/m and a maximum slew rate for each axis of 200 T/m/s. All scans were conducted with digital *dStream* head coils. The surface coil array uses a maximum of 15 channels achieving a maximum coverage of 30cm [24].

Several advantages and disadvantages for the usage of a high-field MRI should be noted. As stated earlier the SNR increases approximately proportional to $\mathbf{B}_0$ and consequently it is favourable to use a higher $\mathbf{B}_0$ field system. Furthermore, T_1 increases with $\mathbf{B}_0$. This can be favourable in producing T_1 weighted images.

On the downside, off-resonance effects like susceptibility variations, see sec. 3.2.4, and water-fat shift increase with $\mathbf{B}_0$. The main spectral peak of fat and water differ by 3.5ppm of $\mathbf{B}_0$. For a scanner with $\mathbf{B}_0$=1.5T the frequency variation can be calculated as $\Delta f = \gamma \, \mathbf{B}_0 \, 3.5\text{ppm} \approx 64\text{MHz } 3.5\text{ppm} \approx 220\text{Hz}$. For a 3.0T system Δf would be approximately doubled to 440Hz. Therefore, the 3.0T system are predestined to be used to study effects of field inhomogeneity on the reconstruction algorithm. Furthermore, the RF wavelength can be reduced many times over, since the field length is inversely proportional to $\mathbf{B}_0$. For even higher field strengths like commercially available 7T scanners, standing waves in the FOV can become visible [25]. The Specific Absorption Rate (SAR) describes the RF power deposited in the imaged human tissue. Relating safety concerns due to patient heating it is strongly regulated, and is not allowed to increase 3.2 $\frac{\text{W}}{\text{kg}}$ in the head [26].

Unless stated otherwise in table A.1 all phantom measurements were conducted with a 3.5l bottle filled with salt water solution. As stated in the same table also other phantoms were used, which show more susceptibility artefacts. In vivo scans were performed following the *Philips Research* internal regulations.

4.1.2 Measurements

All measurements executed and used for this work are listed under table A.1. These can be structured into multiple groups:

The first group consists of all phantom measurements with the 3.5l salt-water solution filled phantom. As this phantom has few field inhomogeneity effects and is smooth inside it is suitable to study the limits of the off-line reconstruction algorithm. The second group consists of phantoms which show more susceptibility artefacts and also have sharp edges.

Third of all strong field inhomogeneity effects were simulated using ω_0 offsets and spatially linearly varying gradient offsets.

Also multiple in vivo measurements were obtained. These tend to have the highest demand on the reconstruction algorithm, as the obtained data is noisier than in phantom cases.

A multislice study was conducted to study the reusability of the calculated phase map for adjacent slices.

Fig. 4.1a) shows an example of the loaded raw data in k-domain. As expected the majority of the signal can be found in the around the zero frequency. Fig. 4.1b) shows the corresponding 2D-FFT of the data. Note that fig. 4.1a) respectively fig. 4.1b) represent only one out of up to 15 receive channels. The result of the offline reconstruction is shown in fig. 4.1c).
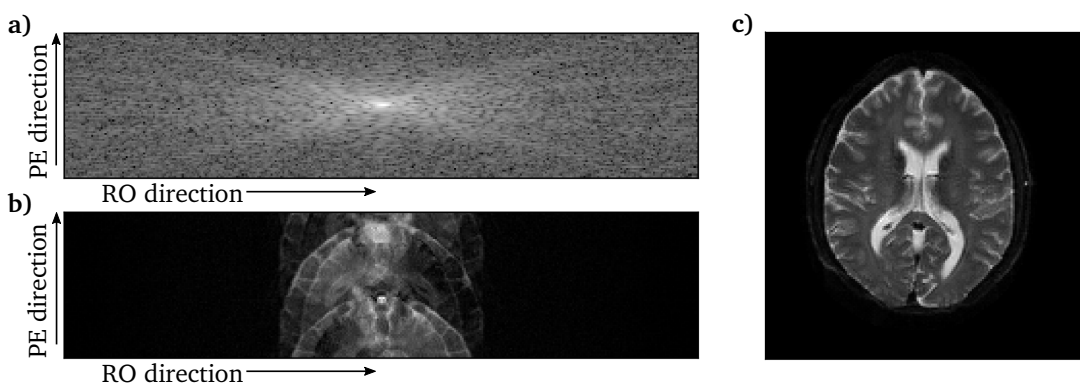
Figure 4.1: Input Data in k and spatial domain. Offline Reconstruction.
a): Shows input data of a single channel (logarithm of magnitude). Data collected using SE sequence with R=2 and fat suppression. PE denotes the *phase-encode* and RO the *readout* direction.
b): 2D-FFT of **a)** Note that due to oversampling in readout direction and non-uniform slope sampling the dimensions of the input data and the final reconstruction vary significantly.
c): Offline reconstruction calculated using the algorithm described in this work.

4.1.3 Software Framework

The offline reconstruction was implemented in *Python 3.6*. Based on the *Anaconda* environment *Spyder 3.1.4* was used as an editor. All algorithms were implemented using *numpy* [27]. The following table B.1 shows the data and parameters used in for this work. Table B.2 describes the implemented *Python* functions.

4.2 Preparation of EPI Data

Before the actual iterative image reconstruction can be executed, preprocessing steps need to applied. These include interpolation steps as explained in the next section as well as preconditioning, see sec. 4.2.2, which can reduce the number of iterations.

4.2.1   Interpolation of Matrices

The zero-fill factor in one cartesian coordinate i can be described as

$$Z_{f,i} = \frac{\text{rows/columns in final } k\text{-space matrix}}{\text{rows/columns in acquired } k\text{-space matrix}} \, . \tag{4.1}$$

There are multiple reasons why a zero interpolation is useful. The number of rows correspond to the number of PE encoding steps. This number is also called the EPI factor. For an EPI acquisition it is always an odd number. In RO direction the number of sampling points is always even to achieve an even signal distribution between $-k_{x,max}$ and $k_{x,max}$. Therefore, to achieve a square matrix for the multiplications of sec. 4.3 the matrix needs to be filled with at least one row full of zeros. By convention this lower row is filled in the lower half plane.

As for $R \neq 1$ the raw data only contains the actually sampled echoes, the omitted readout lines need to be zero filled. Thus, the acquired data matches the coil sensitivity matrices, sec. 4.2.2. The area ration of zero-filling in relation to total area was chosen to be $\sim 15\%$ in this work.

4.2.2   Calculation and Processing of Sensitivity Profiles

Due to the fact that unfolding is achieved by using spatial receive coil sensitivities, the knowledge of those is a prerequisite to obtain a valid reconstruction. Spatial sensitivities are complex functions that vary smoothly [8]. To obtain the coil sensitivity profiles a SENSE reference shot is taken. As mentioned these reference shots measure the RF body coil sensitivity and the sensitivities of the surface head coils.

As noted in table B.1 the body coil sensitivity as well as the sensitivities from the surface coils were loaded into the *Python* environment. As the surface coil sensitivity profiles from the SENSE reference shot still contain anatomical information, every surface coil sensitivity profile $\xi = 1, ..., n_c$ is divided by the body coil, following

$$c_\xi(\mathbf{r}) = \frac{c_\xi(\mathbf{r})}{c_{\text{bodycoil}}(\mathbf{r})} \, . \tag{4.2}$$

The division of the surface coils sensitivities by the body coil is already performed in the *recon2* reconstruction unit and thus it has not to be performed in the *Python* environment.

Fig. 4.2a) shows a body coil sensitivity profile. Using this profile the *Object indicator map* Ω is calculated. Pixels with a magnitude smaller than 20% of the maximum magnitude of the body coil sensitivity are marked as zero, see fig. 4.2b). In terms of SNR such a thresholding is favourable, as the SNR increases with reduced aliasing. Furthermore, the number of superimposed pixels is also reduced.

A surface coil sensitivity profile is shown in fig. 4.2c). For the calculation first the shown surface coil sensitivity is thresholded with Ω. Following it is divided by the square root of the sum. This intensity correction follows

$$I_{\rho,\rho} = \frac{1}{\sqrt{\sum_\xi^{n_c} |c(\mathbf{r}_\rho)|^2}} \, , \tag{4.3}$$

and reduces the number of iterations needed to solve an iterative algorithm [9].

4.2.3   Readout Resampling

In the development of EPI the rapidly vanishing signal amplitude, modulated by T_2 respectively T_2^*, has always been a challenge since it limits the possible *Echo train length*. Depending on the technique used the time window to record the signal $s(t)$ is usually between 30ms and 200ms. Sec. 2.2.2 introduced the spatial encoding by gradients, which enables image reconstruction using FFTs. For EPI the readout gradient G_{RO} can be modelled as a trapezoidal, see the red dotted line in fig. 4.3a). Therefore, the gradient can be described by a rise time, slew rate and gradient amplitude. Usual values for the used gradient system in this work are given in sec. 4.1.1. Sampling only on the constant gradient amplitude shown in light orange in fig. 4.3a) the k-space trajectory will traverse
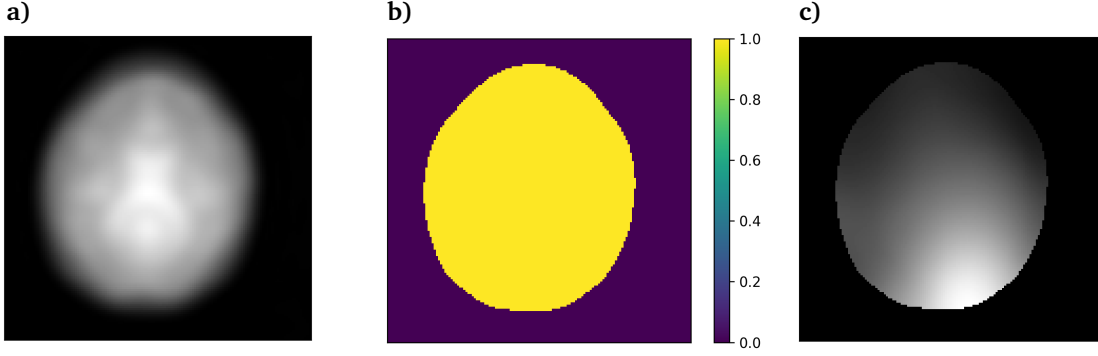
Figure 4.2: Body coil reference, *Object indicator map* Ω and Surface coil sensitivity profile.
a) Shows the body coil image obtained from the low resolution SENSE reference shot. The *Object indicator map* Ω as shown in **b)** is obtained by excluding pixels that are smaller than 20% of the maximum magnitude of the body coil sensitivity. **c)** shows the sensitivity profile of a single surface coil obtained by first dividing by the body coil sensitivity, following eq. 4.2. Following the sensitivity profile is masked with Ω and intensity corrected following eq. 4.3.

the *k*-space with a constant *k*-space velocity. For EPI it is beneficial to also sample on the slopes of G_{RO}, since this improves the sampling efficiency. The fraction of the gradient slope used for sampling is referred to as *slope*-fraction and shown in light purple in fig. 4.3a). Following $k_{RO}(t) = \gamma \int_0^t G_{RO}(\tau)\, d\tau$ it is clear that a non-constant G_{RO} results in a non-uniform *k*-space trajectory, as shown in 4.3a) in green.
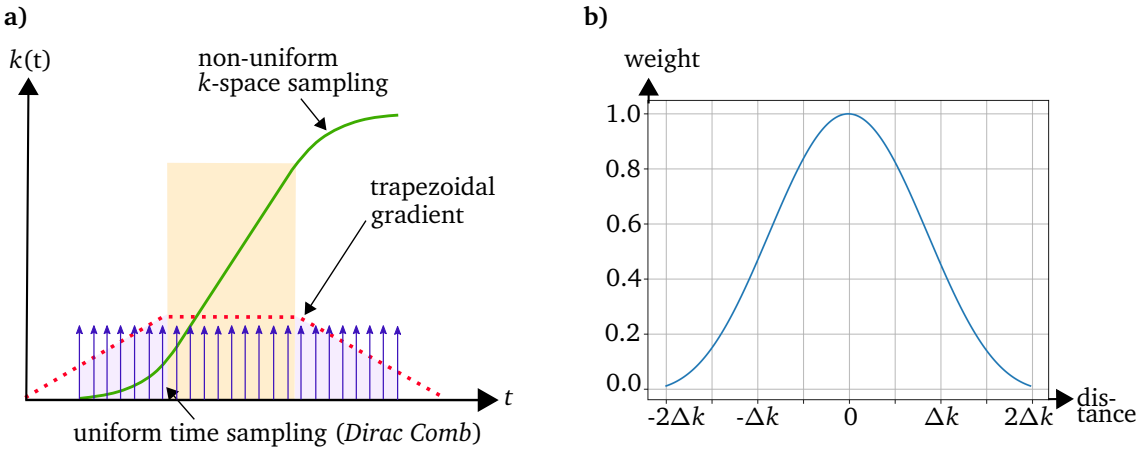
Figure 4.3: Non-uniform *k*-space sampling and *Kaiser-Bessel* window used for regridding.
a) shows a trapezoidal readout gradient G_{RO} used. The areas in purple are sampled and are referred to as *slope fraction*. Slope sampling results in a non-uniform *k*-space sampling. The areas coloured in bright orange are sampled uniformly. The spikes denote the III function, used to describe a *Dirac Comb*.
b) shows a *Kaiser-Bessel* window of width $4\Delta k$, used to regrid the non-uniform *k*-space trajectory.

Taking this into consideration, the sampled data $\mathbf{m}_s$ can be described as

$$\mathbf{m}_s = \mathbf{m}\, O\,. \tag{4.4}$$

O is a sampling function

$$O(k_x, k_y) = \sum_{j=1}^{P} {}^2\delta(k_x - k_{x,j}, k_y - k_{y,j})\,, \tag{4.5}$$

which samples in PE direction and RO direction. Therefore, O consists of *P* two-dimensional delta functions representing the sampling grid [28]. Only the sampling pattern in RO direction is considered to be non-uniform. The sampling pattern in PE direction is always uniform, but might exhibit

an acceleration factor R - see fig. 3.4.

It should be noted that the term Non-Uniform sampling (NUS) is also referred to non-uniform sampling patterns in time. This can be used in order to receive a uniform sampling density of k-space [11]. Using $\Delta k_x = \gamma \int_{t_{s-1}}^{t_s} G_x(\tau)$ it is clear that by picking non-uniform sampling times (t_{s-1}, t_s), Δk_x can be constant. However, the noise statistics are distorted, making other adaptions necessary. In this work only the first approach of non-uniformity in k-space sampling density is considered.

To yield $\mathbf{m}$ from $\mathbf{m}_s$ the influence of the non-uniform sampling introduced by O needs to be considered. While the collected k-space data is 2-dimensional the following explanations are made for the readout direction, in which the non-uniform sampling occurs. Without any loss of generality $k_x = k_{PE}$. Consequently, in PE direction no regridding is necessary.

Methods to consider this sampling and consequently to reconstruct non-cartesian data can be categorised in three approaches [29]: *grid driven* interpolation methods try to estimate grid points by interpolating adjacent k-space data. Furthermore, methods exist which try to locally approximated optimum interpolators for a specific location.

The method used in this work and in most of today's reconstruction algorithms is a *data driven* approach, which adds data points to adjacent grid points. Therefore, the data is resampled to a cartesian grid. The contribution of data to grid points is determined by fitting kernels. An example of such a kernel is shown in fig. 4.3b). While this is very favourable in terms of SNR, it complicates the calculation as e.g. a density compensation needs to be implemented, see the explanations below.

The first basic idea of a gridding algorithm is to divide the k-space plane into a uniformly spaced grid, denoted by $Ш(k_x)$. Therefore, $Ш(k_x)$ defines a sum of equally spaced two-dimensional delta functions. Then, for every gridpoint, all data points falling to a region of it, are summed [28].

The gridding operation is not an exact interpolation. Rather the gridding operation approximates the gridded function within some region. However, this is an accurate representation as long as the width of a region is smaller or equal than distance between two cartesian grid points [30].

Optimally this gridding procedure would use a *sinc* convolution function, which is not feasible due to its infinite nature. The choice for the convolution function is made following two conflicting arguments: computational complexity and performance of the function. In [28] it is shown how different functions compare and that the *Kaiser-Bessel* is a good compromise between computational complexity and accuracy.

The *Kaiser-Bessel* window $W_{KB}(k_x)$ implemented for this work, follows

$$W_{KB}(k_x) = \frac{1}{\alpha} I_0 \Big[\beta \sqrt{1 - (\frac{2k_x}{\alpha})^2} \Big]. \tag{4.6}$$

A graphical representation of this function is shown in fig. 4.3b). In eq. 4.6 I_0 denotes the modified Bessel function of the first kind, order 0. The width α is chosen as $\alpha = 4\Delta k_x$ and the design parameter β as $\beta = \frac{\pi\alpha}{2}$. The value β can be found by minimising a functional which describes the amount of aliasing at the edges of the FOV [28].

The convolution and resampling to a uniform grid than follows

$$m_{SCS}(k_x) = [m_S(k_x) \star W_{KB}(k_x)] \, Ш(k_x). \tag{4.7}$$

As the sampling density is not uniform across the k-space plane, a density compensation function $\rho_A(k_x)$ needs to be introduced and applied, $\rho_A(k_x) = O(k_x) \star W_{KB}(k_x)$. Oversampled k-space areas consequently have a larger area density vice versa undersampled areas will have a smaller one. $\rho_A(k_x)$ is either applied as part of a *postcompensation* or *precompensation*. When applying it in a *postcompensation* fashion, to rapidly changing densities can't be taken care of [29]. Therefore, density compensation was applied prior to the convolution and the gridding algorithm reads as

$$m_{SCS}(k_x) = \left[\frac{m_S(k_x)}{\rho_A(k_x)} \star W_{KB}(k_x) \right] Ш(k_x). \tag{4.8}$$

As a last step after applying the *convolution gridding algorithm*, the resulting complex image (Fourier transformed to spatial domain) has to be divided by the Fourier transform of the convolution kernel $W_{KB}(k_x)$. This division is also referred to as deapodization.

The Fourier transform of eq. 4.6 is the impulse response $W_{KB}(x)$ given by

$$W_{KB}(x) = \text{sinc}(\sqrt{(\pi \alpha x)^2 - \beta^2}). \tag{4.9}$$

A rolloff effect due $W_{KB}(x)$ will show up as an attenuation towards the sides of the image. To account for this the data is collected using an oversampling factor of 2.0, which leads to good sidelobe suppression. This explains why the number of points in readout direction N_{RO} in fig. 4.4a) is significantly larger than in fig. 4.4b). Without oversampling replica sidelobes will superimpose with the image at the edge of the FOV. By introducing an oversampling a transition band can be introduced, aliasing and apodization can be reduced. A oversampling can be conceived by sampling the k-space data in a denser way than the actual grid.

Fig. 4.4 shows the result of applying the *convolution gridding algorithm* explained above.

a)   **b)**
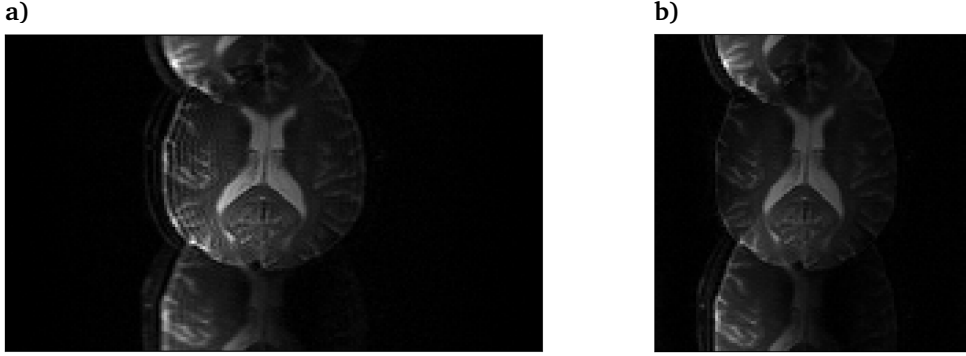
Figure 4.4: Readout regridding: Raw data and resulting coil image.
a) shows a coil image obtained by taking the k-space data of a single surface coil, flipping all odd echoes and then executing a 2D-FFT. Note that the data was collected using an oversampling factor of 2.0 and 80% of the gradient slopes were used for sampling. **b)** shows the same coil data, after readout regridding has been performed as described in this section.

4.3 Implementation of Iterative Image Reconstruction

As noted for SENSE accelerated measurements, the encoding matrix $\mathbf{E}$ can be stated as

$$\mathbf{E}_{(\xi,\kappa),\rho} = e^{j\mathbf{k}_\kappa \mathbf{r}_\rho} \, c(\mathbf{r}_\rho), \tag{4.10}$$

where ρ is the voxel index, κ represents the sampling position in k-space and $\xi = 0,...,n_c$ is the coilindex. Using the encoding matrix the so called *forward model* the measurement can be formulated as

$$\mathbf{m} = \mathbf{E}\mathbf{v}. \tag{4.11}$$

Using this equation the goal is to estimate the signal density v in every voxel located at spatial position $\mathbf{r}$ and are stacked in the vector $\mathbf{v}$. Therefore, for a square image the dimension of $\mathbf{E}$ is $n_c n_d \times N$. The vectors $\mathbf{v}$ and $\mathbf{m}$ have a length of N^2 respectively $n_c \, n_d$.

It is clear that to find a direct calculation of $\mathbf{v}$, a matrix inversion of $\mathbf{E}$ would be needed. Due to very large dimension of $\mathbf{E}$ this is not really feasible, as $\mathbf{E}$ might also ill-conditioned or even singular.

To find a decoding matrix $\mathbf{F}$ there are two main approaches: For the first approach the goal is to optimise the voxel shape, this is termed as *strong* reconstruction. A common assumption for an optimal voxel shape are e.g. box functions.

The second second aims for optimal SNR, weakening the optimal voxel shape condition, termed *weak* reconstruction. This can be achieved by requiring an orthogonality between $\mathbf{F}$ and $\mathbf{E}$. Therefore, the *weak* voxel condition is defined with the identity matrix $\mathscr{I}$ as

$$\mathbf{F}\mathbf{E} = \mathscr{I}. \tag{4.12}$$

If eq. 4.12 is underdetermined, the remaining degrees of freedom can be used for SNR optimisation [9].

Assuming τ independent Gaussian noise sources, each distributed with $\mathscr{N}(0, \sigma_\tau^2)$. Per receive

channel ξ, the τ noise sources are individually weighted by a complex factor $\omega_{\xi,\tau}$. The $n_c \times n_c$ receiver noise matrix Ψ is then defined as

$$\Psi = \sum_{\tau} \sigma_{\tau}^2 \, \omega_{\xi,\tau} \, \omega_{\xi,\tau}^* . \tag{4.13}$$

Ψ depends on the coil geometry, coil sensitivities and load. Thus, it should be determined in the actual imaging setup. Ψ can be determined by analysing samples, consisting only of noise, before the actual imaging procedure. A sufficiently large number of samples, usually at least 10^3 is time averaged to calculate Ψ. To refer Ψ to all n_d k-space sampling positions $\tilde{\Psi}$ is calculated by $\tilde{\Psi} = \Psi \otimes \mathscr{I}_{n_d}$. $\mathscr{I}_{n_d}$ is the identity matrix of size $n_d \times n_d$.

Thus, the noise in the image is given as the ρth diagonal entry of $\mathbf{F} \, \tilde{\Psi} \, \mathbf{F}^H$. This matrix product, termed the *image noise matrix*, should be minimised to achieve optimal SNR. Accordingly, the minimisation problem reads as

$$\begin{aligned} \underset{\mathbf{F}}{\text{minimize}} \quad & \mathbf{F} \, \tilde{\Psi} \, \mathbf{F}^H \\ \text{subject to} \quad & \mathbf{FE} = \mathscr{I} . \end{aligned} \tag{4.14}$$

Using the Lagrange function $\mathscr{L}_{\rho}$ with Lagrange multiplicators $\Lambda_{\rho,\rho'}$ is used find the solution to the minimisation problem eq. 4.14. Thus, the Lagrangian is defined as

$$\mathscr{L}_{\rho} = (\mathbf{F} \, \tilde{\Psi} \, \mathbf{F}^H)_{\rho,\rho} + \sum_{\rho'} \Lambda_{\rho,\rho'} (\mathbf{FE} - \mathscr{I}_{\rho,\rho'}) . \tag{4.15}$$

Setting all partial derivates $\frac{\partial \Lambda_{\rho}}{\partial \mathbf{F}}$ to zero and considering all receive channels $\xi = 0, ..., n_c$ we obtain

$$\begin{aligned} 2 \sum_{\xi'} \mathbf{F}_{\rho,(\xi',\kappa)} \, \Psi_{\xi',\xi} + 2 \sum_{\rho'} \Lambda_{\rho,\rho'}^* \, \mathbf{E}_{(\xi,\kappa),\rho'} \quad & \forall \rho, \xi, \kappa \\ \sum_{\xi,\kappa} \mathbf{F}_{\rho,(\xi,\kappa)} \mathbf{E}_{(\xi,\kappa),\rho'} = \delta_{\rho,\rho'} \quad & \forall \rho, \rho' . \end{aligned} \tag{4.16}$$

This can be restated in matrixform as

$$\begin{pmatrix} 2\tilde{\Psi} & \mathbf{E} \\ \mathbf{E}^H & \mathbf{0} \end{pmatrix} \begin{pmatrix} \mathbf{F}^H \\ \Lambda^H \end{pmatrix} = \begin{pmatrix} 0 \\ \mathscr{I} \end{pmatrix} . \tag{4.17}$$

Inversion and left multiplication leads to the solution of the *weak* reconstruction, which defines the SNR optimal decoding $\mathbf{F}$:

$$\mathbf{F} = (\mathbf{E}^H \, \tilde{\Psi} \, \mathbf{E})^{-1} \, \mathbf{E}^H \, \tilde{\Psi}^{-1} . \tag{4.18}$$

Equation 4.18 defines an estimate in the *least-squares* sense, which includes the prewhitening via $\tilde{\Psi}^{-1}$. Leaving $\tilde{\Psi}$ out is possible, but leads to the fact that noise assessment is skipped in the final estimate. Furthermore, it is possible to apply $\tilde{\Psi}$ to the coil sensitivity profiles and measured data, to achieve prewhitened, virtual channels [9]. Defining the Cholesky decomposition by $\Psi = LL^H$ leads to the decorrelation of eq. 4.19.

$$\begin{aligned} m_{\xi,\kappa}^{\text{decorr}} \quad &= \sum_{\xi'} (L^{-1})_{\xi,\xi'} \, m_{\xi',\kappa} \\ c_{\xi}^{\text{decorr}} \quad &= \sum_{\xi'} (L^{-1})_{\xi,\xi'} \, c_{\xi'}(\mathbf{r}) \\ \mathbf{E}_{(\xi,\kappa),\rho}^{\text{decorr}} \quad &= e^{j\mathbf{k}_{\kappa}\mathbf{r}_{\rho}} \, c_{\xi}^{\text{decorr}}(\mathbf{r}_{\rho}) . \end{aligned} \tag{4.19}$$

As eq. 4.19 is applied as a prewhitening step in the scanner reconstruction unit, the solution reduces to

$$\mathbf{v} = (\mathbf{E}^H \, \tilde{\Psi} \, \mathbf{E})^{-1} \, \mathbf{E}^H \, \tilde{\Psi}^{-1}\mathbf{m} = \Bigg|_{\substack{\mathbf{E}=\mathbf{E}^{\text{decorr}} \\ \mathbf{m}=\mathbf{m}^{\text{decorr}}}} (\mathbf{E}^H \, \mathbf{E})^{-1} \, \mathbf{E}^H\mathbf{m} . \tag{4.20}$$

As noted earlier an intensity correction I, defined in eq. 4.3, can be used as a preconditioner. Therefore, precondition can be seen as a scheme used to accelerate the calculation. Thus, it reduces the number of iteration steps to solve eq. 4.20 iteratively [21]. Therefore, eq. 4.20 is rearranged and left-multiplied with I^2 leading to

$$(I^2 \, \mathbf{E}^H \, \mathbf{E}) \, \mathbf{v} = I^2 \, \mathbf{E}^H \, \mathbf{m} \, . \tag{4.21}$$

However, to restore positive definiteness, needed to solve eq. 4.21 with a CG algorithm, I^{-1} is left-multiplied. Together with insertion of $\mathscr{I}$ in the form of $I \, I^{-1}$ this leads to the final eq. 4.22

$$(I \, \mathbf{E}^H \, \mathbf{E} \, I) \, (I^{-1} \, \mathbf{v}) = I \, \mathbf{E}^H \, \mathbf{m} \, . \tag{4.22}$$

The calculation of the algorithm eq. 4.22, via a CG method, is visually depicted in fig. 4.5. Using a CG algorithm the $N^2 \times N^2$ estimate is found in maximal N^2 iteration steps.
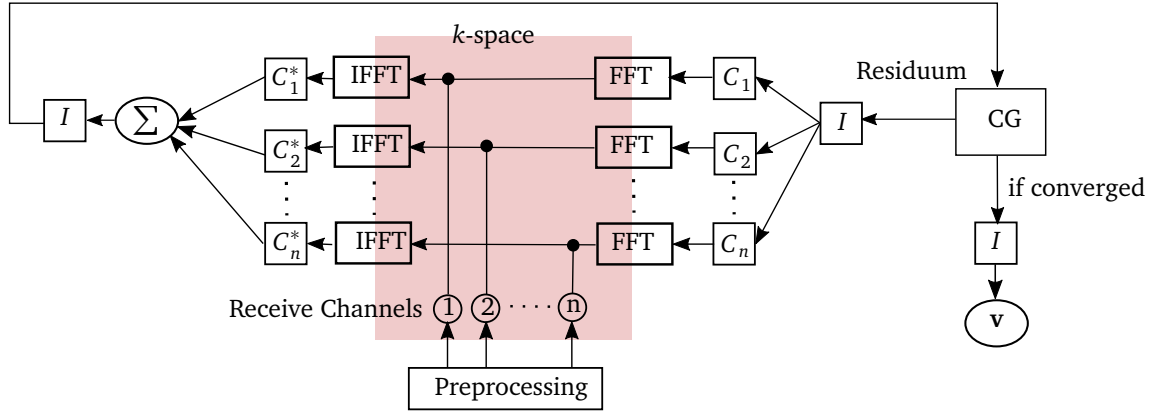
Figure 4.5: Schematic of iterative image reconstruction.
The depicted schematic follows the algorithm of eq. 4.22. The receive channels represented undersampled k-space data sitting on a cartesian grid. Adapted from [9].

4.4 Field Maps

In EPI spatial and intensity distortions due to inhomogeneous static magnetic fields play a crucial role. Some comments should illustrate why field inhomogeneity correction is of such importance. Fig. 3.4 introduced the typical cartesian k-space trajectories in the non-accelerated and accelerated case. Analysing fig. 3.4a) closely, reveals that any error made in the course of the readout are accrued throughout trajectory. Therefore, voxels lying at the end of the readout train are per se affected more by inhomogeneities. Furthermore, due to the low pixel bandwidth in phase encode direction, inhomogeneities have a stronger effect in PE direction. One of the most pronounced field inhomogeneity effects is produced near air-water interfaces, e.g. near to the sinus cavities in the brain. It is common to use EPI for imaging of the brain. Thus, these interfaces always have to be considered. In general, GRE sequences are affected more than SE sequences by field inhomogeneities. For GRE sequences no refocusing of the phase dispersion is used to achieve T_2^* contrast. Therefore, intrinsically GRE sequences are more sensitive to field inhomogeneities.

While there are shimming solutions available, not all inhomogeneities can be shimmed out. Even when a perfect shimming solution is available, the patient itself introduces field inhomogeneities. Therefore, the magnetic field inhomogeneity is a priori unknown [31] and an estimation of field inhomogeneities should always be implemented. As a core application of EPI is fMRI it can be stated that uncorrected field inhomogeneities can mislead activation near sinus cavities.

4.4.1 Field Map Estimation

As previously noted the recorded signal follows

$$s(t) = \int_{\mathcal{V}} v(\mathbf{r})\, e^{-j\Phi(\mathbf{r},t)} d\mathbf{r} \qquad \Phi(\mathbf{r},t) = \int_t \Delta\omega_{B0}(\mathbf{r}) + \gamma\, \mathbf{G}(t)\, dt \quad . \tag{4.23}$$

When field inhomogeneities are considered, the phase is not only determined by the applied gradients but also by field inhomogeneities. Thus, the field inhomogeneity has an influence of the position of a voxel in the final reconstruction [32]. Therefore, to account for field inhomogeneities, a method to measure those needs to be implemented. The de facto standard on todays scanners is based on two low angle Fast Low-Angle Shot (FLASH) [33] measurements, which are termed FFE on a *Philips* scanner. For this work the measurements were conducted using a flip angle of $\theta = 10°$.

Using two FLASH measurements with different echo time differing by ΔT_E the field inhomogeneity can be determined by

$$\Delta\omega_{B0}(\mathbf{r}) = \frac{\Delta\Phi(\mathbf{r})}{\Delta T_E} . \tag{4.24}$$

As noted the field inhomogeneity leads to a shift in the voxel position in EPI. To assess these shifts a so called Voxel shift map (VSM) is calculated. Because the proportionality constant between VSM and $\Delta\omega_{B0}$ is the bandwidth BW, eq. 4.25 results.

In general voxels can be shifted in PE and RO direction. Due to the very low bandwidth in PE direction only shift in PE direction are considered, as the shifts in RO direction are two orders of magnitude smaller and can be neglected [31]. Without any loss of generality the PE direction corresponds to the cartesian y axis in this work. Consequently, the VSM is determined by

$$VSM = \frac{\Delta\omega_{B0}}{BW_{PE}} . \tag{4.25}$$

A calculated VSM is shown in fig. 4.6b). In this measurement a linearly increasing field inhomogeneity was deliberately generated. Diving the obtained $\Delta\omega_{B0}$ map by the bandwidth yields the VSM.

4.4.2 Integration of Field Maps into Reconstruction Scheme

Reconsidering eq. 4.23 it becomes clear that the effects of field inhomogeneities are non-constant in the signal equation integral. Consequently, field inhomogeneity effects can't be directly accounted for in k-space. Therefore, the VSM has to be applied in spatial domain.

The voxels affected by voxel shifts are also termed *wrapped* voxels y^w. To calculate the *unwrapped* voxels y^{uw}, the voxel-shift quantified by the VSM has to be undone. Thus, *unwrapped* pixels can be calculated by

$$y^{uw} = y^w - VSM(y^{uw}) . \tag{4.26}$$

Because the VSM does not only contain integer values, interpolation or gridding algorithms have to be used for the calculation. To enable a successful SENSE reconstruction, it is crucial that the sensitivity maps match the collected data. Exhibiting field inhomogeneities in the subject, this assumption in general is not valid anymore. The sensitivity maps collected as a preparatory steps are only by a negligible extend exposed to pixel shifts induced by field inhomogeneities. To account for the $\Delta\omega_{B0}$ shift problem in EPI, there are two differing approaches. On the one hand, the collected coil images can be unwrapped. Such a coil image is shown in 4.6a). On the other hand, the sensitivity maps C can be wrapped to mimic the spatial distortion introduced by the field inhomogeneities. The resulting construction $\mathbf{v}$ has then to be unwrapped in a final step.

Two factors summarise why the wrapping of sensitivity maps is more favourable. First of all, the coil sensitivities can be assumed to be smooth functions [8], Thus, prior knowledge about the result of the wrapping is available.

Second of all, looking at fig. 4.5 it is clear that the wrapping has to be done for the forward and the unwrapping for the reverse part of the loop. Therefore, this procedure has to be repeated

twice per iteration. As mentioned wrapping the sensitivity and unwrapping the final image is always achieved in two calculations. Thus, the sensitivity wrapping approach has a numerical advantage by a factor proportional to the number of iterations needed to solve the CG loop.

Therefore, the implemented algorithm uses the VSM to calculate wrapped sensitivity profiles $\tilde{C}$. The result of such a wrapping is shown in 4.6d), being in accordance with the coil image 4.6a). Here it becomes also clear, that using the initial coil sensitivity profile $\tilde{C}$ for the reconstruction will result in significant reconstruction errors. This is due to the different shape of the coil image and $\tilde{C}$. The wrapped sensitivities $\tilde{C}$ are fed into the reconstruction algorithm of fig. 4.5, where a final reconstruction is calculated in the usual fashion, accounting also for Nyquist ghosts. This reconstruction $\tilde{\mathbf{v}}$ is then inversely interpolated to yield the final image $\mathbf{v}$.
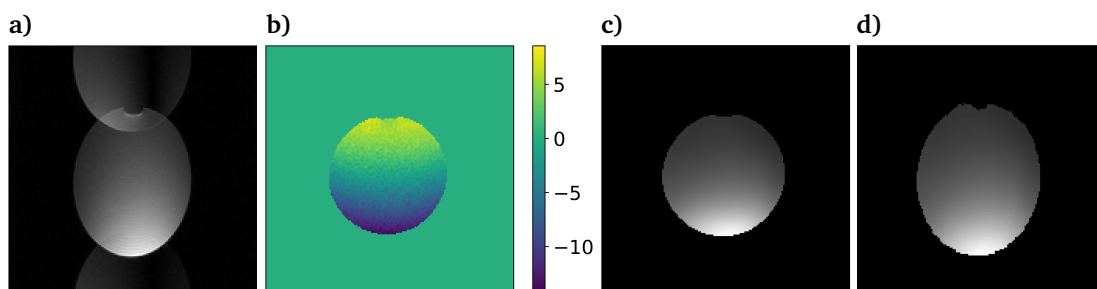
Figure 4.6: Integration of VSM into the reconstruction pipeline.
a) shows the coil image of a single surface coil, which is obtained by applying a 2D-FFT to the k-space data of one coil. As seen the data exhibits strong spatial distortions due to deliberately generated field inhomogeneities.
b) shows the VSM obtained by estimating field inhomogeneities like explained above and dividing by the bandwidth in phase-encode direction.
c) shows the sensitivity map $\tilde{C}$ before the wrapping algorithm is applied. It is visible that the shape of the sensitivity map does not match the coil image in a).
d) shows a wrapped sensitivity map $\tilde{C}$ used to calculate the reconstruction $\tilde{\mathbf{v}}$.
The third column of fig. 5.10c) shows the final reconstruction result $\mathbf{v}$.

4.5 EPI Phase Maps

As mentioned earlier most of today's commercial scanners tackle EPI Nyquist ghosts by executing reference shots prior to the actual image reconstruction. The aim of this work is to estimate phase maps using only the obtained image data. At the same the usage of reference shot data in the iterative reconstruction scheme is also implemented. As a result the reconstruction results with image-based phase map can be compared to reconstruction results with reference data, as done in chapter 5 where the results are presented.

4.5.1 Reference Calibration Scans

For an EPI reference calibration scan, phase-encoding gradients G_{PE} are turned off. Using a readout gradient G_{RO} data is acquired in the same way as in a common EPI measurement. Under ideal conditions, all collected echoes should be identical, because G_{PE} is absent. Figure 4.7a) shows a schematic of such a reference scan, obtained. In fig. 4.7b) it is visible, that the argument of two adjacent phase trends is not equivalent.

Due to the background gradients introduced by eddy currents, described in sec. 3.2.5, a k-space shift results. The shift Δk_{shift} respectively linear phase variation, defined in eq. 3.8 and eq. 3.9, lead to the behaviour that *odd* and *even* echoes are not aligned and the echo positions alternate from row to row.
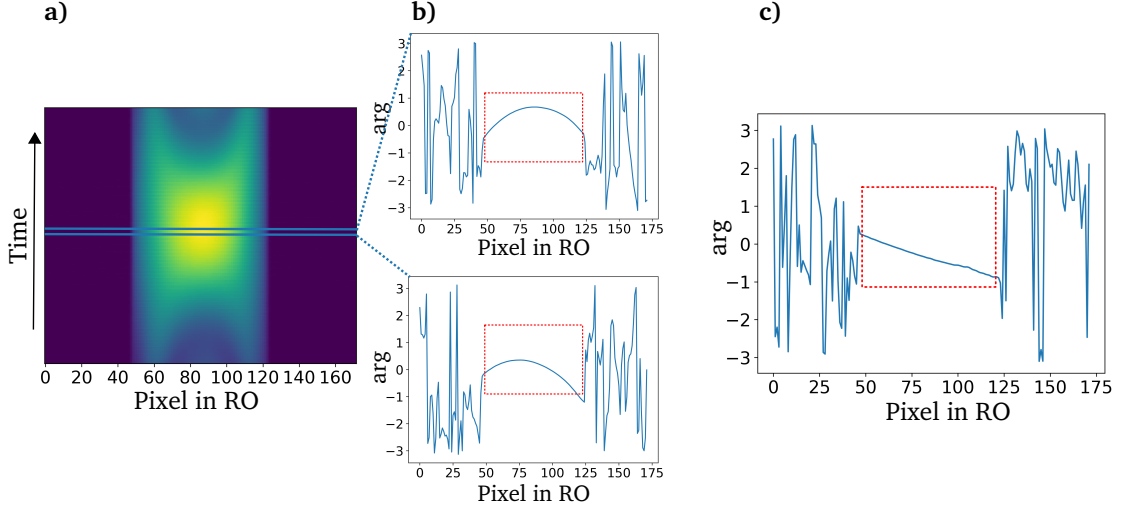
Figure 4.7: Measurement and calculation of EPI reference data.
a) shows the measurement of EPI reference data. The shown image represents the data loaded from one coil of the surface coil array. As seen different echoes are collected. *Odd* echoes are already reversed in the image.
b) shows the argument of the *even* echo on the top, and the argument of *odd* echo on the bottom.
c) shows the angle between the *odd* and *even* echoes depicted in the middle column. As expected, the argument shows a linear trend. Thus, the phase error stems from eddy current induced echo misalignment.

Denoting the echo ν and the measured data of the calibration scan as $m_\nu^C(k_x)$, the phase distorted signal is denoted as $m_\nu^{C'}(k_x)$. The 1D-FFT in RO direction is termed $\tilde{m}_\nu^{C'}(x)$. The relation between the distorted and undistorted signal of the calibration scan is then given by

$$m_\nu^{C'}(k_x) \xrightarrow{1D-FFT} \tilde{m}_\nu^{C'}(x) = \tilde{m}_\nu^C(x)\, e^{j\Phi_\nu^C(x)}. \tag{4.27}$$

$\tilde{m}_\nu^C(x)$ is the undistorted signal. The phase $\Phi_\nu^C(x)$ can be found by calculating the angle between an *odd* and *even* echo. Figure 4.7b) shows the phase of an *odd* respectively *even* echo. The angle between these two echoes is displayed in fig. 4.7c). As expected the phase trend is linear. The calculated phase difference can be used to correct for Nyquist ghosting by the definition of a correction phase. This phase is defined by

$$\Phi_\nu^{CORR}(x) = -\Phi_\nu^C(x). \tag{4.28}$$

In this work the correction phase is termed $\Delta\Phi_{REF} = \Phi^{CORR}$. Thus, $\Delta\Phi_{REF}$ corrects the phase error stemming from Nyquist ghosts for all *odd* echoes. It is applied to the actual measured *odd* echoes $m_\nu^{M'}(k_x)$ in the k_y-x domain [2], thus

$$m_\nu^{M'}(k_x) \xrightarrow{1D-FFT} \tilde{m}_\nu^M(x) = \tilde{m}_\nu^{M'}(x)\, e^{j\Phi_\nu^{CORR}(x)}. \tag{4.29}$$

This way the non-distorted signal $\tilde{m}_\nu^M(x)$ is found. Applying the correction phase in that way is termed a *non-linear phase correction* [3]. It is ideal because it also corrects for phase errors not stemming from eddy current induced phase shifts. An example for these effects are the cutoff characteristics of applied filters. A *linear phase correction* is based on performing an echo peak detection, then calculating linear and constant phase terms for the correction. This can lead to remnant ghosts as e.g. these cutoff characteristics of applied filters are not considered [3].

Fig. 4.8 shows the result of performing the introduced *non-linear phase correction* on a coil image.

a) **b)**
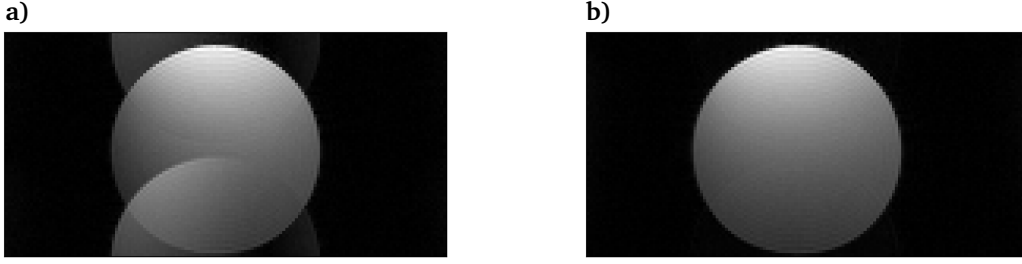
Figure 4.8: Coil image before and after applying EPI reference based phase correction.
a) shows input data of a single surface coil channel after applying a 2D-FFT.
b) shows the single surface coil channel, after the phase correction described in this section was applied. Consequently all *odd* echoes were phase corrected with data obtained from a EPI reference measurement.

The applied phase reference is a 1D correction, since all *odd* echoes are corrected with the same phase, derived by dividing an *odd* and an *even* echo in the area with the highest SNR.

An extension to this method uses two RF excitations, shifting the second image by one echo [3]. Therefore, *odd* echoes of the first dataset are *even* echoes in the second and vice versa. This can help to alleviate effects stemming from time dependent phase effects like field inhomogeneities because corresponding echoes are measured at the same time after excitation.

4.5.2 Image-Based Phase Maps

As noted earlier the main objective of this work is to replace the EPI reference scan with an image-based phase map. This phase map should be jointly estimated with the image itself. Fig. 4.9 shows the input node of the calculation which represents the full set of raw k-space data.

First the raw k-space is split using binary sampling masks M_{so} and M_{se}. These set all *odd* respectively *even* echoes to zero. Therefore, the resulting image obtained by reconstruction does not exhibit any Nyquist ghosts.

Using the binary sampling mask M_{so}, which sets all *even* echoes to zero, the cost functional

$$J(\mathbf{v}_o) = ||\mathbf{A}\mathbf{v}_o - \mathbf{m}||_2^2 \qquad \mathbf{A} = M_{so}\mathbf{E}C \quad , \tag{4.30}$$

is used to find the reconstruction $\mathbf{v}_o$. In the same manner the even reconstruction is found [4] using

$$J(\mathbf{v}_e) = ||\mathbf{A}\mathbf{v}_e - \mathbf{m}||_2^2 \qquad \mathbf{A} = M_{se}\mathbf{E}C \quad . \tag{4.31}$$

Using these two reconstructions, a full phase map $\Delta\Phi_{FULL}$ is obtained with

$$\Delta\Phi_{FULL} = arg(\mathbf{v}_e^* \, \mathbf{v}_o). \tag{4.32}$$

The application of the binary sampling masks introduces additional undersampling and increases the g-factor non-linearly, as quantified in eq. 2.23. The SNR reduction scales with $\frac{1}{\sqrt{R}}$. Therefore, the SNR reduction increases non-linearly with additional undersampling. This can introduce additional artefacts in the obtained $\Delta\Phi_{FULL}$, as shown in sec. 5.1.

To alleviate g related *noise amplification*, *odd* and *even* echoes are reconstructed jointly [4] using a so called *Model 2* reconstruction

$$J(\mathbf{v}) = ||\mathbf{A}\mathbf{v} - \mathbf{m}||_2^2 \qquad\qquad \mathbf{A} = \sum_{k=1}^{2} M_s{}^k \, \mathbf{E} \, C \, \Phi^k$$
$$M_s{}^1 = M_{se} \, , \, M_s{}^2 = M_{so} \qquad \Phi^1 = e^{j0} \, , \, \Phi^2 = e^{j\Delta\Phi_{FULL}} \quad . \tag{4.33}$$

The obtained phase map $\Delta\Phi_{FULL}$ is integrated into the sensitivity maps, yielding so called *composite sensitivity profiles* [34]. Therefore, in the *Model 2* reconstruction the number of sensitivity profiles is effectively doubled. Thus, using three iterative CG reconstructions Nyquist ghosts and the images are jointly reconstructed. This whole procedure is visualised in fig. 4.9.
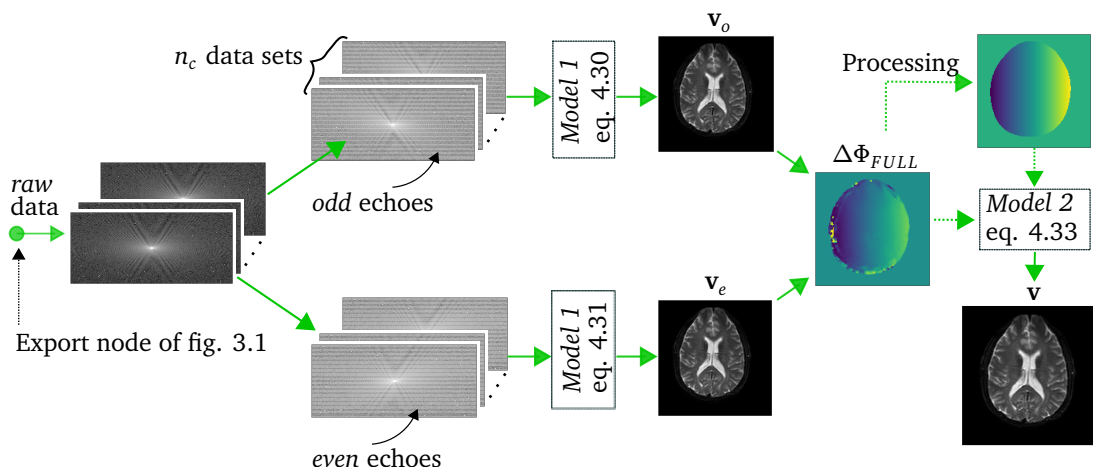
Figure 4.9: Calculation of image-based phase maps.
The imported *k*-space *raw* data is divided into *odd* only and *even* only echoes using binary sampling masks. Separate images are reconstructed and are used to calculate the 2D phase map $\Delta\Phi_{FULL}$. Finally, a joint reconstruction of all data is performed, termed *Model 2* reconstruction. Therefore, a joint image reconstruction and Nyquist ghost correction is performed while minimising *g*-factor noise amplification.
The processing steps are explained in sec. 5.2

Some intriguing questions can be derived directly from this procedure and shall be answered in the following results chapter. First of all, it is interesting how the usage of this 2D phase map $\Delta\Phi_{FULL}$ compares to the usage of $\Delta\Phi_{REF}$, obtained by separate reference measurement beforehand. To study this effect the reference correction was applied in the preprocessing step of the presented iterative reconstruction fig. 4.5. Therefore, the reconstruction follows the same algorithm as the reconstruction using image-based phase map. Thus, in the reconstruction using reference data only one iterative reconstruction is needed. This iterative solution is equivalent to eq. 4.33, without extension of the sensitivity profiles to composite sensitivity profiles. This procedure is needed because the reconstruction in the MRI scanner has multiple other modules which are not considered for this work. This includes filtering of the final reconstruction. Furthermore, the scanner reconstruction unit uses an analytical SENSE instead of an iterative solution. The advantage of this proposed iterative reconstruction algorithm is, that the algorithm to numerically solve the model can easily be exchanged. Furthermore, different regularisation methods can be added. The final reconstruction using an iterative algorithm is compared to the scanner reconstruction in fig. 5.4-5.6.

$\Delta\Phi_{REF}$ is an example of a 1D phase map, since all *odd* echoes are corrected in the same manner, using the Φ^{CORR} defined in eq. 4.28. By contrast using $\Delta\Phi_{FULL}$ the correction for *odd* echoes is performed differently depending on the *y* respectively PE direction. Using averaging, it is also possible to transform the $\Delta\Phi_{FULL}$ phase map to a 1D maps. Therefore, it should be compared how the usage of such a 2D phase map compares to the usage of a 1D phase map.

Another crucial assessment if the behaviour of the algorithm in cases of high acceleration. Due the effectively doubled acceleration factor in the calculation of $\Delta\Phi_{FULL}$ this iterative algorithm is especially sensitive to high acceleration.

While the results presented in the next chapter were obtained for single slice measurements, with slices being located close to the isocenter, it will also be studied if phase maps can be reused to reconstruct adjacent slices. If the phase map can be reused, the number of iterations of algorithm depicted in fig. 4.9 reduces from three to one.

5 | Results

5.1 Image-Based Phase Maps for Accelerated and Non-Accelerated EPI Measurements

First multiple non-accelerated phantom and in vivo measurements were performed. Two different $\Delta\Phi_{FULL}$ are shown in fig. 5.1. Figure 5.1a) shows the phase map obtained when measuring a phantom. Fig. 5.1b) shows the phase map for an in vivo measurement. Both phase maps were obtained from measurements with no acceleration R=1. Nonetheless as explained in sec. 4.5.2 the phase maps are calculated with an effective acceleration factor of R=2, due to the fact that *odd* and *even* echoes are treated separately in the reconstruction.

5.1.1 Phase Map Trend as a Function of Coordinates

For all plotted rows of the phase map linear phase variation across the phase map is visible. Following the theory on Nyquist ghosts, introduced in sec. 3.2.5, this behaviour was expected. Furthermore, fig. 5.1a) shows three different rows of the phase map. A linear fit can be used to assess the difference between these three rows. The calculated slope k and intercept d per row varied slightly. For the top row the calculated values were $k_1 = 0.034\frac{\text{rad}}{\text{pixel}}$ and $d_1 = -0.361$pixel, based on the zero pixel located at the left end of the image. The fit coefficients for the row in the middle were $k_2 = 0.035\frac{\text{rad}}{\text{pixel}}$ and $d_2 = -0.363$pixel. The row on the bottom shows slightly varying coefficients of $k_3 = 0.036\frac{\text{rad}}{\text{pixel}}$ and $d_3 = -0.372$pixel. The average variation of all fitted slopes was found to be 2.15%, while the average variation of intercepts was found to be 1.65%.

Therefore, it can be concluded that for the phantom measurement, the steepness of the slope increases slightly for different rows in the phase map. In contrast for the in vivo measurement also fitting coefficient were found, but not showing a clear trend for the trend in variation. For the top row $k_1 = 0.051\frac{\text{rad}}{\text{pixel}}$ and $d_1 = -2.286$pixel. The results for the middle row coefficients were $k_2 = 0.052\frac{\text{rad}}{\text{pixel}}$ and $d_2 = -2.367$pixel. For the bottom row $k_3 = 0.051\frac{\text{rad}}{\text{pixel}}$ and $d_3 = -2.551$pixel was found. Therefore k varied on average by around 6.44% and the variation of d was on average 6.54%.

As suggesting for the presented value, the steepness of the linear phase trend increases for fig. 5.1a) from top to bottom. Fig. 5.1b) in contrast shows a similar steepness for the rows on the top and bottom. This behaviour is different for every measurement, therefore no general rule for the slope and intercept variation was derivable.

A few remarks should be added to the validity of this calculation. First of all the statistical population is small and consequently it is difficult to draw a conclusion from this analysis. Furthermore, the calculated values only differ in the third decimal place. The slope variation for different rows was also noted in other work [4].

In general it was found to be favourable to use a slight denoising before using the phase maps. Therefore, all phase maps were wavelet filtered [35]. As shown in fig. 5.1 the unfiltered trend (in blue) shows small signal fluctuation. These fluctuations were successfully filtered out using wavelet filters, as the orange trends suggests.
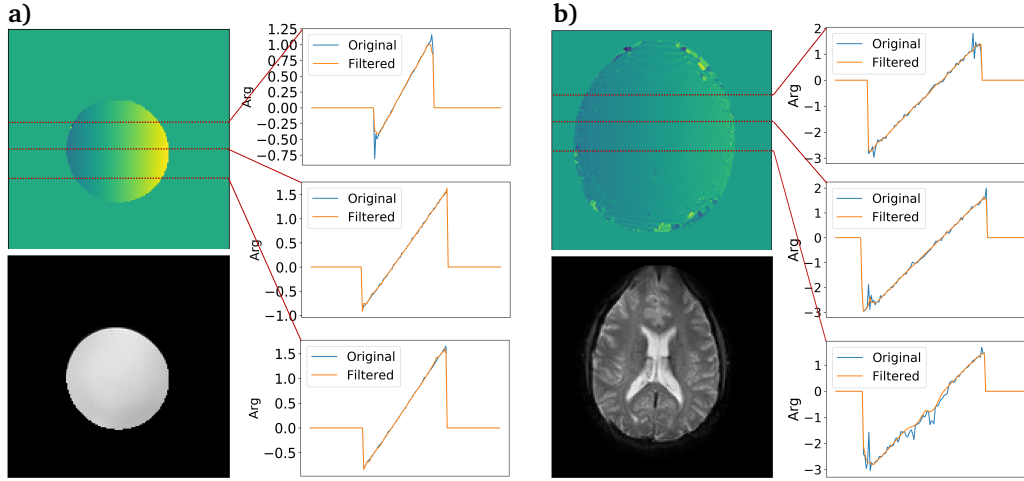
Figure 5.1: 2D phase map $\Delta\Phi_{FULL}$ for a phantom and in vivo measurement for R=1 measurements. **a)** shows the phase map for a phantom measurement. The image was collected using a SE sequence with a FOV of 280mm and 8mm thick slices in the isocenter. The three rows show different phase map trends, showing a linear variation from left to right.
b) is the phase map of an in vivo measurements collected using a GRE sequence with a FOV and 4mm thick slices.
For a) and b) the blue *original* trend represents one row of the phase map. The filtered trend was obtained by applying a *wavelet* filter as explained in this section.

5.1.2 Reduction Factor Dependent Phase Map Artefacts

The phase maps shown in fig. 5.1 were collected for unaccelerated measurements. For increasing acceleration, noisy propagation behaviour is visible. Fig. 5.2 shows that already for a *g*-factor increase to around 3, as shown in fig. 5.2b), strong artefacts in the phase map are visible. Thus, already for R=2 measurements artefacts are visible.

In the case of a noise only signal, the distribution of the phase noise is uniform [36]. This can be visualised by noting that noise only complex data for a noise only vector has the same probability for all directions. If a signal is present, the phase noise can be modelled as gaussian. The variance of the gaussian distribution decreases inversely proportional to the SNR. Therefore, with a decreasing SNR the angle calculated between the *even* and *odd* reconstruction shows greater variation. In the case of a SENSE reconstruction the SNR decreases nonlinearly with increasing acceleration, see sec. 2.3.3. Therefore, the calculation of the angle between the *even* and *odd* reconstruction is especially sensitive to high acceleration factors.

Estimation errors in the phase propagate into the final reconstruction, see also [37]. This is clearly visible for the final reconstruction in 5.2b) and 5.2c). It can be concluded, that for these cases the usage of a full 2D phase map $\Delta\Phi_{FULL}$ is not appropriate. The problem of noisy phase maps is aggravated by the fact that the effective reduction factor for the calculation of phase maps is doubled, see fig. 4.9.

5.2 Phase Map Averaging and Masking

Figure 5.4 shows different reconstructions for measurements with no acceleration. For SE acquisitions in fig. 5.4a) and 5.4b) the usage of $\Delta\Phi_{FULL}$ yields the reconstruction $\mathbf{v}_{\Delta\Phi_{FULL}}$. No artefacts are visible for these reconstructions. Figure 5.4c) shows a R=1 measurement obtained with a GRE sequence. For the reconstruction with $\Delta\Phi_{FULL}$ some artefacts are already visible.

Furthermore, when acceleration is used, 2D phase maps $\Delta\Phi_{FULL}$ show strong artefacts. As explained in the last section for an acceleration factor of R=2, artefacts are induced in the final reconstruction. This is in accordance with the in vivo result of fig. 5.5c), where the most left picture
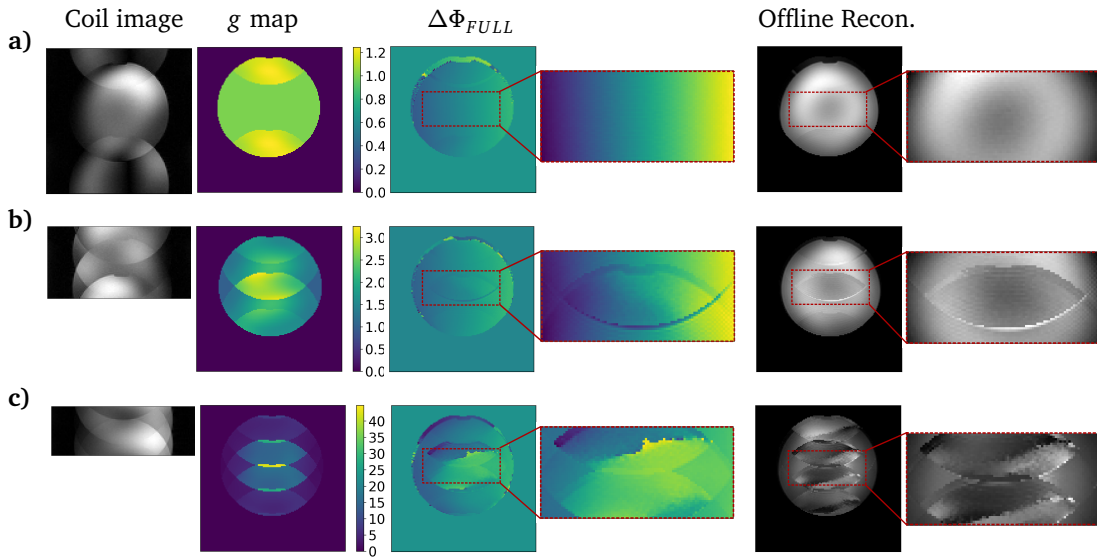
Figure 5.2: 2D phase map, g-factor map and final offline reconstruction for increasing acceleration. **a)** was collected using a non-accelerated R=1 image. For **b)** R=2 and **c)** R=3 reduction was used. The first column shows the coil images, which is the 2D-FFT of the input data of one single surface coil. The total number of coils for the whole set of measurements was n_c=13. The second column shows the g-factor map for an effectively doubled acceleration.
Errors in the full $\Delta\Phi_{FULL}$ phase map propagate into the final reconstruction.

shows artefacts.

Therefore, two additions to the phase map procedure were introduced to alleviate the noisy behaviour of $\Delta\Phi_{FULL}$. These two methods are denoted $\Delta\Phi_{AVG}$ and $\Delta\Phi_{AVG,M}$. To calculate those, first the full phase map $\Delta\Phi_{FULL}$ is calculated. An example of such a phase map, obtained from an R=3 measurements is shown in 5.3b). To calculate $\Delta\Phi_{AVG}$ from the 2D phase map $\Delta\Phi_{FULL}$, a linear fit for all rows in the phase map is obtained. Such a fit yields an intercept k and slope d. The collected slopes and intercepts of all rows are averaged to calculate k_{avg} and d_{avg}. Using k_{avg} and d_{avg} a linear phase ramp can than be calculated, which is equal for all rows. Following this the phase map is fitted into the object indicator map Ω obtained from thresholding sensitivity maps, see sec. 4.2.2. This procedures yields $\Delta\Phi_{AVG}$ shown in fig. 5.3c). Therefore, the phase variation in $\Delta\Phi_{AVG}$ is the same for all lines and can be calculated using k_{avg} and d_{avg}.

For the calculation of $\Delta\Phi_{AVG,M}$ the procedure is in principle repeated. For increasing acceleration the phase maps tends to show a lot of non-smooth, fluctuating behaviour. Stemming from this observation, the lines used in the fitting algorithm are reconsidered. $\Delta\Phi_{FULL}$ in fig. 5.3b) shows noisy behaviour in the central image area. As these areas exhibit a lot of phase fluctuation a linear fitting algorithm produces wrong or inconsistent results. Figure 5.3b) shows that the areas of strong noise artefacts resemble the g-factor map in fig. 5.3a). To calculate the g-map in fig. 5.3a), the mean of all non-zero g-factor values was taken. All values lying more than 20% above the mean of the g are masked and thus are shown in white. Therefore, the white values define a mask, which leads to exclusion of the masked values in the linear fitting process. To be specific, every row which includes such a *white*, masked value is not used for the calculation of average intercept and slope values, denoted $k_{avg,m}$ and $d_{avg,m}$. This masking reduces the number of total rows used in the fitting process. It can also potentially help to reduce the number of rows which are too noisy to fit properly and which consequently result in faulty coefficients.

Afterwards analogue to the previous 1D method the calculated $k_{avg,m}$ and $d_{avg,m}$ are used to calculate $\Delta\Phi_{AVG,M}$, shown in fig. 5.3d). It is visible that this averaged phase map varies to the one in 5.3c). Therefore, in general $\Delta\Phi_{AVG}$ and $\Delta\Phi_{AVG,M}$ are not identical.

a) Masked g-map   **b)** $\Delta\Phi_{FULL}$ **c)** $\Delta\Phi_{AVG}$ **d)** $\Delta\Phi_{AVG,M}$
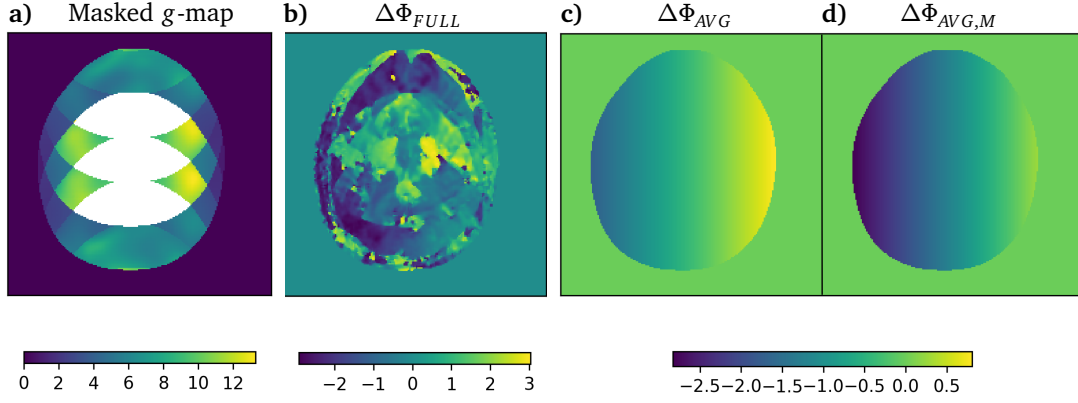
Figure 5.3: Averaging procedure for two-dimensional phase maps.
a) Shows a g-map, where values larger than 20% of the mean g value are masked. The masking is indicated by the white areas. **b)** shows a full 2D phase map $\Delta\Phi_{FULL}$, obtained from an R=3 measurement. Thus, the effective acceleration factor of the phase map calculation is R=6. This explains the noisy behaviour in the central phase map region.
c) shows a 1D phase map, calculated by averaging all linear fit coefficients of **b)**. The calculated phase trend using the average fit coefficients is then masked with the object indicator map Ω, yielding the result seen and denoted as $\Delta\Phi_{AVG}$. The algorithm to calculate $\Delta\Phi_{AVG,M}$ as shown in **d)** is qualitatively equivalent to the one of the calculation of **c)**. The key difference is that for the calculation of $\Delta\Phi_{AVG,M}$, the values in **b)** which are masked by the white mask of **a)** are excluded from the fitting procedure.

5.3   2D and 1D Phase Maps for Increasing Acceleration Factors

To assess the viability of image-based phase maps the *Python* framework was prepared to read-in the EPI reference data. Per measurement this reference data consists of n_c data sets. Using the principles elaborated in sec. 4.5.1, the EPI reference data is used for the coil-wise correction of the measurements. The corrected and uncorrected data for one surface coil is shown in fig. 4.8. Because the Nyquist ghost is already accounted for, there is no need to calculate image-based phase maps. Therefore, the corrected data is used to directly calculate a final off-line reconstruction using the reconstruction defined via. eq. 4.22.

The third column of fig. 5.4-5.6 shows the reference image calculated in this way. On the outmost right of fig. 5.4-5.6 the image as reconstructed by the MRI scanner's *recon2* pipeline is shown. A few things can be noted from the comparison of these two. First of all it is visible, that both reconstructions yield images with an equivalent quality. There are no residual Nyquist ghosts visible. Second of all the scanner reconstruction still differs slightly. This difference can be explained by the fact that the scanner's *recon2* reconstruction pipeline has multiple modules which were not implemented in the off-line reconstruction pipeline for this work. An example for this are different filtering modules.

For the assessment of the different introduced image-based phase maps multiple reconstruction were implemented and compared. The structure of this assessment can be seen in the fig. 5.4-5.6. First the reconstruction using full 2D phase maps $\Delta\Phi_{FULL}$, the averaged phase maps $\Delta\Phi_{AVG}$ and $\Delta\Phi_{AVG,M}$ are calculated. This represents the first to third column, thus the reconstructions $\mathbf{v}_{\Delta\Phi_{FULL}}$, $\mathbf{v}_{\Delta\Phi_{AVG}}$ and $\mathbf{v}_{\Delta\Phi_{AVG,M}}$. Following the EPI reference data is used for the correction of Nyquist ghosts, and the corrected data is used to calculate a reference image $\mathbf{v}_{ref}$.

Therefore, $\mathbf{v}_{ref}$ can be seen as a reference. Using this reference an error of the image-based reconstructions can be obtained. The second column of fig. 5.4-5.6 shows the absolute magnitude difference of the reconstruction and the reference image $\mathbf{v}_{ref}$. The values stated below are the nRMSE error of the magnitudes added over all pixels. Therefore, the nRMSE for the offline

reconstruction using the full phase map $\Delta\Phi_{FULL}$, can be calculated by

$$nRMSE = \sqrt{\frac{\sum_n^N (\,|v_{n,\Delta\Phi_{FULL}}| - |v_{n,ref}|\,)^2}{\sum_n^N (\,|v_{n,ref}|\,)^2}}\,. \tag{5.1}$$

In this eq. the error is added over all pixels. The nRMSE for $\mathbf{v}_{\Delta\Phi_{AVG}}$ and $\mathbf{v}_{\Delta\Phi_{AVG,M}}$ are calculated in the same manner. The results for measurements obtained without acceleration are shown in fig. 5.4. As mentioned before, the calculation of the phase map $\Delta\Phi_{FULL}$ is done with an effective acceleration factor of $R = 2$. First the SE results in fig. 5.4a) and fig. 5.4b) shall be examined. It is visible that the three different phase maps produce results that are equivalent to $\mathbf{v}_{ref}$. Therefore, the joint calculation of the image and the phase maps produces equivalent results to the usage of reference data. In fig. 5.4a) and fig. 5.4b) it is also noticeable that the nRMSE of $\mathbf{v}_{\Delta\Phi_{FULL}}$ is slightly larger than for $\mathbf{v}_{\Delta\Phi_{AVG}}$ and $\mathbf{v}_{\Delta\Phi_{AVG,M}}$. At the same time the visual quality of the reconstruction is equivalent for all reconstructions. Nonetheless, even for these measurements obtained without acceleration it seems favourable to use an averaged phase map.

For data collected with GRE sequences, phase inconsistencies can lead to artefacts in the final reconstruction. One example is shown in fig. 5.4c), where the usage of $\Delta\Phi_{FULL}$ leads to artefacts in areas where pixels are superimposed. Due to the effectively doubled acceleration factor of the phase map calculation, these artefacts already occur in for R=1 measurements. Therefore, in these cases the usage of $\Delta\Phi_{AVG}$ or $\Delta\Phi_{AVG,M}$ does significantly improve the reconstruction. From this it can be concluded that for measurements obtained with GRE sequences the usage $\Delta\Phi_{FULL}$ results in artefacts. Consequently, GRE measurements should always be reconstructed with an averaged phase map.

In general in can be concluded that while the usage of the 2D phase map $\Delta\Phi_{FULL}$ is possible for measurements obtained without acceleration and with SE sequences. In case of GRE sequences the usage of $\Delta\Phi_{FULL}$ can already induce artefacts. Thus, GRE sequences should always be reconstructed using $\Delta\Phi_{AVG}$ or $\Delta\Phi_{AVG,M}$. It should also be noted that the usage of $\Delta\Phi_{FULL}$ is computationally less demanding. The averaging process described in sec. 5.2 requires a phase unwrapping procedure which is computationally expensive.

Figure 5.5 summarises the results for R=2. The phantom results shows that $\Delta\Phi_{FULL}$ can still produce a ghost free image in the case of twofold acceleration. In this case use to the small cross section of the phantom, $\mathbf{v}_{\Delta\Phi_{AVG}}$ has some small residual artefacts. This is alleviated with the usage of $\mathbf{v}_{\Delta\Phi_{AVG,M}}$.

For the in vivo measurements in fig. 5.5b) and 5.5c) $\mathbf{v}_{\Delta\Phi_{FULL}}$ show significant artefacts in the central image area. $\mathbf{v}_{\Delta\Phi_{AVG}}$ and $\mathbf{v}_{\Delta\Phi_{AVG,M}}$ produce equivalently artefact free images. Thus, for the R=2 case the usage of $\Delta\Phi_{AVG}$ and $\Delta\Phi_{AVG,M}$ is favourable to yield results equivalent to $\mathbf{v}_{ref}$. Nonetheless, the result for $\mathbf{v}_{\Delta\Phi_{AVG,M}}$ 5.5c) shows a slightly higher nRMSE than the result for $\mathbf{v}_{\Delta\Phi_{AVG}}$. Inspecting $\mathbf{v}_{ref}$ and $\mathbf{v}_{\Delta\Phi_{AVG,M}}$ shows, that $\mathbf{v}_{\Delta\Phi_{AVG,M}}$ actually exhibits less artefacts. Thus, this results points out limits in the assessment of the reconstruction with an nRMSE. If $\mathbf{v}_{\Delta\Phi_{AVG,M}}$ has less artefacts than $\mathbf{v}_{ref}$, this will result in a high nRMSE, which incorrectly indicates reconstruction errors.

Figure 5.6 shows different in vivo results for the R=3 case. In all cases $\mathbf{v}_{\Delta\Phi_{FULL}}$ contains severe artefacts, which massively alter the reconstruction. The large amount of faulty values is represented by a nRMSE of around 0.40. Both $\mathbf{v}_{\Delta\Phi_{AVG}}$ and $\mathbf{v}_{\Delta\Phi_{AVG,M}}$ alleviate these artefacts and lead to better reconstruction. $\mathbf{v}_{\Delta\Phi_{AVG,M}}$ is a reconstruction qualitatively equivalent to $\mathbf{v}_{ref}$. For fig. 5.6b) $\mathbf{v}_{\Delta\Phi_{AVG,M}}$ can be seen as an improved reconstruction compared to $\mathbf{v}_{ref}$ or the scanner reconstruction. Therefore, equivalently to fig. 5.5c), this shows that when the scanner reconstruction contains artefacts itself, the reference image respectively the calculated nRMSE error looses validity.
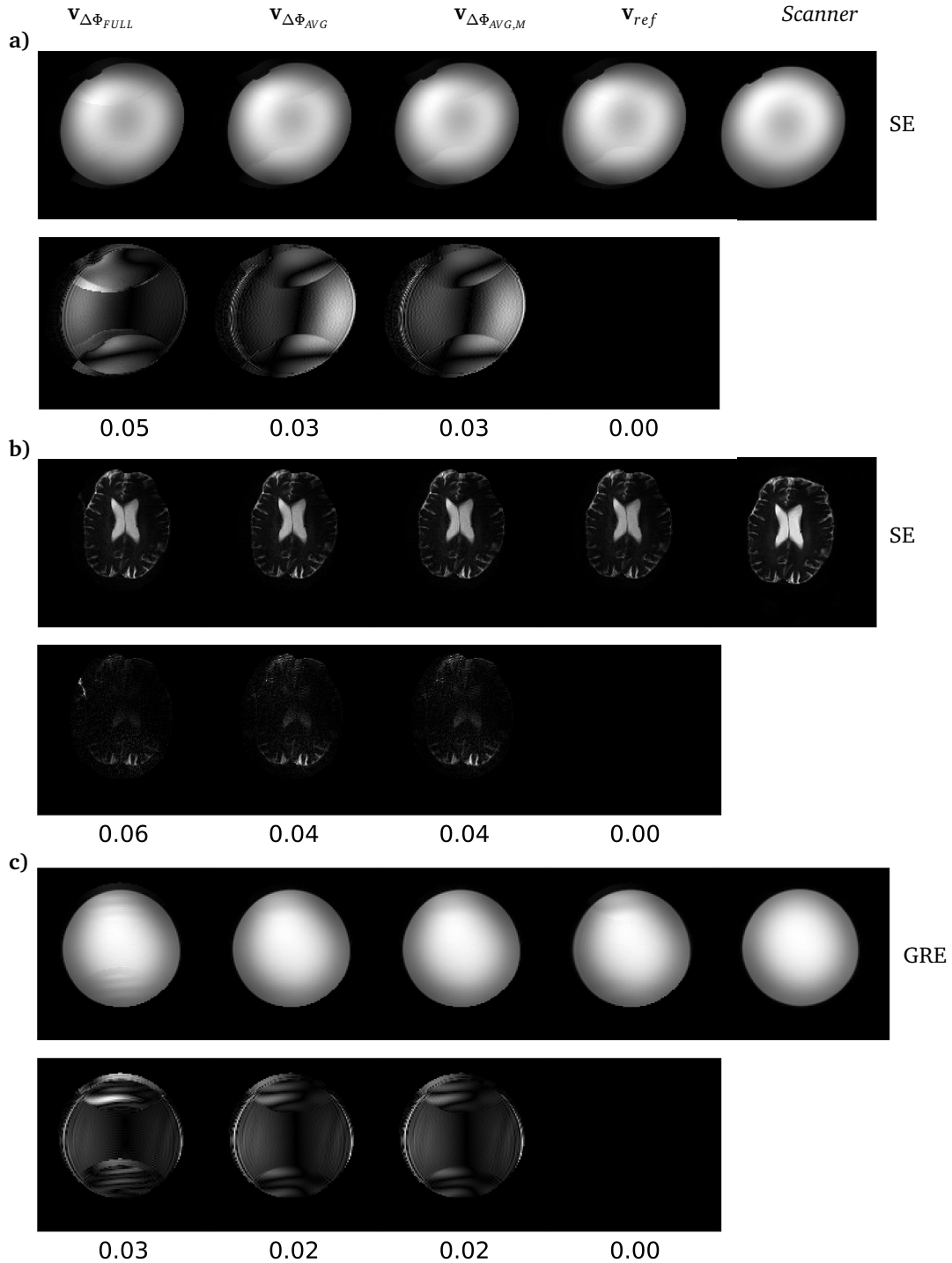
Figure 5.4: Reconstruction results for R=1.
a) shows a phantom measured in an oblique plane. The magnitude error of $\mathbf{v}_{\Delta\Phi_{FULL}}$, $\mathbf{v}_{\Delta\Phi_{AVG}}$ and $\mathbf{v}_{\Delta\Phi_{AVG,M}}$ are of similar appearance. The nRMSE for $\mathbf{v}_{\Delta\Phi_{FULL}}$ is slightly higher, with around 0.05.
b) shows an in vivo image collected in a $\mathbf{B}_0$=1.5T system. On the top left a slight geometric distortion is visible. Note that in contrast to the usual setup of this work, the phase-encode direction is from left to right. All results produce qualitatively similar results. No residual ghosts are visible.
c) shows the final reconstruction for a phantom measurement, imaged with a GRE sequence. As visible the usage of $\mathbf{v}_{\Delta\Phi_{FULL}}$ leads to residual ghosting in the final reconstruction.
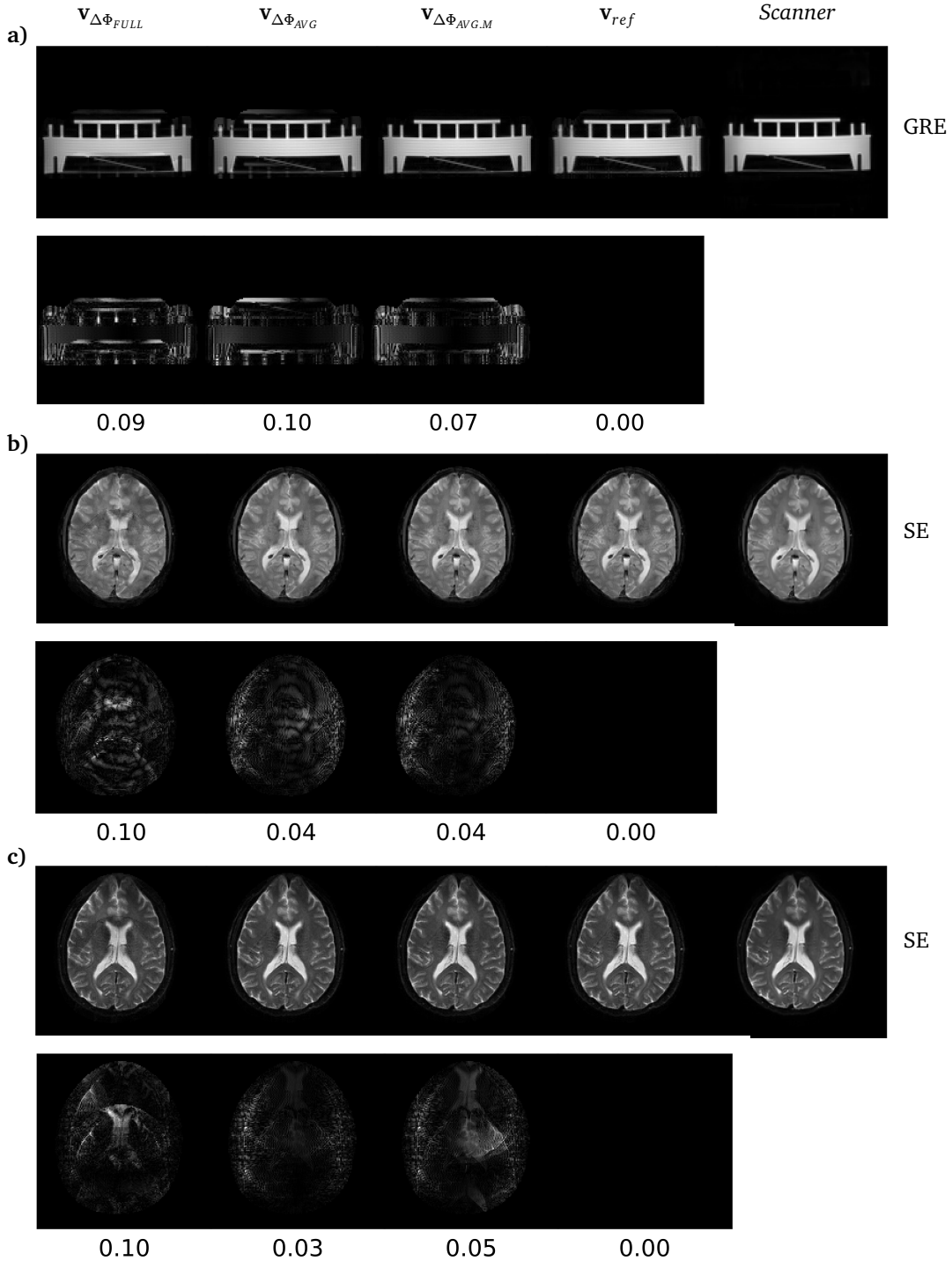
Figure 5.5: Reconstruction results for R=2.
a) shows the reconstruction of a phantom. Due to the small cross section cross section, The nRMSE of $\mathbf{v}_{\Delta\Phi_{AVG}}$ is higher than $\mathbf{v}_{\Delta\Phi_{FULL}}$.
b) shows an in vivo image collected with a GRE sequence. The reconstruction using $\Delta\Phi_{FULL}$ produces the highest nRMSE. As seen in the difference image on the final reconstruction $\mathbf{v}_{\Delta\Phi_{FULL}}$, this stems from the fact that there is a significant ghost remaining in the central image area.
c) shows the offline reconstruction an in vivo measurement collected with a SE sequence. The usage of $\mathbf{v}_{\Delta\Phi_{FULL}}$ leads to significant reconstruction artefacts in the central image area. Both $\mathbf{v}_{\Delta\Phi_{AVG}}$ and $\mathbf{v}_{\Delta\Phi_{AVG,M}}$ are qualitatively equivalent to $\mathbf{v}_{ref}$. Nonetheless nRMSE of $\mathbf{v}_{\Delta\Phi_{AVG,M}}$ is slightly higher.
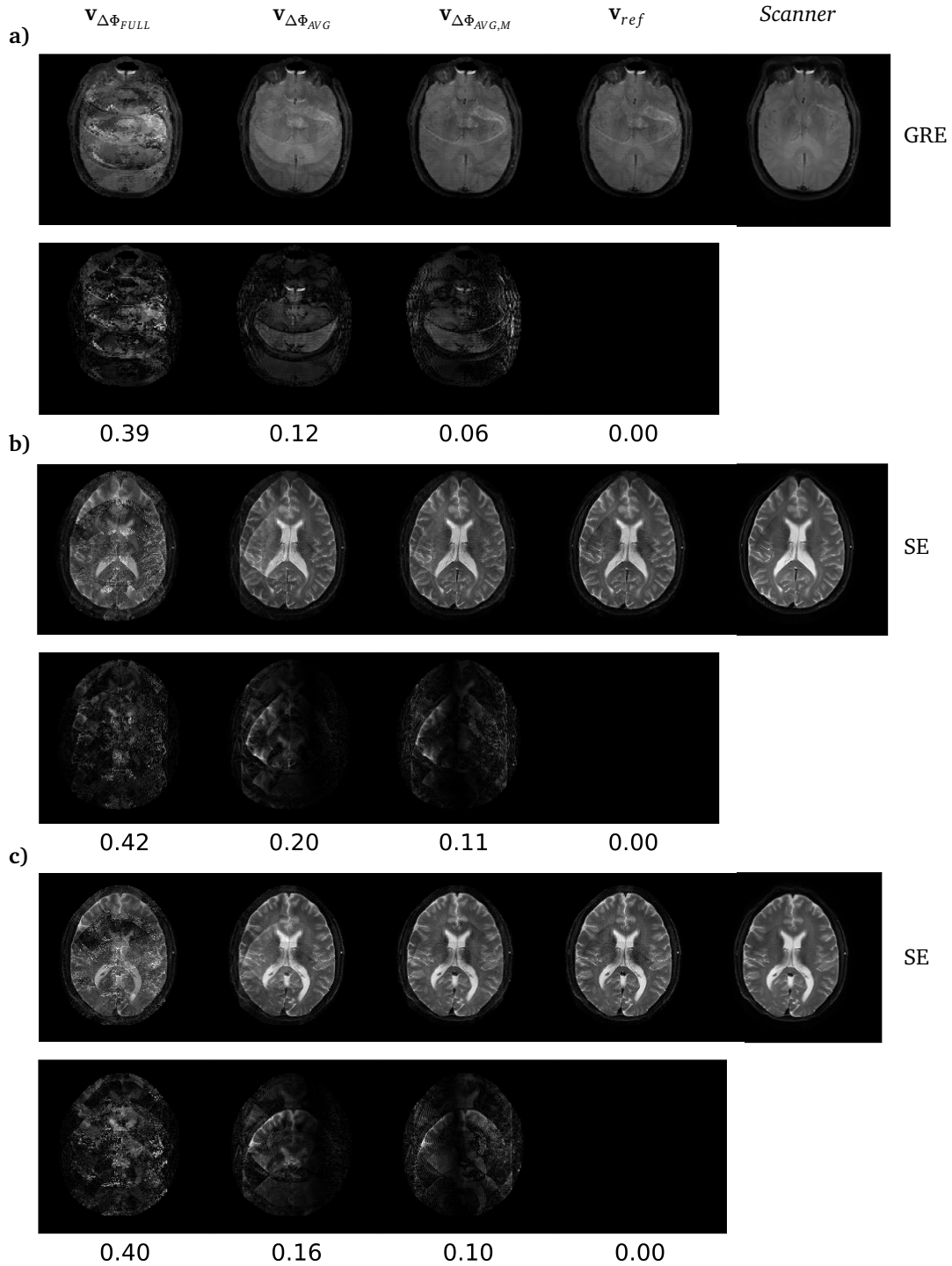
Figure 5.6: Reconstruction results for R=3.
a) shows that $\mathbf{v}_{\Delta\Phi_{FULL}}$ has severe artefacts. This is quantified by a nRMSE of 0.39. $\mathbf{v}_{\Delta\Phi_{AVG}}$ and $\mathbf{v}_{\Delta\Phi_{AVG,M}}$ gradually improve the reconstruction. As shown $\mathbf{v}_{\Delta\Phi_{AVG,M}}$ is visually equivalent to $\mathbf{v}_{ref}$.
b) and **c)** show that for again that the usage of $\Delta\Phi_{FULL}$ yields impractical reconstruction results. This effect can be alleviated by using $\mathbf{v}_{\Delta\Phi_{AVG,M}}$. As shown **b)**, the slight ghost remaining in $\mathbf{v}_{\Delta\Phi_{AVG,M}}$ has a different structure than the ghost in $\mathbf{v}_{ref}$, leading to a comparably large nRMSE. Nonetheless, the reconstruction $\mathbf{v}_{\Delta\Phi_{AVG,M}}$ can be interpreted as having less artefacts than and the scanner reconstruction.

Figure 5.7 summarises the results presented in this section. To calculate the bar plots the nRMSE of every reconstruction was stored. Second the measurements were categorised by acceleration factor R and *phantom* or *in vivo* measurements. The obtained nRMSE were averaged per category to yield an average nRMSE.

Figure 5.7a) shows that for measurements with no acceleration all three proposed image-based phase maps - $\Delta\Phi_{FULL}$, $\Delta\Phi_{AVG}$ and $\Delta\Phi_{AVG,M}$ - yield reconstructions with low nRMSE. As presented earlier for R=1 measurements obtained with GRE sequences, e.g. fig. 5.4c), artefacts were observed. This behaviour stems from phase inconsistencies in the areas where pixels are superimposed. This results in a slightly higher average nRMSE of 0.081 and 0.085 for the phantom respectively in vivo case. No difference was seen exhibited for the usage of $\Delta\Phi_{AVG}$ compared to $\Delta\Phi_{AVG,M}$. Both methods result in an average nRMSE of 0.071 in the phantom and of 0.056 for the in vivo case.

As mentioned earlier in the case of R=2, distinct artefacts can be seen. An example of these artefacts was presented in fig. 5.5b) and 5.5c). This reflects in the large decrease of nRMSE for the usage of $\Delta\Phi_{FULL}$ to $\Delta\Phi_{AVG}$, see fig. 5.7b). While the usage of $\Delta\Phi_{FULL}$ in the in vivo case yields an average nRMSE of 0.171, $\Delta\Phi_{AVG}$ and $\Delta\Phi_{AVG,M}$ results in an average nRMSE of 0.048 respectively 0.043. For phantom measurements the values in fig. 5.7b) from left to right are 0.125, 0.107 and 0.109.

Figure 5.7c) and fig. 5.6 show in accordance that the usage of $\Delta\Phi_{FULL}$ leads to severe artefacts respectively very large nRMSE. For $\Delta\Phi_{FULL}$ the average nRMSE amounts to around 0.395 for phantom and 0.504 for in vivo measurements. For phantom measurements $\Delta\Phi_{AVG}$ resulted in an average nRMSE of 0.093 and 0.173 for the in vivo case. The values for $\Delta\Phi_{AVG,M}$ were slightly lower, amounting to 0.085 for phantom and 0.159 for in vivo measurements. This shows that a successful reconstruction in the case of R=3 accelerated measurements requires $\Delta\Phi_{AVG,M}$.

Comparing fig. 5.7a) to 5.7c) shows that in general the average nRMSE increases with higher acceleration factors R. The increase for the usage of $\Delta\Phi_{FULL}$ is very large, from around 0.08 for R=1 to 0.4-0.5 for R=3. The nRMSE of $\Delta\Phi_{AVG}$ and $\Delta\Phi_{AVG,M}$ is 0.056 in the in vivo case, and increases to 0.173 respectively 0.159 for R=3. Therefore, for a full phase map $\Delta\Phi_{FULL}$ an increase from R=1 to R=3 leads to a sixfold increase of average nRMSE. Masking and averaging, respectively the usage of $\Delta\Phi_{AVG,M}$, only increases the nRMSE threefold for the same increase in acceleration.

Figures 5.4-5.6 summarise that image-based phase maps can be used for the reconstruction of EPI measurements. For all reconstructions the usage of $\Delta\Phi_{FULL}$ compared to $\Delta\Phi_{AVG}$ resulted in an equivalent or higher nRMSE. Thus, the reconstruction showed no improvement when using the full 2D phase map $\Delta\Phi_{FULL}$ compared to the averaged phase maps $\Delta\Phi_{AVG}$ or $\Delta\Phi_{AVG,M}$. To yield artefact free images for high acceleration factors, the phase map should be masked and and averaged. The usage of $\Delta\Phi_{AVG,M}$ yields results that are equivalent or in some cases even better than the $\mathbf{v}_{ref}$ or scanner reconstruction.
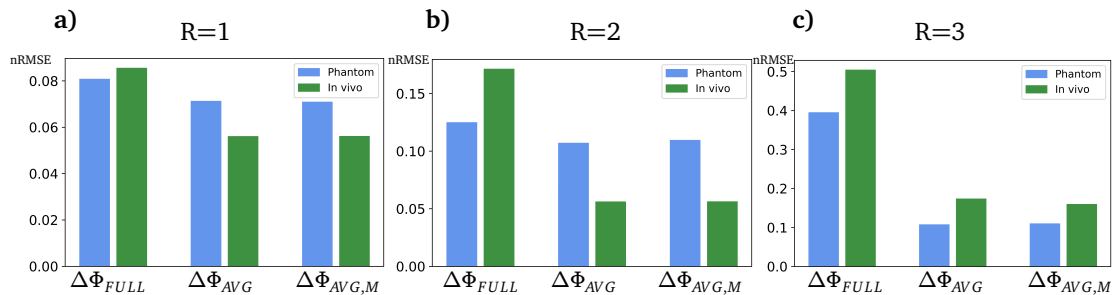
Figure 5.7: Average nRMSE of all reconstructions.
The bar plots summarises the results presented in this section. The average nRMSE for all measurements are shown for different acceleration factors. First these plots show that the average nRMSE for all measurements increases with acceleration. Second the approach method of averaging and averaging and masking leading to $\Delta\Phi_{AVG}$ respectively $\Delta\Phi_{AVG,M}$ help to reduce the increase of nRMSE. Therefore, when using a $\Delta\Phi_{FULL}$ nRMSE increases sixfold from R=1 to R=3. With the usage of $\Delta\Phi_{AVG,M}$ this increase is only threefold.

Figure 5.8 shows different reconstructions, obtained using $\mathbf{v}_{\Delta\Phi_{AVG,M}}$. Using fig. 5.6b) and 5.6c) as a starting point, the data is further by applying a binary sampling mask M_s. With the application of M_s additional echoes were zeroised, to achieve a higher acceleration factor. The effect of this additional, simulated acceleration is then assessed by calculating a offline reconstruction using $\Delta\Phi_{AVG,M}$. For R=3.2 no additional artefacts are visible. The results show that a further increase of acceleration lead to additional, severe artefacts. This behaviour stems from the effectively doubled acceleration of the phase maps and the difficulty to obtain a valuable linear fit coefficients for noisy phase maps. Therefore, it can be concluded that the proposed image-based phase maps and the following procedure to obtain $\Delta\Phi_{AVG,M}$ allow successful reconstruction of data collected with an acceleration factor of R=1 to R=3. This was shown in fig. 5.4-5.6. For high acceleration the masked and averaged phase map $\Delta\Phi_{AVG,M}$ has to be used. The reconstruction depends on obtaining a valid average slope and intercept. For acceleration factors R>3 the linear fitting procedure for the calculation of the average slope and intercept produces faulty values. Thus, significant errors in the reconstruction results, as visible in the figure below.
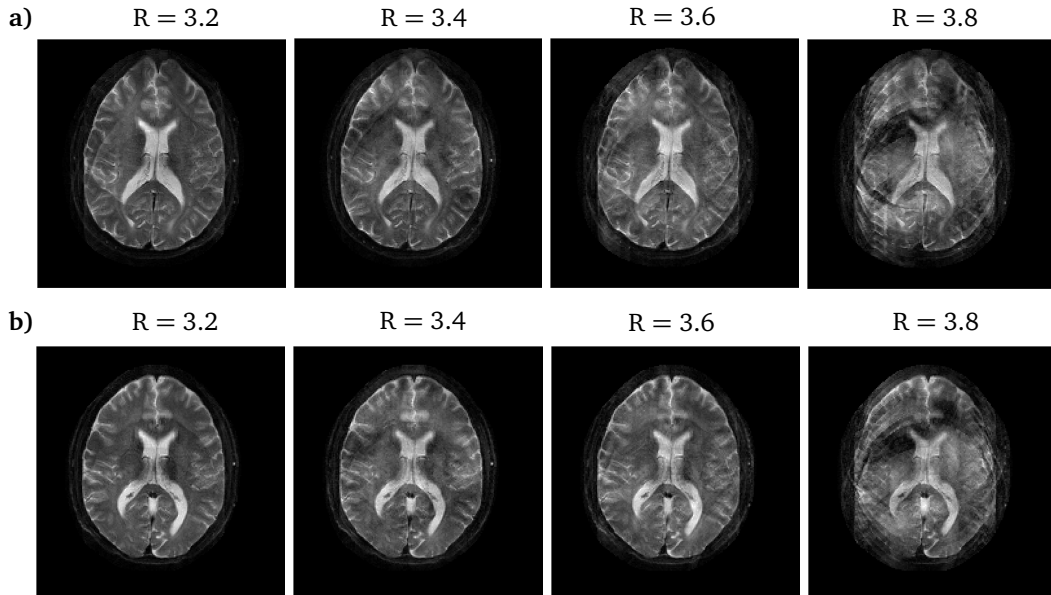
Figure 5.8: Reconstruction results for R>3.
The measurements of fig. 5.6**b)** and **c)** were further accelerated by zeroising collected echoes with a sampling mask M_s. The reconstructions were obtained using $\Delta\Phi_{AVG,M}$.
For an acceleration factor of R=3.2 no effect is visible. The results show that a further increase of acceleration lead to additional, severe artefacts. This behaviour stems from the effectively doubled acceleration of the phase maps and the difficulty to obtain a valuable linear fit coefficients for noisy phase maps.

5.4 Consideration of Off-Resonance Effects

In the methodology chapter under sec. 4.4.2 it was presented how measure $\Delta\omega_{B0}$ maps and consequently obtain a VSM. Furthermore, it was shown how to integrate VSM into the reconstruction algorithm. It was concluded that the most efficient integration can be achieved by mimicking the effect of $\Delta\omega_{B0}$ on sensitivity profiles. Thus, a wrapped sensitivity profile is calculated by linear interpolation and the result of the iterative algorithm is unwrapped as a final step of the reconstruction pipeline.

To assess the performance of this method, first a constant $\Delta\omega_{B0}$ was simulated by offsetting ω_0 by -300Hz. Fig. 5.9 summarises for the results. On the first column the so called *coil image* is shown, which is the 2DFFT of the data collected with one surface coil. The second column shows the VSM that was used to interpolated the sensitivity maps and inversely interpolate the final reconstruction, as described in sec. 4.4.2. The final offline reconstruction is presented in the third column, and the scanner reconstruction in the fourth column.

First the validity of the proposed algorithm was tested by assuming a VSM which is uniformly zero, which represents the assumption of neglectable field inhomogeneities. As shown in the third and fourth column of fig. 5.9a), the final offline reconstruction and the scanner reconstruction are equivalent. Therefore, it can be concluded, that in the case of diminishing field inhomogeneities the extended algorithm, which also accounts for field inhomogeneities, yields a Nyquist ghost free reconstruction.

Figure 5.9b) shows the application of a constant Larmor frequency offset which results in a VSM with a constant offset ~ 50 pixels. As shown in the first column, for such an offset the scanner reconstruction has significant errors. First due to the shifted coil sensitivities, signal cancellation occurs. Second of all is the SENSE reconstruction corrupted, as shown by the ripples on the bottom of the image. By contrast, the implemented offline reconstruction successfully reconstructs the image as shown in the third column. Also the non-smooth signal edge on the top is successfully reconstructed.
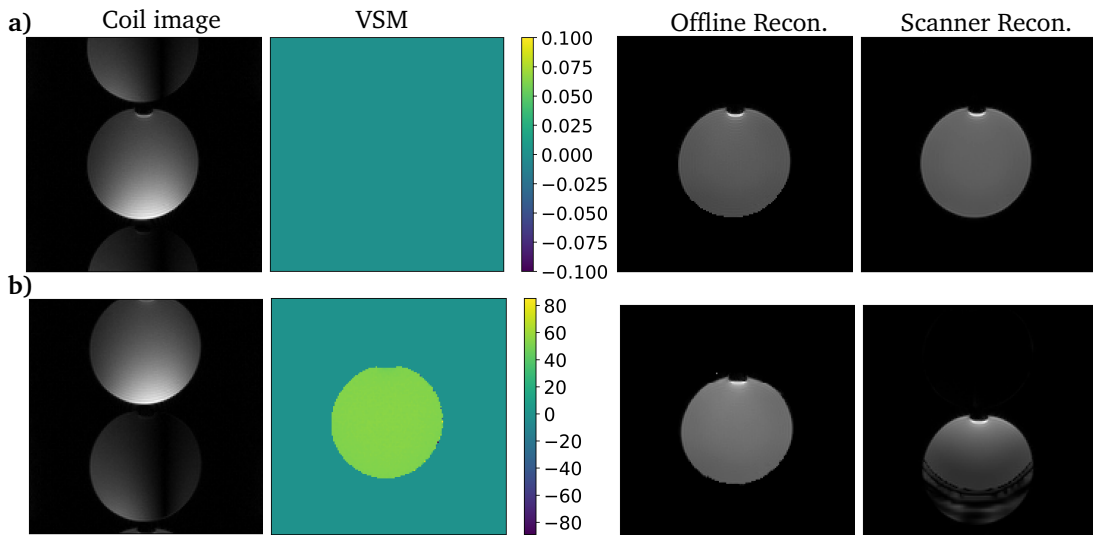
Figure 5.9: Effect of constant field inhomogeneities on the reconstruction.
The first column shows the 2DFFT of a single surface coil data set. The second row shows the VSM, found by dividing the field inhomogeneities by the bandwidth in phase-encode direction. The third column is the offline reconstruction obtained by the algorithm, which is compared by the scanner reconstruction in the fourth column.
a) Shows that the extended reconstruction proposed under sec. 4.4.2 works successfully when no field inhomogeneity is present, thus VSM is uniformly zero. In this case the implemented offline reconstruction and scanner reconstruction are equivalent. Thus, the extended algorithm accounting for field inhomogeneities yields a successful reconstruction without Nyquist ghosting when no inhomogeneities are present.
b) By offsetting the Larmor frequency by -300Hz before the data acquisition, a constant field inhomogeneity is simulated. This results in a VSM of ~ 50 pixels. As shown the scanner reconstruction has SENSE errors and errors due to the shifted coil image. The offline reconstruction does not show these artefacts. The image is successfully reconstructed without Nyquist ghosting.

Following, a linear offset was generated by adding an offset to the gradients. The results for three different cases of linear offset are shown in fig. 5.10. For fig. 5.10a) the applied gradient lead to a buckling of the coil image. The same buckling effect is visible in the scanner reconstruction.

The offline reconstruction in contrast has the correct and shape and no significant artefacts. A slight ringing below the non-linear edges is present for the offline reconstruction. For the reconstructions in fig. 5.10b) and fig. 5.10c) no ringing occurs. This could be due to the fact that for the case where a buckling effect occurs in the coil image, the number of points available for the approximation of the linear interpolation is smaller than in the case when a dilation occurs.

Figure 5.10b) and 5.10c) show the application of a gradient, which leads to a dilation of the data, as seen in the coil image. For 5.10b) the offline reconstruction successfully reconstruct the image without exhibiting any artefacts. The scanner reconstruction has SENSE errors leading to the ripple on the top and bottom of the final reconstruction. Furthermore, a geometric distortion is still present. For an increasing dilation effect as shown in 5.10c) the scanner reconstruction has more severe artefacts. For these strong geometric distortion the offline algorithm still successfully reconstructs an image.
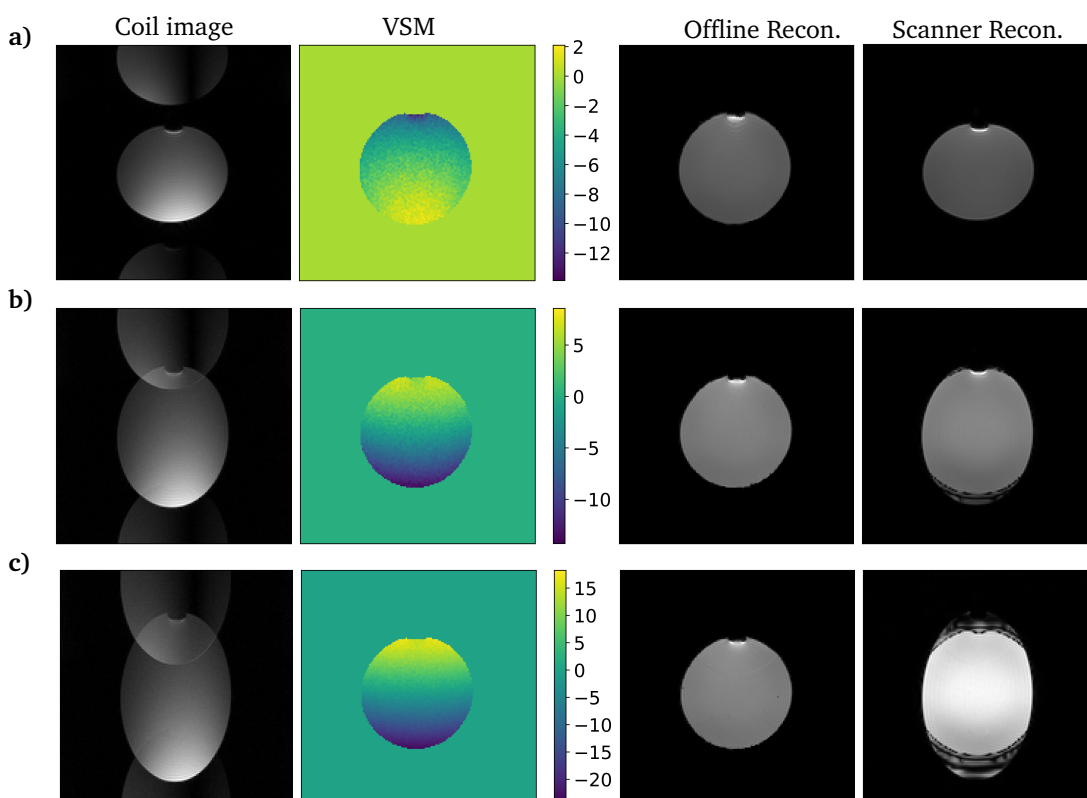
Figure 5.10: Effect of linearly increasing field inhomogeneities on the reconstruction.
a) The applied gradient offset leads to a buckling of the coil image. The scanner reconstruction shows a distorted shape. The distortion is qualitatively similar to the buckling of the coil image. The offline algorithm successfully reconstructs the image without geometric distortions.
b) and **c)** The applied gradient offset leads to a dilation of the coil image. The scanner reconstructions show increasing SENSE errors leading to the ripple on the top and bottom of the final reconstruction. The offline algorithm successfully reconstructs the image without geometric distortions.

Figure 5.11 shows the geometric distortion for an in vivo measurement. The VSM shows that on the top of the image a strong patient susceptibility induced field inhomogeneity is present. This field inhomogeneity leads to a geometric distortion on top of the scanner reconstruction. The offline reconstruction which incorporates the field inhomogeneity information shows no geometric distortion. Therefore, the shape of the reconstructed image is successfully corrected.
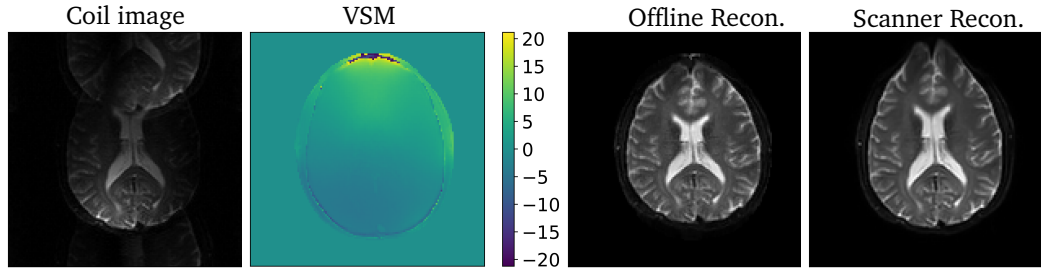
Figure 5.11: Correcting field inhomogeneities in an in vivo measurement.
Equivalently to the images above, the coil image and VSM are shown. The measurement was obtained using a SE sequence. The offline reconstruction is compared to the scanner reconstruction. It is visible, that the shape of the reconstructed image is successfully corrected. The scanner reconstruction does not perform a correction. Thus, the shape of the reconstruction is distorted.

5.5   Multislice Reconstruction and Concomitant Field Modelling

The last sections described the incorporation of a joint estimation of phase maps and image data. The considered slices were collected very close to the MRI scanners *isocenter*, which has the coordinates $(x, y, z) = (0, 0, 0)$. For a usual fMRI study a multislice acquisition is used, which means that multiple slices are acquired sequentially. An intriguing question is if the calculated phase map is also valid for adjacent slices. When only few slices are collected coil heating can be neglected and thus eddy current induced Nyquist ghosts should be equivalent for adjacent slices. Therefore, in principal it can be expected that the phase map does not change.

To asses the reusability of phase maps, 20 slices of 4mm slice thickness were collected. The slices are located between -13.2mm to 62.8mm in relation to the MRI scanners *isocenter*. First, the usual reconstruction procedure was executed using $\Delta\Phi_{FULL}$, yielding $\mathbf{v}_{\Delta\Phi_{FULL}}$. These reconstructions are shown in fig. 5.12a) for different slices. Then the phase map closest to the *isocenter* was stored. The slice for which the phase map was stored is indicated by the green frame in fig. 5.12. This stored phase map is termed $\Delta\Phi_{FULL, ISO}$.

Using $\Delta\Phi_{FULL, ISO}$ instead of the actual phase map, the reconstruction is repeated for all slices. These reconstructions $\mathbf{v}_{\Delta\Phi_{FULL, ISO}}$ are shown in fig. 5.12b). The magnitude difference between the $\mathbf{v}_{\Delta\Phi_{FULL}}$ and $\Delta\Phi_{FULL, ISO}$ are plotted in fig. 5.12c). As expected for the slice with the location -1.2mm, the difference was zero. This is due to the fact that the stored and actual phase map are identical for this slice. Fig. 5.12a) and 5.12b) are visually not distinguishable. Therefore, indeed it can be concluded from this analysis, that reconstruction using stored phase maps is possible and leads to no artefacts.

Still, fig. 5.12c) shows that there is a small difference in the magnitudes. This difference increases for slices further away from the isocenter, hinting at effects stemming from concomitant fields.

To understand concomitant fields it first has to noted that the main magnetic fields introduced in sec. 2.2.2 and in other explanations is often simplified. Often only the main magnetic field $\mathbf{B}_0$ and the gradient vector $\mathbf{G}$ are stated as the magnetic field components in the imaging procedure. Therefore, the total field $\mathbf{B}$ is usually modelled as $B = \mathbf{B}_0 + G_x x + G_y y + G_z z$. However, as the Maxwell equations show, this is a simplification. To asses the total magnetic field, the *Gauss's law for magnetism* and *Ampère's circuital law* have to be taken into consideration. For an infinitesimal current density $\mathbf{J}$ and constant electric field, as can be assumed for the case of voxels sufficiently far away from interface boundaries, *Gauss's law for magnetism* and *Ampère's circuital law* reduce to

$$\nabla \cdot \mathbf{B} = 0$$
$$\nabla \times \mathbf{B} = \mathbf{0} \quad .$$

(5.2)
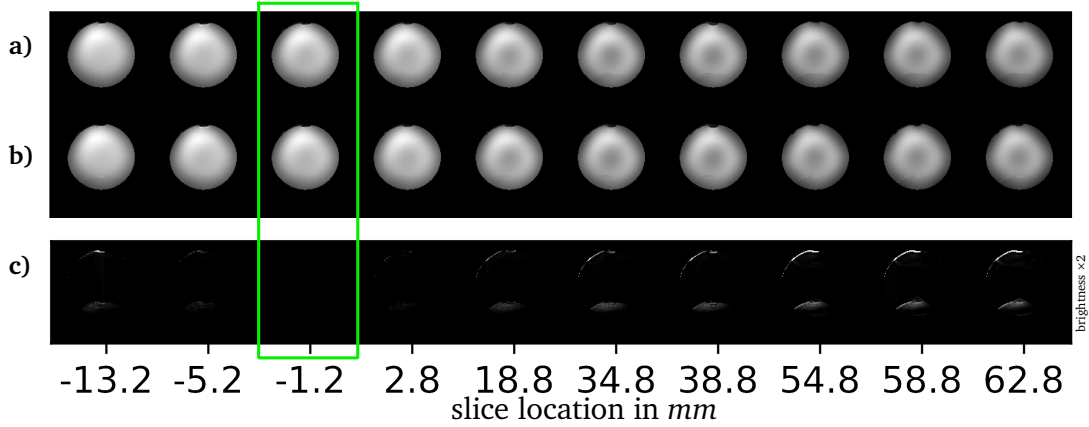
Figure 5.12: Reutilisation of image-based phase maps.
a) shows the reconstruction $\mathbf{v}_{\Delta\Phi_{FULL}}$ for multiple slices. The slice location with respect to the isocenter is given on the x-axis and is identical for all three subgraphs. Therefore, a) represents the usual reconstruction using $\Delta\Phi_{FULL}$. The phase map of the slice framed in green was stored, and is denoted as $\Delta\Phi_{FULL,ISO}$.
b) The procedure was repeated using the stored phase map $\Delta\Phi_{FULL,ISO}$ for the reconstruction of all slices. The reconstructions for different slices are shown in b). A small difference for these reconstruction vs. the reconstruction in a) can be observed.
c) Shows the magnitude difference of a) and b). It is observable that the difference increases with distance from the *isocenter*, hinting on effects stemming from concomitant maxwell fields.

Therefore, the total magnetic field of the lowest order [38] follows

$$B(x,y,z) \quad = \mathbf{B}_0 + G_x x + G_y y + G_z z + \frac{1}{8\mathbf{B}_0} G_z^2 x^2 + \frac{1}{8\mathbf{B}_0} G_z^2 y^2 + \frac{1}{2\mathbf{B}_0}(G_x^2 + G_y^2)z^2$$
$$- \frac{1}{2\mathbf{B}_0} G_y G_z yz - \frac{1}{2\mathbf{B}_0} G_x G_z xz \,. \tag{5.3}$$

For transversal slices several simplifications can be made [39]: Due to the fact that G_y and G_z respectively G_y and G_z are never used at the same time, the last two terms of eq. 5.3 are dropped. Furthermore, the slice selection gradient G_z is applied for a significantly smaller than the readout gradients G_x and G_y. Therefore, for a transversal slice, as used for this work, the field can be approximated following

$$B(x,y,z) = \mathbf{B}_0 + G_x x + G_y y + G_z z + \frac{1}{2\mathbf{B}_0}(G_x^2 + G_y^2)z^2 \,. \tag{5.4}$$

The concomitant field term is then calculated by

$$B_c(x,y,z) = \frac{1}{2\mathbf{B}_0}(G_x^2 + G_y^2)\,z^2 \,. \tag{5.5}$$

Two other simplifications are made. First, a constant readout gradient is assumed and consequently non-uniform ramp sampling neglected. Therefore, Φ_c is linear in time. Also neglecting the *phase-blips* G_y, since they are substantially smaller and activated for a shorter period than the readout gradient G_x, we can calculate the concomitant phase Φ_c following

$$\Phi_c = \gamma \, 2\pi \, \frac{1}{2\mathbf{B}_0} \, G_x^2 \, z^2 \, t \,, \tag{5.6}$$

where t denotes the time between the *odd* and *even* echo peak per slice.

Using this expression the concomitant phase Φ_c was simulated. As mentioned earlier 20 slices were collected , lying between $z = -13.2$mm and $z = 62.8$mm. The measurements were conducted on a $\mathbf{B}_0 = 3$T system using a readout gradient of $G_{RO} = 0.02 \, \frac{\text{T}}{\text{m}}$.
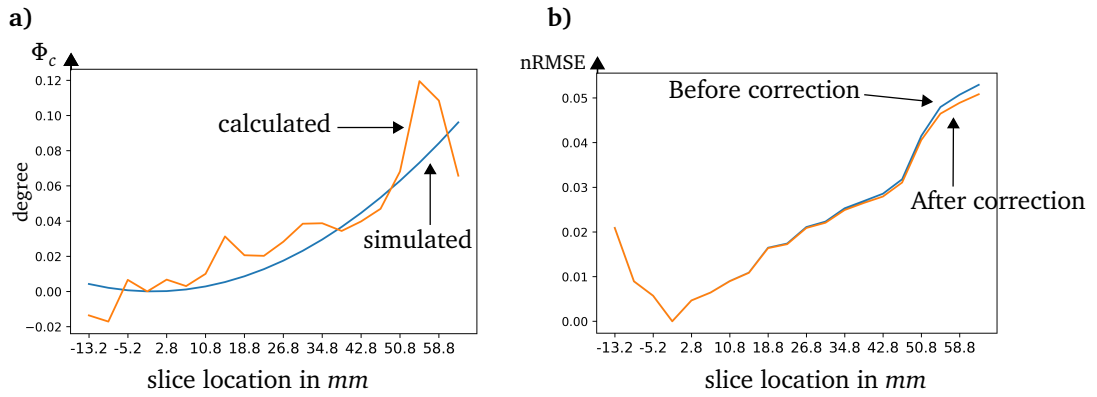
Figure 5.13: Simulation, calculation and correction of concomitant phase term.
a) shows the simulated concomitant phase Φ_c obtained by simulation using eq. 5.6. The actual phase difference between phase maps of slices and the phase map of the isocenter slice was used for the calculation, shown in orange. In general it is visible that the calculation and simulation are in good agreement.
b) shows the nRMSE per slice. It is derived by calculating the error between the reconstruction with the actual phase map and the reconstruction using the stored phase map. Therefore, it is the error between fig. 5.12a) and fig. 5.12b). After applying a correction term derived from a) to the stored phase map, the reconstruction error is slightly reduced.

First the expected concomitant field term was simulated with eq. 5.6. The result is plotted in blue in fig. 5.13a). As expected a quadratic dependance of the error to the slice location results. Second of the phase difference between the actual phase maps $\Delta\Phi_{FULL}$ and the stored phase map $\Delta\Phi_{FULL,ISO}$ was calculated per slice. This result is shown in fig. 5.13b). It is observable that the simulation and calculation are in good agreement. This suggests that the change of the phase map between adjacent slices is indeed contributed to effect of concomitant maxwell fields.

The derived concomitant maxwell phase term Φ_c were used to correct the stored phase map $\Delta\Phi_{FULL,ISO}$. Fig. 5.13b) shows in blue the nRMSE for the usage of $\Delta\Phi_{FULL,ISO}$. Therefore, this is the nRMSE between fig. 5.12a) and fig. 5.12b). The nRMSE is as usual defined by eq. 5.1. To reduce this error, the slices are reconstructed using the stored phase map $\Delta\Phi_{FULL,ISO}$ with an additional slice-dependent correction of concomitant maxwell phase terms Φ_c. This concomitant phase term, obtained from the simulation in fig. 5.13a) respectively eq. 5.6, is subtracted from $\Delta\Phi_{FULL,ISO}$. Consequently, the corrected phase can be directly used in the offline reconstruction. Fig. 5.13b) shows that when using the corrected phase terms, the nRMSE is slightly reduced. The magnitude difference in fig. 5.12 also hints at a small change of object geometry further away from the *isocenter*. A small change in the object diameter for adjacent slices could explain the increasing error visible at the edges.

6 | Discussion

This work aimed to replace the EPI reference scan data with an image-based phase map. Thus, phase errors and image data can both be estimated with the measurement data. This leads to a measurement data driven reconstruction, making the EPI reference scan obsolete.

For non-accelerated measurements collected with SE sequences, the 2D phase maps which were only processed by *wavelet* denoising provided reconstruction results comparable to $\mathbf{v}_{ref}$. Also the introduced 1D phase maps obtained by averaging and masking $\Delta\Phi_{FULL}$ showed reconstruction results without artefacts. Still, the nRMSE was on average slightly higher when using $\Delta\Phi_{FULL}$. In general 2D phase maps can provide better reconstruction when cross-term eddy currents occur or when imaging with oblique scan planes [4] [37] [40]. Figure 5.4a) shows a measurement obtained in a oblique scan plane. As visible all reconstructions are visually equivalent, while the nRMSE of $\mathbf{v}_{\Delta\Phi_{FULL}}$ is slightly higher. This raises the question if $\mathbf{v}_{\Delta\Phi_{FULL}}$ is actually a better reconstruction than $\mathbf{v}_{ref}$. As fig. 5.4a) suggest, the usage of nRMSE for the assessment of the reconstruction can not give a definite answer. SNR maps could be used to further compare $\mathbf{v}_{\Delta\Phi_{FULL}}$ and $\mathbf{v}_{ref}$ [41]. Still, also for R=1 measurements the averaged phase maps $\mathbf{v}_{\Delta\Phi_{AVG}}$ and $\mathbf{v}_{\Delta\Phi_{AVG,M}}$ provided the best nRMSE on average. For measurements obtained with GRE sequences artefacts were already visible for R=1 measurements. Consequently, GRE measurements should always be reconstructed using $\mathbf{v}_{\Delta\Phi_{AVG}}$ or $\mathbf{v}_{\Delta\Phi_{AVG,M}}$.

The image-based phase maps confirmed the assumption of linearly varying phase trend. Therefore, the main effect leading to Nyquist ghost are the introduced eddy currents. Since other effects, like filtering procedures, have the same effect on *odd* and *even* echoes these effects will not appear in image-based phase maps. The results showed that the linear phase trend varies slightly at different locations in PE direction. It was shown that the slope and intercept variation is on average only few percent. This variation was also noted by [4] and [42]. The origin of this small variation remains unclear. On the other hand, the performance of the linear fitting algorithm itself should also be considered. When plotting two linear phase trends which a slope difference only occurring in the third decimal, the difference can not be spotted visualy.

For measurements with twofold acceleration, the usage of $\Delta\Phi_{FULL}$ resulted in serious artefacts in the phase map. These artefacts propagate in the final reconstruction. Therefore, $\Delta\Phi_{AVG}$ was used to obtain valid reconstruction results without artefacts. As mentioned, cross-term eddy currents or measurements obtained under oblique scan planes could induce phase errors which can't be reproduced with a 1D phase map. With the measurements obtained with this work, this situation did not occur. Thus, the nRMSE was always equivalent or lower for $\mathbf{v}_{\Delta\Phi_{AVG}}$ compared to $\mathbf{v}_{\Delta\Phi_{FULL}}$.

As the g-factor increases non-linearly with acceleration, the linear fitting algorithm calculated faulty values for R=3 measurements. Thus, a mask for the g map was derived. This mask excluded values above 20% of the mean g-factor from the averaging procedure. Therefore, this can be seen as an extension to the introduced averaging algorithm. Using the masking and averaging procedure, R=3 accelerated measurements can be reconstructed. For lower acceleration factors the usage of $\Delta\Phi_{AVG}$ yields equivalent results to $\Delta\Phi_{AVG,M}$. Consequently, also for R=1 and R=2 measurements $\Delta\Phi_{AVG,M}$ can be used. For R=3 only $\mathbf{v}_{\Delta\Phi_{AVG,M}}$ yields artefact free reconstructions.

The described averaging and masking procedure are computationally intensive. For the linear fitting procedure a phase unwrapping procedure is necessary. Especially for areas of g-factor induced *noise amplification* this procedure is computationally expensive. The masking procedure requires the calculation of the g-map as an initial step. The g-factor only has to be calculated for superimposed voxels, since the g-factor is equal to one when no aliasing occurs. Still, for all other voxels five matrix multiplication with an order of at least $\mathcal{O}(N^{2.373})$ and a matrix inversion with computational complexity of order $\mathcal{O}(N^3)$ are needed. Therefore, it can be concluded that the proposed averaging

and masking procedures are effective, but significantly increase computational complexity.

For in vivo measurements the proposed algorithm including averaging and masking can successfully reconstruct artefact free images to an acceleration of around R=3.2. For higher acceleration the algorithm leads to residual artefacts, since through the occurring noise amplification leaves few rows in the phase map for the linear fitting algorithm respectively the remaining rows exhibit a lot of fluctuation due to *noise amplification*. Thus, a reconstruction for acceleration factors R>3 does not seem promising. This is due to the fact, that the proposed fitting algorithm is hindered by the strong g-factor induced noise amplification. To reconstruct measurements with threefold and higher acceleration, it should be considered to integrate the phase map into the iterative reconstruction itself, enforcing smoothness of the phase map [43]. This way it could be possible to reconstruct higher accelerated measurements.

All calculation were conducted using a CG gradient without regularisation. As shown, an intrinsic problem of the image-based phase map estimation is the effectively doubled acceleration. Due to the non-linear g-factor increase and consequently occurring noise amplification, the phase map estimation is very sensitive to noise acceleration. These effects could be mitigated by adding appropriate regularisation. In principal the proposed algorithm consists of two steps. In the first step images using only *odd* and *even* echoes are reconstructed to yield the phase map. Therefore, this calculation should be subject to regularisation enforcing smoothness. A smoothness constraint generally comes at the cost of spatial details in the phase map, since a smoothness requirement is a relation of neighbouring pixels. Since the actually reconstructed images of this first step are discarded, a reconstruction enforcing mainly smoothness by appropriate regularisation can be used. For the second step of the algorithm, which includes the calculated phase map into the sensitivity profiles and reconstructs the final image, a different regularisation with a better balance between spatial details and smoothness can be used.

The integration of VSM maps into the iterative reconstruction proved as successful and numerically efficient. As shown in the comparison to the scanner reconstruction, leaving out field inhomogeneity correction can lead to errors stemming from the shifted coil sensitivities as well as SENSE errors in the reconstruction. In contrast to most publications, e.g. [4], the field inhomogeneities were not directly integrated into the forward and reverse model. Such an integration would need non-uniform FFT methods, based on gridding or interpolation [44]. This is necessary to mask the *odd* or *even* echoes correctly. This masking is represented by the pink area in fig. 4.5. Therefore, per iteration the gridding has to be conducted twice, leading to a costly calculation. The proposed method of interpolating the sensitivity maps as an initial step and inversely interpolating the final reconstruction proved to yield good reconstructions. This combines with a reduction of computational complexity by the number of iterations.

Furthermore, the algorithm for the correction of field inhomogeneities was assessed with non-accelerated measurements. In principal the same procedure is used for accelerated measurement. As mentioned to yield artefact free images for higher acceleration, a phase map obtained by masking and averaging the full 2D phase map should be used. Since this masking depends on the g-map, it has to be extended to calculate the g-map of the interpolated sensitivities mimicking the field inhomogeneities. Using this recalculated g-map, the phase map $\Delta\Phi_{AVG,M}$ can also be calculated when incorporating field inhomogeneities. The algorithm can then be used for higher acceleration factors.

Using phantom measurements it was shown that the calculated phase map is also valid for adjacent slices. Two things have to be noted to the practical consideration of this implementation. First, the concomitant phase calculation can easily be added to the calculation of the phase map. Due to the long readout trajectories these have a special importance for single-shot EPI trajectories. Second of all, the calculated effect of the concomitant phase is relatively small. As shown a reconstruction using a saved phase map without concomitant phase correction, the obtained reconstruction still does not show significant artefacts. There is now visible difference in the reconstruction using a saved vs. the actual phase map. Furthermore, for longer fMRI protocols the phase map change is also governed by increasing temperature of the gradient coils and consequently strongly varying eddy currents. Therefore, it is questionable that phase maps could be reused for practical in vivo protocols. It has to be noted that the reutilisation only reduces computational complexity. In principal calculating the full phase map for every slice is the most beneficial options. Nonetheless, using the developed model for the concomitant phase, the phase map of adjacent slices can be seen as sort of a prior knowledge to the calculated phase map.

7 | Conclusion

The goal of this work was to revise the EPI image reconstruction, integrating the most important effects directly into the reconstruction model. Furthermore, the core objective of this work lies in the replacement of the EPI reference scan with an image-based phase map.

For non-accelerated measurements obtained with SE sequences, a 2D phase map provided reconstructions qualitatively equivalent to a reconstruction using EPI reference data. As shown, artefacts induced by higher acceleration or for measurements obtained with GRE sequences can be treated by masking and averaging the 2D phase map. Even for low acceleration such 1D phase maps provided better reconstruction results than the full 2D phase maps. Therefore, further studies should examine the effects lying beneath the phase trend differences in the phase maps.

Other work [4] [5] noted this differences as well. This methods rely either on an analytical solution of the model [5] or employ regularisation methods and a larger number of coils in the head array. Consequently, they did not employ averaging methods and used only denoising. Therefore, these approaches should be tested as well to study if the artefacts in the phase map can be reduced. If the 2D phase map exhibits less artefacts for measurement with acceleration, the proposed averaging and masking method could enable fourfold and higher acceleration.

In total, the core objective, the calculation and integration of image-based phase maps, was achieved. This leads to a measurement data driven, joint reconstruction of phase errors and image data. Therefore, for an acceleration up to R=3 a reconstruction could be obtained without EPI reference scan data.

Furthermore, the integration of VSM into the reconstruction was successful. Only few additional computational complexity was added, obtaining good reconstruction results. Further in vivo measurements should be made testing the limits of this algorithm.

The proposed iterative reconstruction comes at the price of increased computation. Especially due to increasing hardware capabilities, it is predictable that this will play no significant role in the future. Proper regularisation methods should be added to the iterative reconstruction, as these are expected to decrease the noise amplification and will consequently improve the algorithm. One of the significant advantages lies in the fact that for the solution of equation system defined by the model, multiple numerical solution algorithms can be used. Thus, the approach is not dependent on the usage of a CG algorithm.

The proposed model can be seen as a first step. It contains the possibility of including other effects in the model. It was shown how concomitant maxwell fields can be integrated easily into the model-based reconstruction. There are also other effects that can be incorporated into the model and would improve the reconstruction. Examples are signal decay due to T_2^* or motion correction for DWI measurements.

The work shows that an appropriate modelling process of the EPI image acquisition is still an intriguing research question. This leads to the interesting problem of estimating the model parameters either by separate reference scans or jointly with the data. This work contributed to the data-driven joint reconstruction of model parameters and the image itself. Using such data-driven approaches, the scan efficiency can be further improved.

A | Lists of Measurements

The following table summarises the measurement obtained for this work. These measurements were used to calculate all presented results.

Name	Date	$\mathbf{B}_0$	Object	Sequence	R	NUS	Remark
20171201_2	1-12-17	1.5T	Phantom	SE	2	Yes	
20171201_3	1-12-17	1.5T	Phantom	SE	3	Yes	
20171201_4	1-12-17	1.5T	Phantom	GRE	1	Yes	
20171201_5	1-12-17	1.5T	Phantom	GRE	1	Yes	
20171212_1	12-12-17	1.5T	Phantom	SE	1	Yes	
20171212_2	12-12-17	1.5T	Phantom	SE	2	Yes	
20171212_3	12-12-17	1.5T	In vivo	SE	1	Yes	
20171212_4	12-12-17	1.5T	In vivo	SE	2	Yes	
20180124_1	24-1-18	1.5T	Phantom	SE	1	Yes	ω_0 -300Hz
20180124_2	24-1-18	1.5T	Phantom	SE	1	Yes	ω_0 -300Hz
20180124_3	24-1-18	1.5T	Phantom	SE	2	Yes	ω_0 -300Hz
20180124_4	24-1-18	1.5T	Phantom	SE	2	Yes	ω_0 -300Hz
20180124_5	24-1-18	1.5T	Phantom	SE	1	Yes	Linear AP gradient offset
20180124_6	24-1-18	1.5T	Phantom	SE	1	Yes	Linear AP gradient offset
20180124_7	24-1-18	1.5T	Phantom	SE	1	Yes	Linear AP gradient offset
20180124_8	24-1-18	1.5T	Phantom	SE	1	Yes	Linear AP gradient offset
20180124_9	24-1-18	1.5T	Phantom	SE	1	Yes	Linear AP gradient offset
20180124_10	24-1-18	1.5T	Phantom	SE	2	Yes	Linear AP gradient offset
20180124_11	24-1-18	1.5T	Phantom	SE	1	Yes	Linear AP gradient offset
20180309_1	9-3-18	1.5T	In Vivo	SE	1	Yes	PE Direction Changed
20180309_2	9-3-18	1.5T	In Vivo	SE	2	Yes	PE Direction Changed
20180309_3	9-3-18	1.5T	In Vivo	SE	3	Yes	PE Direction Changed
20180309_4	9-3-18	1.5T	In Vivo	GRE	1	Yes	PE Direction Changed
20180309_5	9-3-18	1.5T	In Vivo	GRE	2	Yes	PE Direction Changed
20180309_6	9-3-18	1.5T	In Vivo	GRE	3	Yes	PE Direction Changed
20180419_1	19-4-18	3.0T	Phantom	GRE	1	Yes	
20180419_2	19-4-18	3.0T	Phantom	GRE	2	Yes	
20180419_3	19-4-18	3.0T	Phantom	GRE	3	Yes	
20180419_4	19-4-18	3.0T	Phantom	GRE	4	Yes	
20180419_5	19-4-18	3.0T	Phantom	GRE	1	Yes	Linear AP gradient offset
20180419_6	19-4-18	3.0T	Phantom	GRE	2	Yes	Linear AP gradient offset
20180419_7	19-4-18	3.0T	Phantom	GRE	3	Yes	Linear AP gradient offset
20180419_8	19-4-18	3.0T	Phantom	GRE	4	Yes	Linear AP gradient offset
20180419_9	19-4-18	3.0T	Phantom	GRE	1	Yes	Different Phantom
20180419_10	19-4-18	3.0T	Phantom	GRE	2	Yes	Different Phantom
20180419_11	19-4-18	3.0T	Phantom	GRE	3	Yes	Different Phantom
20180419_12	19-4-18	3.0T	Phantom	GRE	4	Yes	Different Phantom
20180419_13	19-4-18	3.0T	Phantom	GRE	1	Yes	Different Phantom
20180423_1	23-4-18	3.0T	Phantom	GRE	1	Yes	
20180423_2	23-4-18	3.0T	Phantom	GRE	2	Yes	
20180423_3	23-4-18	3.0T	Phantom	GRE	3	Yes	
20180423_4	23-4-18	3.0T	Phantom	GRE	4	Yes	

20180423_5	23-4-18	3.0T	Phantom	GRE	1	Yes	
20180423_6	23-4-18	3.0T	Phantom	GRE	2	Yes	
20180423_7	23-4-18	3.0T	Phantom	GRE	3	Yes	
20180423_8	23-4-18	3.0T	Phantom	GRE	4	Yes	
20180507_1	7-5-18	1.5T	Phantom	SE	1	Yes	
20180507_2	7-5-18	1.5T	Phantom	SE	1	Yes	Phase Blips off
20180507_3	7-5-18	1.5T	Phantom	SE	1	Yes	1D test mode
20180507_4	7-5-18	1.5T	Phantom	SE	2	Yes	
20180507_5	7-5-18	1.5T	Phantom	SE	3	Yes	
20180613_1	13-6-18	3.0T	Phantom	GRE	1	Yes	
20180613_2	13-6-18	3.0T	Phantom	GRE	2	Yes	
20180613_3	13-6-18	3.0T	Phantom	GRE	3	Yes	
20180613_4	13-6-18	3.0T	Phantom	SE	1	Yes	
20180613_5	13-6-18	3.0T	Phantom	SE	2	Yes	
20180613_6	13-6-18	3.0T	Phantom	SE	3	Yes	
20180613_7	13-6-18	3.0T	Phantom	SE	1	Yes	Multislice: 20 Slices
20180613_8	13-6-18	3.0T	Phantom	SE	2	Yes	Multislice: 20 Slices
20180613_9	13-6-18	3.0T	Phantom	SE	1	Yes	Oblique Plane
20180613_10	13-6-18	3.0T	Phantom	SE	1	Yes	Double Oblique Plane
20180613_11	13-6-18	3.0T	Phantom	SE	1	Yes	Channel Delay Offset
20180613_12	13-6-18	3.0T	In vivo	GRE	1	Yes	
20180613_13	13-6-18	3.0T	In vivo	GRE	2	Yes	
20180613_14	13-6-18	3.0T	In vivo	GRE	3	Yes	
20180613_15	13-6-18	3.0T	In vivo	SE	1	Yes	
20180613_16	13-6-18	3.0T	In vivo	SE	2	Yes	
20180613_17	13-6-18	3.0T	In vivo	SE	3	Yes	
20180613_18	13-6-18	3.0T	In vivo	GRE	1	Yes	
20180615_1	15-6-18	3.0T	In vivo	GRE	1	Yes	
20180615_2	15-6-18	3.0T	In vivo	GRE	2	Yes	
20180615_3	15-6-18	3.0T	In vivo	GRE	3	Yes	
20180615_4	15-6-18	3.0T	In vivo	SE	1	Yes	
20180615_5	15-6-18	3.0T	In vivo	SE	2	Yes	
20180615_6	15-6-18	3.0T	In vivo	SE	3	Yes	
20180615_7	15-6-18	3.0T	In vivo	GRE	1	Yes	
20180615_8	15-6-18	3.0T	In vivo	GRE	2	Yes	
20180615_9	15-6-18	3.0T	In vivo	GRE	3	Yes	
20180615_10	15-6-18	3.0T	In vivo	SE	1	Yes	
20180615_11	15-6-18	3.0T	In vivo	SE	2	Yes	
20180615_10	15-6-18	3.0T	In vivo	SE	3	Yes	

Table A.1: Obtained measurements

B | Program Structure

The following table B.1 summarises the loaded data and the loaded parameters from the *.hdf5* file. The data and parameters were used to calculate the results of this work. For the calculation of the results multiple scripts and functions were implemented. An overview of the implemented functions is given in table B.2.

Name	Type	Size	Description
Body coil sensitivity	Data	$N_y \times N_x$	Sensitivity matrix for RF body coil
Coil array sensitivities	Data	$n_c \times N_y \times N_x$	Sensitivity matrices for surface coil array
Raw data	Data	EPI factor $\times N_x$ *factor*	Measured data in *k*-domain, *factor* is dependent on slope fraction used for sampling and oversampling factors
Sense data	Data	$N_y \times N_x$	Coil images before SENSE unfolding
Phase data	Data	EPI factor $\times N_x$	EPI reference scan
Field map	Data	$N_y \times N_x$	Field map in Hz
BW in PE direction	Parameter	1	Bandwidth in PE direction, calculated with echo times
Oversampling factors	Parameter	1×1	Oversampling factors in PE and RO direction
Scan resolution	Parameter	1×1	Number of collected echoes $\times$ sampling points in readout direction
Reconstruction resolution	Parameter	1×1	Size of matrices used for reconstruction in the scanner
R	Parameter	1	Reduction Factor in PE direction
PE direction	Parameter	1	PE direction in *x* or *y* direction
Odd echo direction	Parameter	1	*Odd* echo in $-x$ or *x* direction
Sampling points	Parameter	1	Sampling points in RO direction

Table B.1: Loaded data and parameters

Function	Description
b0interpolation.py	Function to interpolate and inversely interpolate sensitivity maps
conjugategradient.py	Multiple functions of calculating conjugate gradient with integration of image-based phase maps
deadface_io_python3.py	Read and write files from scanner recon unit
filtering.py	Wavelet and median filters
gridding.py	Readout gridding, data padding
hdf5.py	Load Data from hdf5 file, see table B.1 for table of loaded data
measurements.py	Dictionary with all obtained measurements, see table A.1 for measurement list
phasemap.py	Calculation of phase map and different processing algorithms
readout.py	Load parameters from sin file, needed if hdf5 import fails
window_functions.py	Kaiser-Bessel window functions

Table B.2: Implemented functions

Bibliography

[1] P. Mansfield, "Multi-planar image formation using nmr spin echoes," *Journal of Physics C: Solid State Physics*, vol. 10, no. 3, p. L55, 1977.

[2] H. Bruder *et al.*, "Image reconstruction for echo planar imaging with nonequidistant k-space sampling," *Magnetic Resonance in Medicine*, vol. 23, no. 2, pp. 311–323, 1992.

[3] F. Schmitt, M. K. Stehling, and R. Turner, *Echo-Planar Imaging: Theory, Technique and Application*. Springer, 1998.

[4] U. Yarach *et al.*, "Model-based iterative reconstruction for single-shot epi at 7 t," *Magnetic resonance in medicine*, vol. 78, no. 6, pp. 2250–2264, 2017.

[5] V. B. Xie *et al.*, "Robust epi nyquist ghost removal by incorporating phase error correction with sensitivity encoding (pec-sense)," *Magnetic resonance in medicine*, vol. 79, no. 2, pp. 943–951, 2018.

[6] S. Ljunggren, "Imaging methods," *Journal of Magnetic Resonance*, vol. 54, pp. 338–343, 1983.

[7] P. Roemer *et al.*, "The nmr phased array," *Magnetic resonance in medicine*, vol. 16, no. 2, pp. 192–225, 1990.

[8] K. P. Pruessmann *et al.*, "Sense: sensitivity encoding for fast mri," *Magnetic resonance in medicine*, vol. 42, no. 5, pp. 952–962, 1999.

[9] K. P. Pruessmann *et al.*, "Advances in sensitivity encoding with arbitrary k-space trajectories," *Magnetic resonance in medicine*, vol. 46, no. 4, pp. 638–651, 2001.

[10] D. G. Nishimura, *Principles of magnetic resonance imaging*. Stanford University, 1996.

[11] E. M. Haacke *et al.*, *Magnetic resonance imaging: physical principles and sequence design*. John Wiley & Sons, 1999.

[12] M. A. Bernstein, K. F. King, and X. J. Zhou, *Handbook of MRI pulse sequences*. Elsevier, 2004.

[13] D. J. Larkman and R. G. Nunes, "Parallel magnetic resonance imaging," *Physics in medicine and biology*, vol. 52, no. 7, pp. 15–55, 2007.

[14] M. H. Hayes, *Statistical digital signal processing and modeling*. John Wiley & Sons, 2009.

[15] S. Aja-Fernández, G. Vegas-Sánchez-Ferrero, and A. Tristán-Vega, "Noise estimation in parallel mri: Grappa and sense," *Magnetic resonance imaging*, vol. 32, no. 3, pp. 281–290, 2014.

[16] J. Pauly, "Chapter 2: Partial k-space reconstruction," 04 2018. `https://users.fmrib.ox.ac.uk/~karla/reading_group/lecture_notes/Recon_Pauly_read.pdf`.

[17] Q. X. Yang *et al.*, "Double-sampled echo-planar imaging at 3 tesla," *Journal of Magnetic Resonance, Series B*, vol. 113, no. 2, pp. 145–150, 1996.

[18] S. B. Reeder *et al.*, "A novel object-independent "balanced" reference scan for echo-planar imaging," *Journal of magnetic resonance imaging: JMRI*, vol. 9, no. 6, p. 847, 1999.

[19] J. A. Fessler, "Model-based image reconstruction in mri," Huangguoshu International Interdisciplinary Conferenceon Biomedical Mathematics, 2010.

[20] R. Remis, *EE4595 Wavefield Imaging - Lecture Notes*. TU Delft, 2017.

[21] C. R. Vogel, *Computational methods for inverse problems*. SIAM, 2002.

[22] J. A. Fessler, "Model-based image reconstruction for mri," *IEEE Signal Processing Magazine*, vol. 27, no. 4, pp. 81–89, 2010.

[23] Philips, "Ingenia 1.5t mr-system," June 2018. `https://www.philips.de/healthcare/product/HC781341/ingenia-15t-mrsystem`.

[24] Philips, "dstream headspine coil," June 2018. `https://www.philips.de/healthcare/product/HC781342/ingenia-30t-mrsystem`.

[25] M. A. Bernstein, "Field strength dependence in mri: Advantages and artifacts at 3t," in *Proceedings of the ISMRM*, 2006.

[26] J. Allison and N. Yanasak, "What mri sequences produce the highest specific absorption rate (sar), and is there something we should be doing to reduce the sar during standard examinations?," *American Journal of Roentgenology*, vol. 205, no. 2, pp. W140–W140, 2015.

[27] NumPyDevelopers, "Numpy," June 2018. `https://www.numpy.org/`.

[28] J. I. Jackson *et al.*, "Selection of a convolution function for fourier inversion using gridding (computerised tomography application)," *IEEE transactions on medical imaging*, vol. 10, no. 3, pp. 473–478, 1991.

[29] J. Pauly, "Chapter 5: Reconstruction of non-cartesian data," 07 2014. `https://users.fmrib.ox.ac.uk/~karla/reading_group/lecture_notes/AdvRecon_Pauly_read.pdf`.

[30] J. O'sullivan, "A fast sinc function gridding algorithm for fourier inversion in computer tomography," *IEEE transactions on Medical Imaging*, vol. 4, no. 4, pp. 200–207, 1985.

[31] D. Holland, J. M. Kuperman, and A. M. Dale, "Efficient correction of inhomogeneous static magnetic field-induced distortion in echo planar imaging," *Neuroimage*, vol. 50, no. 1, pp. 175–183, 2010.

[32] P. Jezzard and R. S. Balaban, "Correction for geometric distortion in echo planar images from b0 field variations," *Magnetic resonance in medicine*, vol. 34, no. 1, pp. 65–73, 1995.

[33] A. Haase *et al.*, "Flash imaging. rapid nmr imaging using low flip-angle pulses," *Journal of Magnetic Resonance*, vol. 67, no. 2, pp. 258–266, 1986.

[34] T.-K. Truong and A. Guidon, "High-resolution multishot spiral diffusion tensor imaging with inherent correction of motion-induced phase errors," *Magnetic resonance in medicine*, vol. 71, no. 2, pp. 790–796, 2014.

[35] N. Kingsbury, "Complex wavelets for shift invariant analysis and filtering of signals," *Applied and computational harmonic analysis*, vol. 10, no. 3, pp. 234–253, 2001.

[36] H. Gudbjartsson and S. Patz, "The rician distribution of noisy mri data," *Magnetic resonance in medicine*, vol. 34, no. 6, pp. 910–914, 1995.

[37] D. Xu *et al.*, "Robust 2d phase correction for echo planar imaging under a tight field-of-view," *Magnetic resonance in medicine*, vol. 64, no. 6, pp. 1800–1813, 2010.

[38] M. A. Bernstein *et al.*, "Concomitant gradient terms in phase contrast mr: analysis and correction," *Magnetic resonance in medicine*, vol. 39, no. 2, pp. 300–308, 1998.

[39] X. J. Zhou *et al.*, "Concomitant magnetic-field-induced artifacts in axial echo planar imaging," *Magnetic resonance in medicine*, vol. 39, no. 4, pp. 596–605, 1998.

[40] P. Jezzard, A. S. Barnett, and C. Pierpaoli, "Characterization of and correction for eddy current artifacts in echo planar diffusion imaging," *Magnetic resonance in medicine*, vol. 39, no. 5, pp. 801–812, 1998.

[41] P. M. Robson *et al.*, "Comprehensive quantification of signal-to-noise ratio and g-factor for image-based and k-space-based parallel imaging reconstructions," *Magnetic Resonance in Medicine*, vol. 60, no. 4, pp. 895–907, 2008.

[42] U. Yarach *et al.*, "Dynamic 2d self-phase-map nyquist ghost correction for simultaneous multi-slice echo planar imaging," *Magnetic resonance in medicine*, 2018.

[43] Z. Hu *et al.*, "Phase-updated regularized sense for navigator-free multishot diffusion imaging," *Magnetic resonance in medicine*, vol. 78, no. 1, pp. 172–181, 2017.

[44] L. Greengard and J.-Y. Lee, "Accelerating the nonuniform fast fourier transform," *SIAM review*, vol. 46, no. 3, pp. 443–454, 2004.